THESIS ON MECHANICAL ENGINEERING E104

ZrC-based and ZrC-doped Composites for High-Temperature and Wear Applications

DER-LIANG YUNG

TUT PRESS

TALLINN UNIVERSITY OF TECHNOLOGY
Faculty of Mechanical Engineering
Department of Materials Engineering

Dissertation was accepted for the purpose of a Degree of Doctor of Philosophy in Engineering on October 14, 2016.

Supervisor: Professor, Dr. Irina Hussainova, Department of Materials Engineering, Tallinn University of Technology, Estonia

Co-supervisor: Maksim Antonov (PhD). Department of Materials Engineering, Tallinn University of Technology, Estonia

Opponents:

1. Michael Gasik, professor, Dr., Dr.Sci. Aalto University Foundation,
   School of Chemical Technology
   Finland

2. Alexander Vanetsev, PhD. Institute of Physics, University of Tartu,
   Laboratory of Laser Spectroscopy
   Estonia

Defence of the thesis: November 14, 2016 @ 12:00, room U05-216

Tallinn University of Technology

Ehitajate tee 5, Tallinn, Estonia

Declaration:

Hereby I declare that this doctoral thesis, my original investigations and achievements, submitted for the doctoral degree at Tallinn University of Technology, has not been submitted for any academic degree elsewhere.

ISSN 1406-4758
ISBN 978-9949-83-029-9 (Publication)
ISBN 978-9949-83-030-5 (PDF)

MEHHANOTEHNIKA E104

ZrC baasil ja ZrC-ga legeeritud komposiitmaterjalid rakendusteks kõrgtemperatuursetes ja kulumistingimustes

DER-LIANG YUNG

TTÜ
KIRJASTUS

CONTENTS

LIST OF PUBLICATIONS

The present doctoral dissertation is based on the following peer reviewed publications, referred to in the text as **Papers I-IV**:

Paper I **Yung DL**, Hussainova I, Rodriguez MA, Traksmaa R. Processing of ZrC-TiC Composites by SPS. *Key Engineering Materials*. (2016) 674, 94−99, DOI: 10.4028/www.scientific.net/KEM.674.94

Paper II **Yung DL**, Antonov M, Hussainova I. Spark plasma sintered ZrC-Mo cermets: Influence of temperature and compaction pressure. *Ceramics International*. (2016) 42 (11), 12907−12913, DOI: dx.doi.org/10.1016/j.ceramint.2016.05.059

Paper III **Yung DL**, Antonov M, Veinthal R, Hussainova I. Wear behaviour of doped WC-Ni based hardmetals tested by four methods. *Wear*. (2016) 352-353, 171−179, DOI: dx.doi.org/10.1016/j.wear.2016.02.015

Paper IV **Yung DL**, Cygan S, Antonov M, Jaworska L, Hussainova I. Ultra high-pressure spark plasma sintered ZrC-Mo and ZrC-TiC composites. *International Journal of Refractory Metals and Hard Materials.* (2016) 61, 201-206, DOI: http://dx.doi.org/10.1016/j.ijrmhm.2016.09.014

ABBREVIATIONS

AC2T – Austrian Centre of Tribology

CMC – Ceramic Matrix Composite

CTE – Coefficient of Thermal Expansion

DC – Direct Current

EDS – Energy Dispersive Spectrometer

HIP – Hot Isostatic Pressing

HPHT – Ultra-High-Pressure, High-Temperature

HT-XRD – High-Temperature X – ray diffraction

IFT – Indentation Fracture Toughness

IOSP – Institute of Advanced Manufacturing Technology

ICV – Institution of Ceramics and Glass

MFP – Mean free path

MMC – Metal Matrix Composites

OECD – Organisation of Economic Cooperation and Development

PTA – Plasma Transferred Arc

RT – Room temperature

SEM – Scanning Electron Microscope

SPS – Spark Plasma Sintering

TBM – Tunnel Boring Machine

TGA – Thermogravimetric Analysis

TUT – Tallinn University of Technology

UHTC – Ultra-High-Temperature Ceramics

VHTR – Very High-Temperature Reactor

vol.% - volume percentage

wt.% - weight percentage

XRD – X – ray diffraction

PREFACE

The area of complex and heavy industries spurs the global demand for novel materials with multiple desirable properties from advanced production technologies. These materials are classified as ultra-high-temperature ceramics (UHTCs), typically carbides, nitrides, and borides [1]. They are usually handled using powder metallurgical methods, where monolithic ceramics or composite materials can be produced. The benefits of composite materials are the ability to combine advanced properties from two or more compounds with preferable characteristics into a single material.

Composite materials possess a set of unique properties not achievable with a single monolithic material. One such class of composites is called ceramic matrix composites (CMCs) [2]. The development of CMC was driven by the fact that monolithic ceramics are intrinsically brittle in nature and mechanically unreliable for applications involving rigorous stress loads. For example, the base carbide could have very low thermal conductivity and ion radiation absorbance, yet fracture toughness is also intrinsically low. However, when combined with a reinforcing carbide with similar hardness and better strength, the new composite material becomes imbued with characteristics of each monolithic compound.

Similarly, another class of composite materials is called cemented carbides, or cermets, whose classic example is tungsten carbide with either nickel or cobalt binder. WC-Co has been thoroughly studied for use in drilling and cutting tools [3, 4]. What distinguishes the cemented carbide structures from the CMC is the use of a metal binder to hold the harder carbide particles together. In the example of WC-Co, the metal binder offers enhanced toughness and ductility to the overall composite, while the harder carbide offers incredible wear resistance against abrasion [5].

Whether using CMCs or cemented carbide composites, the goal is to improve the weaknesses of the base material. Another possibility involves using carbides as a reinforcement hardfaced particulate in alloy coatings [6]. The reinforced coating could reduce the wear rate and handle high-temperature abrasion wear under oxidative conditions.

The focus of this thesis centres on zirconium carbide (ZrC) and can be viewed as the carbide's application into three distinct streams: 1) ZrC-based composites; 2) ZrC-doped hardmetals; 3) ZrC reinforcement particulate into a base alloy.

The properties of ZrC make it an ideal base material for applications in the nuclear industry and space vehicles. ZrC already possesses innate resistance to irradiation damage [7] and suitably low thermal conductivity [8, 9]. The space shuttle's underbelly is equipped with thermal plating. It is a critical component during vehicle re-entry through Earth's atmosphere when the silica base compound must withstand up to 1200 °C [10]. Similarly, research into the new generation of nuclear reactors, dubbed the generation IV series of reactors including Very High-Temperature Reactors (VHTRs) that could have operating temperatures up to 1000 °C [11]. Pure ZrC can be oxidised at around 600 °C [12]; therefore, another goal is to increase ZrC composite's resistance to oxidation.

1. REVIEW OF THE LITERATURE

1.1 Introduction

Climate change risks and catastrophes have taken front page news in the 21st century because no other time in history has humanity had so much impact on the Earth. In the developing and developed nations, there is an ever-growing need for energy resources. There are many remedies to satisfy this demand; one such solution is nuclear energy. The world will demand new energy sources, especially zero emission sources. Electricity demand will rise two fold from 2011 to 2035 [13]. However, to continue development and advancement of such technology, new composite materials must be created. By 2020-2040, the fourth generation nuclear power plant is expected to be within technological capability [14]. Zirconium based alloys have been used as fuel rod sheaths in Candu reactors [15] for the last 40 years with an operating temperature of 300 °C [16]. New VHTR would have an operating temperature of up to 1000 °C for optimal operating efficiency and would also require new composite materials that can survive those environments [14]. High-temperature reactors can drive efficient processes to generate energy products other than electricity: hydrogen, synthetic hydrocarbon fuels from coal or biomass, or process heat for the industry [17]. ZrC could be an ideal candidate given its high-temperature properties and resistance to radiation damage on its microstructure. ZrC has potential use in the nuclear industry where operating temperatures approach ~1000 °C [11].

ZrC is also considered a potential material in aerospace applications [17]. Space vehicles are typically categorised as either one-time or fully reusable space transport systems. When a space vehicle re-enters earth's atmosphere, it is exposed to incredible pressures and heat stresses. In order to be commercially viable, a reusable space vehicle may have to perform multiple launches and re-entries per month in a safe, cost-effective manner. The design aspects of re-entry vehicles focus on the winged craft characterised by sharp configurations, aviation-like, able to fly at high altitudes [18]. Heat transfer during re-entry is characterised as either conductive heat from friction in the solid material or convective heat, but in both cases is attributed as "radiative equilibrium temperature" [19]. At the forefront, these re-rentry vehicles are composed of UHTC materials due to their tensile strength at high-temperature and oxidation resistance. The classic example of the American space shuttle from the National Aeronautics and Space Administration employs a silica material to deflect and dissipate heating during vehicle atmospheric re-entry. The material should withstand temperatures up to 1200 °C under atmospheric conditions [10].

Apart from using ZrC as a base material for new composites, ZrC is also employed as an additive to composites or reinforcement hardfacing to coatings. In the field of large-scale industrial tools for underground tunneling, the vehicles dubbed, Tunnel Boring Machines (TBMs), employ WC hardmetal inserts on to frontal drag bits to excavate the earth [20]. Cemented carbide tools possess a finite lifespan depending on the excavation's ground abrasivity and subsequent wear on the tool [21]. The goal is to increase tool lifespan, achieving predictable wear. For industry, the effort to reduce the TBM downtime, above all, is financially beneficial for extensive projects. Underground, the front end of the soft ground TBM is subjected to a hyperbaric environment, and as such, any human intervention work becomes a diver operation [22]. Tools with enhanced lifespan mitigate worker risk as the number of instances for tool replacement is reduced.

Another area where refractory carbides play a pivotal role is reinforcements for softer binder materials. Similar to cemented hardmetals, metal matrix composites (MMCs) are a mixture of metals that possess ductility and versatility, but have reduced tensile strength (if compared to metals) and hardness (if compared to ceramics). Heavy industries, such as the oil and gas, use drilling tools and pipes that feature metal materials as the basis of their equipment. These materials are more prone to wear and corrosion especially under high-temperature conditions up to 500 °C. Plasma transferred arc-welding (PTA) technology is able to provide a coating of a wearable composite material, deposited onto the wear-prone parts, increasing its life span. Wear resistant MMCs produced by hardfacing techniques are meant to protect a component or substrate against abrasion, impact, and/or erosion [23-27]. A common MMC reinforced with refractory carbide is a Ni-based matrix reinforced with fused (WC/W_2C) particles. However, this material is only viable at temperatures below 600 °C due to its limited oxidation resistance [28]. Compared with WC, ZrC [29] and TiC are viable alternatives, providing improved oxidation resistance at 800 °C, and abrasive wear resistance up to 900 °C [30]. This improvement is made possible due to the abrasive action, limiting the growth of oxide below critical thickness for exfoliation.

1.2 Properties of ZrC

ZrC is an UHTC with a crystalline compound featuring a host metal and carbon. This is structured in a close-packed arrangement where carbon occupies an interstitial space within the structure. ZrC's unique properties include its melting point (~3420 °C), high hardness (~25.5 GPa), low electrical resistivity (4.3×10^{-7} Ω•m), and Young's modulus of elasticity (~400 GPa) [1]. ZrC has better amorphisation than silicon carbide (SiC) during irradiation exposure since it possesses covalent, metallic and ionic bonds [31], hence making it an ideal material for nuclear applications. As an additive to composites, ZrC decreases the thermal conductivity and thermal diffusivity of the composite; as a result, even at ultra-high-temperatures, the composite remains resistant to ablation effects due to oxidation [32]. ZrC activation energy was calculated from Murray's formula as 41 kcal•mol^{-1} (171.7 kJ•mo1^{-1}), suggesting that ZrC sintering requires temperatures of at least 2400 °C [33].

ZrC starts to oxidise from as low as 600 °C, depending on the partial pressure of oxygen [12]. ZrO_2 oxidation produces species of the tetragonal or monoclinic shapes, which are the usual products. At temperatures between 600 and 700 °C, c-ZrO_2 phase forms a compact, pore-free microstructure, thus slowing further oxidation of the matrix. Pure ZrC can produce a protective oxide layer between 600 – 700 °C, depending on partial pressure. Further agitation easily disrupts the protective layer and causes further oxide penetration into the substrate. It is assumed that the c-ZrO_2 phase acts as a diffusion barrier for transport of oxygen so that the local oxygen potential at the ZrC/ZrO_2 interface becomes too low to oxidise the carbon component in ZrC [34].

1.3 Synthesis of pure ZrC

1.3.1 Reactive Sintering

There are various routes to synthesise ZrC. Typically, the easiest route is using ZrO_2 powder with excess graphite at temperatures up to 1500 °C to achieve reactive sintering [35]. Similarly, ZrC powders can be synthesised by combustion or carbothermal reduction of a precursor derived from zirconium nitrate, urea, and glucose mixed solution. This is performed under argon at 1200–1600 °C for 3 h, where the powders are spherically shaped, (120–180 nm in diameter) and oxygen content (1.4 wt.%) [36].

1.3.2 Laser pyrolysis

Laser pyrolysis technique is based on interaction between a laser beam and a gaseous or liquid precursor. It is an energy intensive process, similar to carbothermal reduction. ZrC nanopowders can be produced from an intimate mixture of zirconium butoxide composed of ZrO_2 crystalline nanograins and free C undergoing laser pyrolysis. The annealing temperature needed is up to 1600 °C under argon atmosphere to achieve a grain size of 100 nm respectively [37]. Combemalea et al. [38] managed to reduce the yielded ZrC grain size to 35 nm using $ZrCl_4$ as a precursor substrate. However, HCl emission and Cl pollution in the final powders appeared as main drawbacks.

1.3.3 Sol-gel route

Nanosized ZrC can be synthesised from a sol-gel route using zirconium n-proproxide, acetic acid and saccharose as a carbon source [39]. The heat treatment can be done at 1200 °C, but would produce a ZrC containing excessive oxygen. Increasing the heat treatment temperature to 1600 °C would decrease the oxygen levels but also increase the size of the ZrC grains from 90 to 150 nm.

1.3.4 Mechanical alloying

Nanocrystalline ZrC of composition $Zr_{56}C_{44}$ was synthesised at room temperature by attrition milling elemental Zr and C powders [40]. The ZrC powders had homogeneous shape with smooth surface and uniform size (~0.5 mm diameter). The ZrC grain size was 0.47 nm. The experiment was done in a stainless steel milling container with steel balls and since the milling was done at room temperature, the necessary energy was obtained from friction alone. Other instances include milling a powder mixture of Zr/C=1/1 molar ratio in a planetary ball mill and then exposing the content to air [41]. The substance self-ignited spontaneously and the self-propagating high-temperature synthesis of ZrC simultaneously occurred.

1.4 Sintering ZrC Composites

Various routes exist for sintering ZrC composites, including hot isostatic pressing (HIP) [42], hot pressing [33], pressureless sintering [43], and spark plasma sintering [44]. For CMC, the two materials ZrC-20Mo and ZrC-20TiC will employ spark plasma sintering (SPS) technology. However, the SPS technology comes in two forms, at least in this case dealing with compaction pressure. Hence, we divide the discussion into conventional SPS and ultra-high-pressure, high-temperature (HPHT) SPS. For the section on ZrC and TiC additive to cemented carbide, sinterHIP will be used. Finally, for the portion of ZrC and TiC hardfaced reinforcement, plasma transferred arc welding (PTA) will be used.

1.4.1 Spark Plasma Sintering

UHTC materials are borides, carbides, and nitrides of the Group IV–V elements of the periodic table. They all have very low sinterability due to their covalent atomic bonding and low self-diffusion coefficients [45]. Spark plasma sintering (SPS), also known as field-assisted sintering technique (FAST), is a fast, clean, but energy intensive technique for improving sintering kinetics [46]. Because of its rapid heating rate, the process eliminates the surface impurities and defects that would occur during vacuum or gas furnace heating. Typical pulse duration is in the order of a few milliseconds. Owing to the compact geometry of the die and punches, sintering cycles with heating rates as high as 1000 $°C \cdot min^{-1}$ are possible and enable significant reduction in the total duration of the process and energy costs.

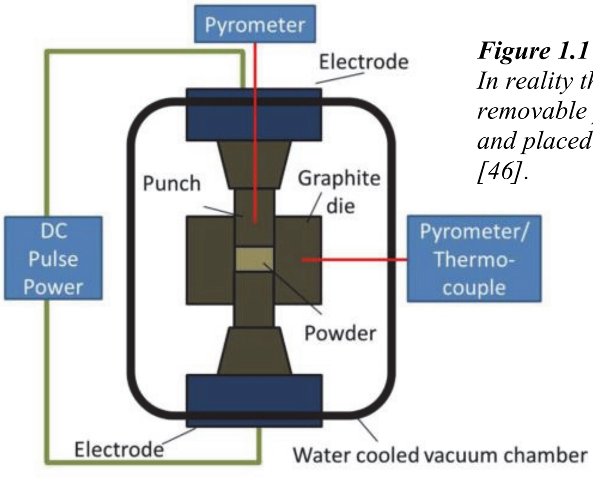

Figure 1.1 *Schematic of the SPS machine. In reality the die and punch dies are removable pieces assembled with powder and placed at the centre of the machine [46].*

Schematic of Figure 1.1 shows the SPS technology, which combines compaction and pulsed current heating conducted through the graphite punches [46]. Graphite is a typical element in the composition of dies and moulds, as well as in the individual sheets used to insulate the powders from the punch walls. Notice also the cylindrical shape of the produced specimens, which is the standard for the technology. This ensures evenly distributed pressures when pressing in a uni-axial fashion. Large specimen dimensions and improved flexibility in terms of possible product geometries are still needed and further development of this technology is required [47].

The typical parameters of the SPS technology usually revolve around setting pressure and temperature. The maximal temperature achieved by using standard graphite tools ranges up to 2000 °C. The pressure depends on the diameter of the punch and sample. Typical pressures considering maximum threshold are up to 50 MPa, but depending on the grade of graphite used, pressures up to 100 MPa on a 20 mm diameter punch (32 kN) are possible [46]. The FCT Systeme GmbH SPS machine can accommodate special tungsten carbide cobalt (WC-Co) punches that can withstand pressures up to 150 MPa on a 20 mm diameter punch (41.1 kN). There are other parameters to consider, including heating rate ($°C•min^{-1}$), dwell time (min), pulsing (whether constant or interval in ms), atmosphere (vacuum or inert gases), and cooling rate ($°C•min^{-1}$) [48]. Given the automation of the modern SPS machine, slowing cooling parameters can be 20 $°C•min^{-1}$ above 300 °C. The machine features both a thermocouple probe and optical thermometer. Experiments have documented the SPS pulsing patterns, denoted in milliseconds peaks, dictate the time of no current. The peaks denote an increase in the magnitude of the signalling peak voltage, while the base is the “off” time, or period of no current. This could be relevant with SPSing samples that can react with each other, for example, Si and Mo [49].

1.4.2 Ultra-high-pressure, high-temperature spark plasma sintering (HPHT-SPS)

SPS offers fast heating rates, high-temperature sintering, and appropriate pressures to consolidate refractory powders. This branch of SPS research uses ultra-high-pressure, high-temperature (HPHT) to sinter ceramic composites; compaction pressure plays a pivotal role over sintering temperature [50]. To achieve high pressure, a Bridgeman anvil apparatus is used. The design is simple with two opposite flat surfaces where a pre-compact powder specimen is mounted. The apparatus imparts high pressure and, depending on the thickness of the specimen, high-pressure gradients due to the flow of the powder compact [51].

The photograph of the HPHT SPS machine from the Institute of Advanced Manufacturing Technology in Poland is found in Paper IV. The technology to sinter nanopowder compacts has advanced in recent years. These materials are increasingly important commodities and their creation into mixtures for composites as well as the experimentation to produce new material properties up to very high pressures will become increasingly prevalent [52]. Another area for the purpose of HPHT SPS is in the geosciences, such as the study of the Earth’s crust or mantel and core. The materials are exposed to very high pressures up to 500 GPa, where the materials in the mantel and core are fully dense and loaded in compression, unlike the powder material [53].

1.4.3 SinterHIP

SinterHIP technology is a form of thermal consolidation for cemented carbides where the application of heat and pressure is meant to densify the materials and close any remaining pores [42]. In this case, the pressure is usually supplied by introducing inert gas into the sintering chamber, thus providing holistic compaction of the sample and fully consolidates the carbide during the sintering process. The result is a product, which contains little to no porosity. The produced components are able to achieve full theoretical density. This technology has been used specially in heavy industries including the automotive, oil and gas, and aerospace to manufacture flawless components.

1.4.4 Plasma transferred arc (PTA) welding

PTA welding involves an open plasma flame where powder substrate is transported by a carrier gas torch to a welding torch as depicted in Figure 1.2. The substrate becomes molten by temperatures up to 3500 °C and solidifies to form a metallurgical bonded layer on the surface of a base metal, typically steel [26]. The bonded layer is called the hardfacing, and this layer can be reinforced by additional hard particulates, where the industrial standard is WC.

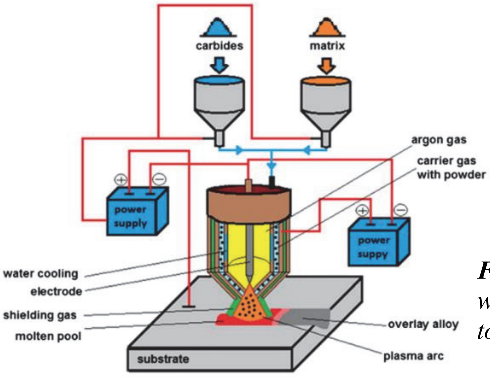

Figure 1.2 *Depiction of PTA welding with carbide and matrix powders gas fed to the weld torch [25].*

1.5 ZrC-based composites

ZrC-based composites are usually a combination of ZrC with other refractory hard materials, including W-ZrC [54], ZrC-HfC [55], ZrC-$MoSi_2$ [56], or ZrC-ZrO_2 [57]. This thesis will focus on two samples: zirconium carbide molybdenum (ZrC-Mo) and zirconium carbide-titanium carbide (ZrC-TiC). In previous research, it was found that a weight percentage of 20 wt.% either Mo or TiC into a ZrC composite offers an optimal balance of hardness and fracture toughness [35, 58, 59]. Hence, the composition of ZrC-20Mo and ZrC-20TiC will be the primary materials studied. ZrC-20Mo (~ZrC-14 vol.%Mo) was a ratio for the cermet sintered under vacuum up to 1900 °C with mechanical properties hardness HV10 1700 and by Vickers' indentation fracture toughness of 5.6 MPa•$m^{1/2}$. ZrC-20TiC (~ZrC-25 vol.%TiC) possessed a ratio of mixed carbide solid-solution vacuum sintered at 1900 °C with mechanical properties HV10 2070 and 5.8 MPa•$m^{1/2}$ using the same measuring principles [58].

1.5.1 ZrC-Mo system

Studies of Mo-ZrC cermets include arc melting for fusing composites at 2000 °C in Ar [60, 61]. Landwehr et al. [8, 62-64] did experiments with ZrC-Mo composites sintered in carbon and carbon-free environments up to 2200 °C. ZrC and Mo could be densified by liquid phase sintering; however Mo_2C formation was due to Mo in a carburising environment. The lack of available Mo in the system defeated the goal producing a viable cermet. Mo_2C was not found after 2100 °C in the graphite-free atmosphere, confirming the existing phase equilibria in the Zr–Mo–C system [62, 63]. However, graphite is an very important tool in sintering at high-temperatures. Protective gases would need to be employed leading to sintering in a pressureless environment. For a ZrC-40 vol.%Mo cermet, using hot isostatic pressing (HIP) at 1800 °C for 200 MPa for 1 h, yielded an indentation fracture toughness value of 6.6 MPa•$m^{1/2}$ with approximately 380 GPa Young's modulus value [64]. ZrC particle reinforced into Mo sintered by SPS double the strength and plastic elasticity [65]. Studies involving the SPS of pure Mo show that given the speed and the efficient concentration of heat during sintering, the penetration depth reaction between the graphite and Mo could be held to a minimum. Even with Mo carburisation, the penetration depth would be no more than 200 µm [66]; grinding or polishing would remove any traces.

1.5.2 ZrC-TiC system

The ZrC-TiC composite possesses a miscibility gap, where the dissolution of ZrC into TiC and vice versa creates a mixed carbide solid solution depending on the molar ratio of one carbide to the other. The sintering of ZrC-TiC solid solution is favoured towards the ZrC absorbing the TiC. The replacement of larger Zr ions by smaller Ti ones is easier than vice versa and thus the miscibility gaps are asymmetric [67, 68]. Alternatively, to form ZrC-TiC solid-state solution would require adjusting molar ratios and a similarly high sintering temperature (> 2000 °C) [68, 69]. Thermodynamic evaluation of the TiC-ZrC system has been done by Markstrom et al [70] where it was estimated that a composite of ZrC-20TiC (approximately ZrC_X-TiC_{1-X}, where x = 70 mole fraction) has a miscibility gap at ~1850 °C. The mixed (Ti,Zr)C phase should be stable above this temperature, but decomposes into TiC and ZrC at lower temperatures. Borgh et al. [71] suggested that mixed carbides could be used as a strengthening constituent. It is believed that the new superhard mixed carbide has a high potential in various engineering applications such as cutting tools, and in surface coatings [72]. Previous research into ZrC-TiC composites shows grain size refinements in TiC–ZrC solid solutions, the mechanical properties of Vickers hardness and indentation fracture toughness are significantly increased when compared to monolithic TiC or ZrC. Liu et al. [67] performed SPS experiments on TiC-ZrC composites with a molar fraction, $Ti_xZr_{1-x}C$ where x = 0.3, which is approximately ZrC-20TiC. They reported the following mechanical properties: HV1 = 20 GPa, K_{IC} = 6.5 MPa•$m^{1/2}$, and Young's modulus 370 GPa, signals a twofold increase in fracture toughness compared to pure ZrC. SPS compaction pressure in their experiments was kept at 50 MPa, constant pulsing.

1.6 ZrC-doped composites

1.6.1 Additives to hardmetals

Existing research has largely focused on using other carbides, namely vanadium carbide (VC) and chromium carbide (Cr_3C_2) [73, 74] as additives, which improves the sliding wear resistance of WC-Co. TiC has been known to flatten the shape of the WC grain into triangular prisms, thus increasing its hardness and strength [75]. By adding trace ZrC, the carbide segregates to the hardmetal, inhibiting grain growth in WC systems [4]. However, there is little research done on the tribological performance of adding ZrC to WC-based cemented carbides.

1.6.2 Hardface reinforcement to metal matrix composites (MMCs)

MMC is a metal base binder possessing ductility and toughness. A commercial substrate for example, could be the Ni-based superalloy, NiCrBSi, a matrix powder used in high temperature wear-resistant coatings. A common reinforcement added is WC/W_2C, which further enhances both the impact and abrasion resistance [6]. However, other carbides can also be used, with each giving unique properties to the MMCs: Cr_3C_2 enhances corrosion resistance, TiC increases wear resistance to erosion and abrasion [26]. ZrC has not been considered as a reinforcement additive due to its high cost. However, ZrC could offer even better high-temperature wear resistance than WC. ZrC decreases the thermal conductivity and thermal diffusivity of the composite; as a result, even at ultra-high-temperatures, the composite remains resistant to ablation effects due to oxidation [32].

1.7 ZrC oxidation

ZrC is classified as an UHTC characterised by the ability to handle temperatures up to 2400 °C and superior thermal capability compared to SiC [76]. However, it has been well documented that pure ZrC has poor high-temperature chemical stability against an oxidising atmosphere [77, 78], thus limiting its potential application as a UHTC. ZrC oxidation begins at as low as 600 °C depending on oxygen partial pressure, where a *c*-ZrO_2 compact phase is formed preventing further oxidation of carbon in ZrC [12, 34]. At higher temperatures beyond 800 °C, with a higher partial pressure of oxygen, ZrC quickly oxidises into either monoclinic and/or tetragonal ZrO_2 oxide scales consisting of a porous and cracked outer layer [79]. The resulting oxides offer virtually no protection against further oxidation, confirmed by extrapolated linear oxidation kinetics [80]. As a response, various avenues of research exist to alloy ZrC with other compounds and elements to enhance the oxidation resistance of ZrC. One of the compounds alloyed to ZrC to enhance oxidation resistance is silicon carbide (SiC) since the resulting silicon oxide (SiO_2) is supposed to form a more protective oxide layer. However, the available research seems to portray conflicting results concerning SiC and ZrC. Zhao et al. [81] tested ZrC-30 vol.% SiC in air between 800 and 1500 °C, but found that SiC turned into SiO_2 only offered protection at the higher temperature range, not at any temperature lower than 1100 °C. On the contrary, Ma et al. [82] experimenting with ZrC-20 vol.% SiC claimed that oxidation resistance, in accordance with mass change, was better below 1000 °C. The kinetics of ZrC alloy oxidation seems to be dependent on the composition of the alloying compound, in this case, SiC. A later study [77] with ZrC-SiC found that higher concentrations (~30 wt.%) of SiC exhibited better ZrC oxidation protection at lower temperatures (~1500 °C) compared to lower concentration (~10 wt.%) performance, offering better protection at higher temperatures (~1800 °C). The variables at play during oxidation are complex and numerous. Since most experiments are done in static air conditions where variables, such as partial pressure of oxygen that can influence oxidation kinetics, are not taken into account. For example, lower oxygen partial pressure improved the oxidation resistance of ZrB_2-SiC ceramics [83]. The composites of ZrC-20Mo and ZrC-20TiC have not had oxidation mechanisms and behaviours previously studied.

1.8 Objectives of the study

The motivation for this work is the urgent need for a well-developed processing methods allowing remarkable mechanical properties of the multifunctional and industrially applicable final product as well as the knowledge-based design of the ultra-high-temperature ceramic-based composites. New horizons for products directly connected to processing routes can fill an intense need in innovative materials to perform in challenging conditions.

The ***overall objective*** of the study is to bring together knowledge on the manufacturing of composites of commercial interest, using advanced sintering techniques and microstructural engineering. Current research is concentrated on the development of **ZrC-20Mo** and **ZrC-20TiC** composites and their analysis in terms of microstructure, mechanical and high-temperature properties.

Furthermore, two diverging investigations extend the research into using **ZrC** or **TiC** as **additives** for cemented carbides, or as **hardfaced reinforcement** for metal matrix composites. In the first instance, ZrC or TiC is incorporated into hardmetal WC-8wt%Ni and subjected to tribological tests including low and high stresses. In the second stream, ZrC and TiC are sintered with Ni and incorporated into a metal matrix composite via plasma arc transferred weld coating, before being subjected to high-temperature abrasion and impact wear conditions.

The ***main tasks*** of this work are twofold: (1) to investigate the mechanical properties and oxidation behaviour of ZrC-based composites and to improve the fracture toughness and temperature stability of the composites over pure ZrC; (2) to study the wear behaviour, including high-temperature abrasion wear of ZrC-doped hardmetals and hardfaced coatings.

The goals related to the objectives are as follows:

1. Optimisation of the SPS parameters to sinter ZrC-20Mo and ZrC-20TiC composites;
2. Mechanical, structural, and chemical characterisation of the sintered materials;
3. Examination of the formation of new phases during sintering and their effect on the mechanical properties;

4. Studying the effect of ultra-high pressure SPS on the sinterability of the materials and their properties;
5. Analysis of the oxidised ZrC-composites' microstructure and chemical characteristics up to 1500 °C;
6. Studying the tribological behaviour of WC-Ni doped with ZrC and TiC under low and high abrasion, wet and dry erosion;
7. Optimising the integrity of ZrC and TiC reinforced hardfacing via PTA welding metal matrix composite;
8. Studying the tribological behaviour and properties of ZrC and TiC reinforced PTA welded hardfacing in high-temperature oxidation conditions.

2. MATERIALS AND METHODS

2.1 Powder preparation

For ZrC composite research, Figure 2.1 gives an overall view of the pathway of activities for this research. Commercially purchased powders were milled, then SPS followed testing in various matters. Detail methods for each samples powder preparation can be found in each of the four Papers I-IV.

For the PTA welding experiments, commercially available powders of TiC (2-5 µm, Strategic Metal Investments, 99 % purity), ZrC (2-5 µm, Strategic Metal Investments, 99 % purity), and Ni (20 µm, Norilsk, 99 % purity) were used to synthesise the cermet particulates of TiC-10wt.% Ni and ZrC-10wt.% Ni. Carbides were mixed with 10 wt.% Ni in a mechanical ball mill with ethanol and 1 wt.% paraffin for 48 h, as described elsewhere [27]. The mixture was dried, granulated, and vacuum sintered at 1500 °C for 30 min. The carbide reinforcement was then combined during PTA welding with NiCrBSi based alloy.

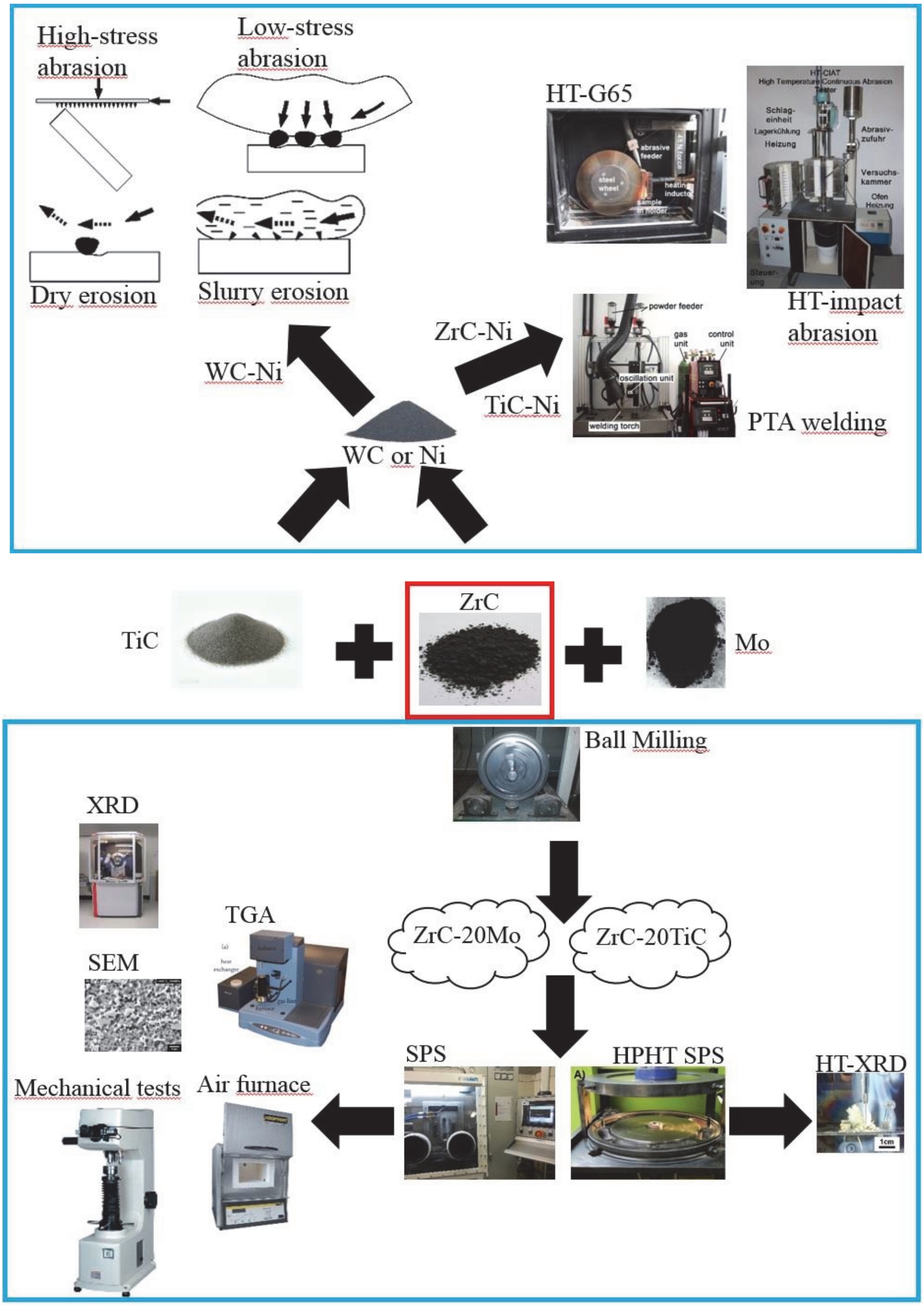

Figure 2.1 *Schematic pathway of activities: ZrC-based composites via SPS ZrC-20Mo and ZrC-20TiC (bottom); ZrC-doped composites into cemented carbide and PTA coating (top).*

2.2 Spark plasma sintering

Three spark plasma sintering machines were used during this research. The first SPS (Dr. Sinter SPS-1050-CE) was used to sinter powders under argon between 1600-1900 °C. This SPS could compact samples up to 100 MPa (20 mm dies) and at temperatures up to 2000 °C. The heating rate can be adjusted from relatively slow 100 °C•min^{-1} up to fast 1000 °C•min^{-1}, followed by a dwelling time at the final sintering temperature. This SPS was used to sinter ZrC-20TiC composites in the first series of examining mechanical properties.

The SPS furnace (FCT Systeme GmbH) sinters powders under vacuum or protective atmosphere between 1600-2200 °C. As rated by the manufacturer, this SPS machine has an upper limited compaction pressure with the standard graphite moulds rated at 50 MPa. However, by changing the grade of graphite and manufacturing customised dies and moulds, the compaction pressure for this SPS could be changed to be used up to 100 MPa. Both SPS machines use 20 mm diameter graphite (5 µm, Carbone of America, Grade 2333) cylindrical moulds, the compaction pressure up to 100 MPa and at temperatures up to 2200 °C. Due to the automation of the system, the sintering program can also be set to slow cool samples after final dwelling. This latter SPS was used to sinter all other samples of ZrC-20Mo as well as ZrC-20TiC for later high-temperature oxidation testing.

2.3 Ultra-high-pressure, high-temperature spark plasma sintering

An ultra-high-pressure, high-temperature (HPHT) spark plasma sintering (SPS) machine was used to examine the effect of high compaction pressure on the mechanical properties of sintering ZrC composites. The HPHT SPS equipment consisted of a high pressure (7.8 GPa) hydraulic press equipped with a Bridgman anvil, and a direct-pulsed current generator with an accompanying computer control system. The specifics of HPHT SPS are detailed in Paper IV.

2.4 High temperature oxidation

Oxidation tests were carried out in a Nabertherm (L9/13) static air furnace with a PID P330 controller in laboratory air between 600-1200 °C, at intervals of 200 °C. The experiment was setup so that separate samples were exposed at each temperature point only once before cooling via the ambient atmosphere.

The furnace heating rate was set to be 12 °C•min^{-1} for an 1 hour dwell time at each temperature point. Prior to testing, the SPSed samples were mechanically ground and polished with diamond abrasives to a 1 µm finish. They were then cleaned in an ultrasonic acetone bath, dried, before being weighed, using an electronic balance with accuracy 0.0001 g.

2.5 SinterHIP

Sintering the WC-8Ni hardmetals doped with ZrC or TiC was carried out in a FCT-system (FPW-300-400 Sinter-HIP furnace, Germany). Sintering temperature was ramped up to 1450 °C, then pressurised in argon up to 30 bars. The parameters are shown in Figure 2.2, detailing the ramp rates and more information found in Paper III.

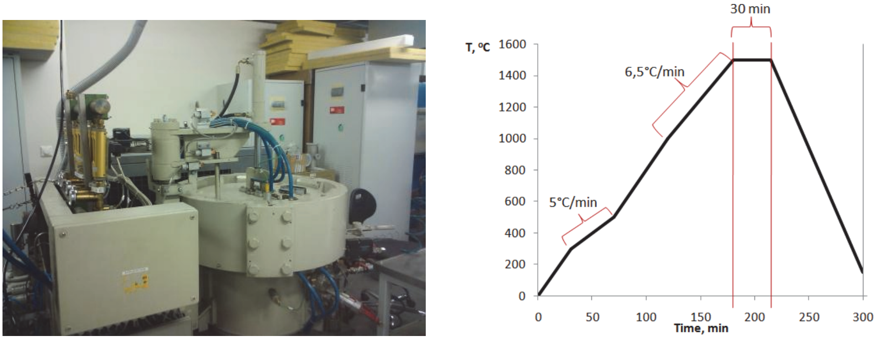

***Figure 2.2** SinterHIP machine with an accompanying sintering regime diagram.*

2.6 Plasma arc transferred (PTA) welding

NiCrBSi alloy powder (0.2 wt.% C, 4 wt.% Cr, 1 wt.% B, 2.5 wt.% Si, 2 wt.% Fe, rest Ni) with particle size of 50-150 µm was used as a matrix material for the PTA process. Hardfacing layers of the NiCrBSi matrix with reinforced cermet particles TiC-Ni and ZrC-Ni were deposited onto an austenitic stainless steel substrate using an EuTronic® Gap 3001 DC apparatus under the parameters set in Table 2.1.

Table 2.1 *PTA welding parameters for ZrC-Ni and TiC-Ni reinforced hardfacing.*

Parameter	**ZrC-Ni reinforcement**	**TiC-Ni reinforcement**
Welding current [A]	77	70
Oscillation speed [mm s^{-1}]	17.5	20
Oscillation width [mm]	20	20
Welding speed [mm s^{-1}]	1.05	1.3
Substrate material	austenitic steel	austenitic steel
Carrier gas & flow [L min^{-1}]	Ar or H_2	Ar or H_2

2.7 Thermogravimetric analysis

To determine the weight change of the ZrC composites during oxidation at high temperature, a thermogravimetric analysis (TGA) was done. The TGA uses a NETZSCH STA 449 ***F3*** *Jupiter®* thermal analyser with differential scanning calorimetry (DSC). The system contains a high heating rate furnace, which is capable of operating in the temperature range of 30-1250 ºC. The system is air tight, therefore, allowing measurements to be conducted under precisely defined atmospheres. The software, NETZSCH Proteus 6.1.0, allows the computation of the rate of mass change, mass change steps, onset and peak temperature, peak area integration etc. The samples were analysed in Al_2O_3 crucibles without lids. The used heating rate was in all cases 20 °C•min^{-1}. The used atmosphere was 20 % O_2 and 80 % N_2 to simulate the effect of ordinary air. The result is a detailed minute-by-minute measurement of change in weight versus time. For these experiments, ZrC composites weight change was measured between room temperature (RT) and 1200 °C with 1 h dwell times at 800 °C, 1000 °C, and 1200 °C.

2.8 Testing mechanical properties

Archimedes' method was used to determine specimen density with distilled water. The bulk Vickers' hardness with Indectec machine was set to HV10. In some samples, HV1 low load Indectec indenter was used to measure samples to maintain consistent comparison. For transverse rupture strength (TRS), a low-speed rotary saw cut samples to appropriate sizes. Samples were polished to 3 µm; an Instron 8802 press performed three-point bending tests. The indentation fracture toughness (IFT) was calculated by resorting to the Palmqvist method [84], specifically the Evan and Wilshaw's equation (2.1):

$$K_{IC} = 0.079\frac{P}{a^{3/2}}\log(4.5\frac{a}{c}) \qquad (2.1)$$

where P is load in newtons, a is indent length, and c is propagation crack length. Indentation testing for Young's moduli was done on personal computer controlled Zwick 2.5/TS1S rig with a Vickers indenter at 10 N load [85]. The reported mechanical properties constitute the mean standard deviation values of 6 indentations. Alternatively, some samples were measured using a Panametrics Epoch III ultrasonic wave transition device to determine Young's modulus. The calculations were carried out according to the following formula:

$$E = \rho \bullet C_T(3\frac{C_L^2}{4C_L^2} - \frac{C_T^2}{C_T^2}) \qquad (2.2)$$

where E – Young's modulus, ρ – density of the material, C_L – velocity of the longitudinal wave, C_T – velocity of the transversal wave.

2.9 Tribological tests of ZrC doped composites

The hardmetals doped with ZrC or TiC were subjected to a series of increasing aggressive stress tests. Specific test parameters can be found in Paper III, Materials and Methods section.

2.10 HT abrasive wear testing

PTA welded ZrC-Ni and TiC-Ni reinforced hardfacings were subjected to HT cyclic abrasion (hot ASTM G65) and HT cyclic impact abrasion testing, shown in Figure 2.3. The hot G65 test featured a steel wheel with flowing Ottawa silica and induction heating up to 700 °C with the following test lasting for 10 min. The cyclic impact abrasion test featured a CoCrMo-base plunger (Stellite 21) also with flowing Ottawa silica abrasive. The plunger impacts the sample at 45° with an energy of 0.8 J and frequency of 2 Hz [25].

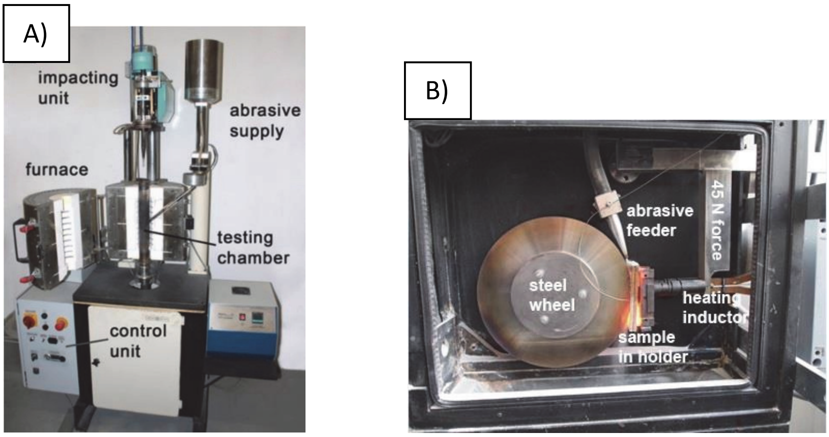

Figure 2.3 *A) Impact abrasion wear tester [25]; B) hot G65 abrasion wear tester both able to achieve 700 °C testing environment, photo copyrighted from AC2T.*

2.11 Microstructural characterisation

The microstructural analysis was done under SEM (FE-SEM Hitachi S-4700 and TM-1000, Japan) after etching with $HF:HNO_3:H_2O$ (1:1:2 vol.%) solution for 10 s. Surface analysis via SEM was done as-is after high temperature oxidation in static air furnace, while cross-section microstructural analysis was done after polishing to a 1 µm finish with diamond abrasive.

Chemical composition was analysed with X-ray diffraction analysis (XRD, Philips PW3830 X-ray Generator, 4 kW, Cu-Anode) using CuK_{α} radiation. The accelerating voltage was 40 kV with a filament current of 30 mA, a scan step size of 0.02°, and a count time of 0.4 s at each step. These parameters are applicable to equipment at TUT. Cooperation with the Institute of Advanced Manufacturing Technology included access to their high-temperature x-ray diffraction machine. Chemical composition was analysed with X-ray diffraction (Empyrean, by PANalytical equipped with high-temperature chamber Anton Paar HTK 2000N) by using the copper radiation (λCu Kα = 1.5418 Å). The measurements were carried out at the following temperatures: RT, 800 °C, 1000 °C, 1200 °C and 1500 °C in air. The HT-XRD parameters involved a heating rate of 20 $°C•min^{-1}$, with each dwell time lasting for 30 min before taking 1 h to do XRD scans at the dwell temperature.

3. RESULTS AND DISCUSSION

3.1 ZrC-TiC, conventional SPS

ZrC-20TiC was subjected to SPS at either 1600 or 1900 °C with either a pressure of 50 MPa or 100 MPa at both temperatures. The exact SPS parameters are outlined in Table 3.1. The goal of this work was to determine the influence of different compaction pressures on the sintered composites, while maintaining the temperature and all other parameters constant. The results include analysis of mechanical properties and microstructure analysis.

Table 3.1 *SPS parameters for ZrC-20TiC*

Samples from conventional SPS	Heating rate [°C ·min^{-1}]	Dwell time[min]	Temperature [°C]	Pressure [MPa]
A	100	10	1600	50
B	100	10	1600	100
C	100	10	1900	50
D	100	10	1900	100

Table 3.2 *Mechanical properties of the samples tested from* ***Table 3.1***

Samples from conventional SPS	Relative density [%]	Hardness, HV10	Indentation Fracture Toughness, K_{IC} [MPa·m$^{1/2}$]	Transverse rupture strength [MPa]
A	98.1	2012 ± 48	3.8 ± 0.7	488 ± 7
B	98.5	1898 ± 53	5.4 ± 0.5	688 ± 134
C	103	1640 ± 41	4.1 ± 0.5	648 ± 5
D	101.7	1731 ± 26	4.1 ± 0.5	742 ± 56

First, Table 3.2 reveals the non-characteristic representation of relative density in with values that exceed 100 %. It is safe to say that grain growth or grain coarsening is not a plausible cause for such change in values based on the law of conservation of mass. Therefore, a chemical change must take place in the material, which would affect its density. XRD analysis on samples B and D at the two sintering temperatures show different chemical compositions. Figure 3.1 shows that at 1900 °C, ZrC-20TiC sintered with 100 MPa shows peaks of a solid-state (Zr,Ti)C phase. The higher sintering temperature leads to the formation of (Zr,Ti)C; the miscibility gap for ZrC-20TiC is estimated to be at ~1900 °C [55]. According to the thermodynamic evaluation of the TiC-ZrC system done by Markstrom et al. [70], a composite of ZrC-20TiC (approximately ZrC_X-TiC_{1-X}, where x = 70 mole fraction) has a miscibility gap at ~1850 °C. Hence, with the change in chemical composition from a carbide-carbide to a mixed carbide composite, this is reflected in samples C and D having densities that exceed 100 % compared to theoretical densities.

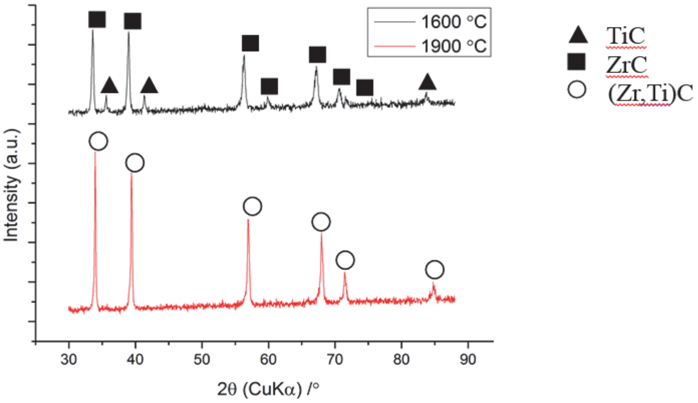

***Figure 3.1** XRD patterns of ZrC-20TiC at 1600 °C (top, black) and 1900 °C (bottom, red), respectively, samples B and D from **Table 3.1**.*

Previous research involving sol-gel synthesis of the TiC-ZrC composite also features SPS using 100 MPa compaction pressure to consolidate the powders [86]. The paper stated the hardness and indentation fracture toughness to be 2244 (HV5) and 3.2 MPa•m$^{1/2}$ respectively for a sample of 1:1 mol TiC-ZrC (approximately ZrC – 63 wt.% TiC) composite. This composite was produced from SPS using a compaction pressure also of 100 MPa, but at the temperature of 2000 °C. The research with ZrC-20TiC revealed that high compaction pressures during SPS are detrimental to fracture toughness values during sintering at 1900 °C.

The major finding from Paper I shows that TiC exists as a secondary phase in the ZrC-20TiC sintered at 1600 °C with a 100 MPa compaction pressure. The presence of TiC explains the difference in the mechanical properties in Table 3.2, where sample B shows the highest indentation fracture toughness at 5.4 MPa•m$^{1/2}$. A separate experiment also confirms the Young's Modulus value for sample B to be 347 GPa. The higher compaction pressure will also improve the transverse rupture strength value of sample B, with a value of 688 MPa usually seen with higher sintering temperatures. This is an indication that high pressures at relatively low sintering temperatures consolidate the composite material, but the lower temperature also inhibits the miscibility gap formation to form mixed solid solution carbides. Under high-resolution SEM, it is clearly evident that during crack propagation for sample B, the secondary TiC phases act like crack deflectors, Figure 3.2A. The crack stops and deviates around the TiC grain. Figure 3.2B reveals the crack propagating underneath the TiC particle forming a bridge.

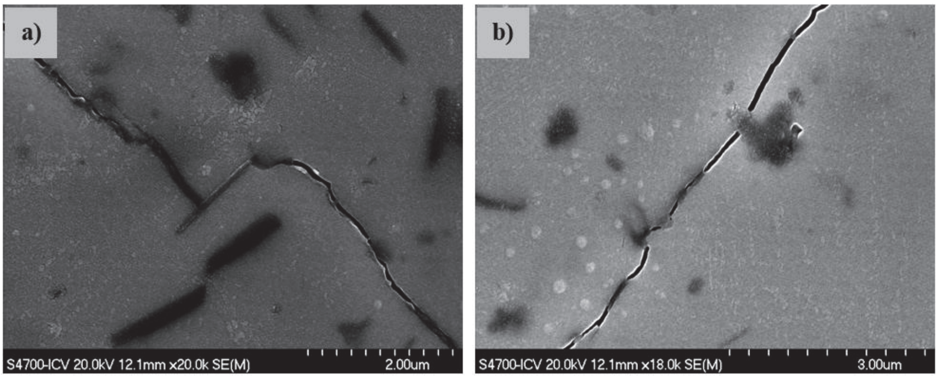

Figure 3.2 *Sample B, ZrC- 20TiC sintered at 1600 °C with pressure 100 MPa showing a) crack deflection and b) bridging with TiC grains.*

Resulting from early research published in Paper I, it is concluded that high compaction pressure during conventional SPS works to improve the fracture toughness of ZrC- 20TiC composite by inhibiting the miscibility gap of the composite, but still achieving close to full densification according to SEM images and density measurements. Higher sintering temperatures drive the formation of the miscibility gap for ZrC-TiC creating mixed carbide solutions (Zr,Ti)C. This subsequently lowers the mechanical properties.

3.2 ZrC-Mo, conventional SPS

ZrC-20Mo composite was studied with SPS in a series of tests between 1600-2100 °C with either a pressure of 50 or 100 MPa. The exact parameters are outlined in Table 3.*3*. It was explained in Paper II that modifying the SPS machine to accommodate compaction pressures up to 100 MPa was not a problem for ZrC-20TiC, but resulted in complications with sintering ZrC-20Mo cermet. While using 50 MPa, sintering could be done up to 2100 °C without incident; however, applying 100 MPa caused complications during post sintering. All samples sintered with compaction pressure 100 MPa survived the sintering intact. The moulds did not break during sintering; but they cracked when trying to extract the samples at room temperature. Apparently, the 100 MPa compaction pressure caused the material to extrude at the centre of the die, bulging the mould. SPS using 100 MPa of pressure at temperatures above 1700 °C resulted in mould breakage.

Table 3.3 *SPS parameters for ZrC-20Mo*

Sample	Heating rate [°C•min^{-1}]	Dwell time[min]	Temperature [°C]	Pressure [MPa]
A	100/300	5	1600	50
B	100/300	5	1900	50
C	100/300	5	2100	50
D	100/300	5	1600	100
E	100/300	5	1700	100
F	100/300	5	1800	100
G	100/300	5	1900	100

ZrC-20Mo's relative density decreases with rising sintering temperature. This could be explained by the decreasing fraction of pure Mo, having higher density (10.3 g•cm^{-3}) compared to MoC (approximately 8.78 g•cm^{-3}) due to Mo carburisation. With 100 MPa compaction pressure, the relative density of the cermet is increased by 1 percent compared to samples pressed at 50 MPa [Paper II]. The density results are reflective of the master sintering curve of Mo, hence the higher compaction pressure rises the activation energy of Mo [87]. Neither does the theoretical density also does not take into account the formation of mixed solid solution carbides.

***Table 3.4** Relative density and mechanical properties of the composites of ZrC- 20Mo at different SPS parameters.*

Sample	Relative density [%]	Hardness, HV10	Indentation Fracture toughness, K_{IC} [MPa•m$^{1/2}$]	Young‘s Modulus [GPa]
A	97.7	2139 ± 20	5.1 ± 0.5	300 ± 23
B	97.7	2174 ± 18	5.5 ± 0.6	346 ± 16
C	97.4	2231 ± 14	5.4 ± 0.6	396 ± 14
D	98.7	2051 ± 54	5.4 ± 0.6	374 ± 30
E	98.5	2065 ± 33	4.2 ± 0.6	353 ± 15
F	98.3	2157 ± 50	4.2 ± 0.6	294 ± 28
G	98.3	2139 ± 51	3.9 ± 0.6	291 ± 21

In Table 3.4, the Vickers' hardness increases with rising sintering temperature. There is an inverse trend between relative density and both hardness and Young's modulus. This can be attributed to a decrease Mo solid solution formation $(Zr_{50},Mo_{50})C$ intensity in XRD scans, which is at 42° (2θ) in Figure 3.3. At 2100 °C and 50 MPa, ZrC-20Mo possessed mechanical values of 2231 (HV10) and 5.4 MPa•m$^{1/2}$ along with the highest value for Young modulus at 396 GPa [Paper II]. High compaction pressure SPS, along with rising sintering temperature, has a negative effect on the mechanical properties that drop as much as 25 % on average.

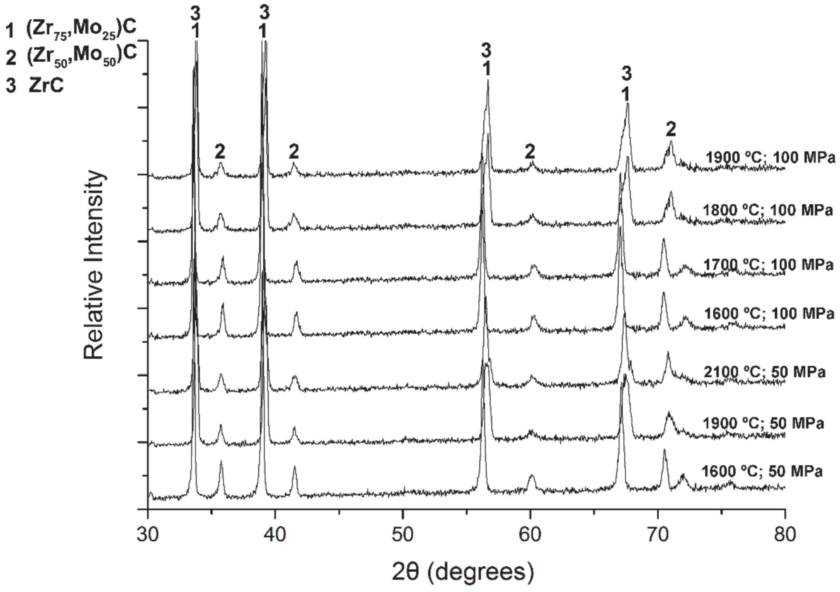

***Figure 3.3** ZrC-20Mo XRD spectra at various temperatures and pressures. ZrC is also detected, but it is shifted to the higher θ values.*

In all samples tested, ZrC was detected as (Zr,Mo)C regardless of the applied pressure. The intensity of (Zr,Mo)C increases with increasing temperature, as seen in Figure 3.3. Free Mo is not detected in XRD, instead Mo exists in the solid solution, $(Zr_{50},Mo_{50})C$. Raising the sintering temperature from 1600 to 2100 °C saw a progressive decrease in the $(Zr_{50},Mo_{50})C$ intensity, due to further Mo dissolution into ZrC. The XRD show ZrC peaks shift to higher 2θ values compared to the normal stoichiometry. As seen in Figure 3.3, with the shifting ZrC peaks, the lattice parameter values also slowly decreases with increasing temperature. In work by Landwehr et al. [62, 64], ZrC higher 2θ values indicate Mo dissolution into ZrC. This was accompanied with an increase in solid solution of Mo with increasing Mo content up to 40 vol.% Mo in the ZrC-Mo composition. In this case, $(Zr_{75},Mo_{25})C$ species were detected as the ZrC absorbed Mo and shifted to the right. Detailed SEM images are published and discussed in Paper II to reiterate the findings by XRD.

ZrC-20Mo was studied under increasing SPS temperatures and two compaction pressures. Paper II showed that 100 MPa compaction pressure increases composite densification by 1 %, but deteriorated the mechanical properties, by promoting grain growth. Lower temperature and moderate pressure, 1600 °C and 50 MPa revealed a very clear ZrC grain structure and Mo solid solution $(Zr_{50},Mo_{50})C$ diffusion between carbide grains. Raising the sintering temperature to 2100 °C, while using a moderate pressure of 50 MPa saw the composite increase overall mechanical properties by yielding small clusters of $(Zr_{50},Mo_{50})C$ phases in the microstructure. This optimised SPS regime resulted in the following mechanical values: 2231 HV10 and 5.4 $MPa\cdot m^{1/2}$, and 396 GPa Young's modulus. ZrC-20Mo sintering is influenced by temperature, not pressure according to the two pressures studied.

3.3 Ultra-high-pressure, high-temperature spark plasma sintering

HPHT SPS allowed the use of tantalum foils thus sintering within a non-carburising environment. It is shown in Paper IV that the results of ZrC-20Mo and ZrC-20TiC that underwent HPHT SPS have similar mechanical results compared with conventional SPS. Near fully consolidated material was achieved in the very short dwelling time by HPHT SPS. Details of the procedures and methods are found in Paper IV. The mechanical properties of these samples are shown in Table 3.5 and compared with the same samples produced from conventional SPS. Paper IV concluded that ultra-high-pressure did not improve the cermet's properties at least when it comes to fracture toughness. This reinforces the notion that for the ZrC-Mo composites, the sintering temperature affects the bulk density of the sample [63].

Table 3.5 *Mechanical properties of samples synthesised by HPHT SPS and SPS*

HPHT SPS Samples	**Relative density [%]**	**Hardness, HV1**	**Indentation Fracture Toughness, K_{IC} [MPa•m$^{1/2}$]**	**Young Modulus [GPa]**
ZrC (1550 °C)	99.6	1450 ± 18	2.5 ± 0.4	326 ± 7
ZrC-20Mo (1950 °C)	98.6	2239 ± 38	5.4 ± 0.6	340 ± 7
ZrC-20TiC(1550 °C)	96.4	1896 ± 40	5.9 ± 0.3	319 ± 6
SPS Samples				
ZrC (2200 °C, 100 MPa)	99.7	1889 ± 56	2.8 ± 0.5	283 ± 15
ZrC-20Mo (1900 °C, 50 MPa)	97.7	2284 ± 65	5.5 ± 0.6	346 ± 16
ZrC-20TiC (1600 °C, 100 MPa)	98.4	2030 ± 96	5.4 ± 0.5	347 ± 18

With HPHT SPS, the mechanical values of ZrC-20TiC for hardness and toughness are comparable to those by Liu et al. [67]. Pure ZrC was also tested with HPHT SPS and the results show expected full densification comparable to normal SPS at 2200 °C. However, the mechanical hardness does not reflect the relative density values. The high compaction pressure plays a role in the initial stages of particle rearrangement and results in the destruction of agglomerates leading to densification through plastic or superplastic deformation [88] as mentioned in Paper IV.

The microstructure for all HPHT SPS samples is shown in Paper IV. For ZrC-20Mo the result show rounded ZrC grains, an indication of the eutectic reaction with Mo to form (Zr_{50},Mo_{50})C and (Zr_{75},Mo_{25})C, the solid solution of Mo and ZrC, respectively. This supports other research implying a shift in the ZrC peaks towards higher 2θ values at 33.3° and 39.3°, implying Mo dissolution into ZrC [64, 89]. The shift in XRD pattern is clearly shown in Figure 3.4 when the ZrC-Mo pattern is compared to the ZrC reference of a control sample also produced from HPHT SPS. The eutectic temperature between ZrC and Mo is not altered by the ultra-high-pressure compaction. ZrC will absorb the available Mo forming a solid solution (Zr,Mo)C at temperatures below 2100 °C [63]. The fracture toughness in the ZrC-20Mo composite is mostly attributed to solid solution strengthening.

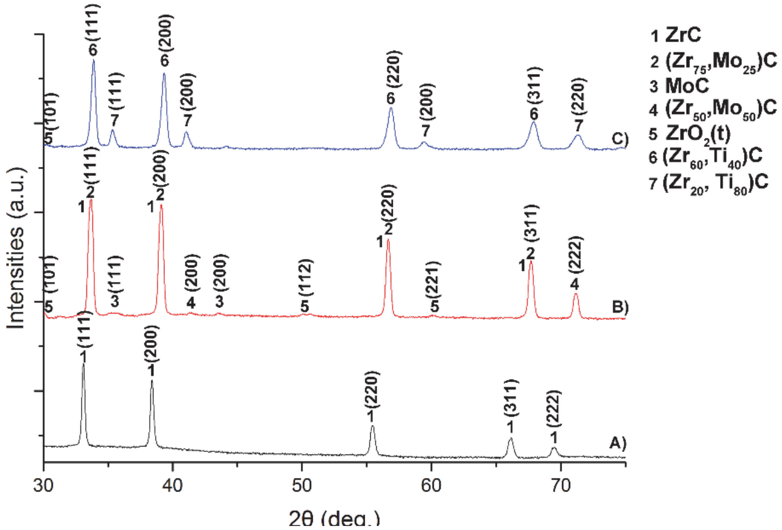

Figure 3.4 *XRD patterns of ZrC composites sintered by HPHT SPS: A) reference commercial ZrC sintered as-received, B) ZrC-20Mo, C) ZrC-20TiC*

The ZrC-20TiC composite shows a mixed, solid solution microstructure [Paper IV]. These results are in contrast with findings of Paper I where the 100 MPa pressure under conventional SPS produced no mixed carbide at 1600 °C, even after 10 min of sintering. HPHT SPS and sintering in a non-carburising environment did not inhibit the eutectic reaction between Mo and ZrC: Mo dissolution into ZrC still occurred and Mo was carburised forming MoC. HPHT SPS influenced ZrC-20TiC by lowering the miscibility gap temperature below the 1850 °C threshold. HPHT SPS has little influence on the mechanical properties of the composites

3.4 High-temperature XRD

HPHT SPS undergoing x-ray diffraction analysis at temperatures up to 1500 °C. Details of the phase changes for ZrC-20Mo starting from 800 °C, where the formation of oxide species ZrO_2 and MoO_3 is detected at 30.2°, 23° and 25° are revealed in Paper IV. MoO_3 is known to vaporise at this temperature range since it has a melting point at 790 °C [90]. MoO_3 vaporisation would suggest catastrophic breakdown (weight loss) and further expedite oxidation of (Zr,Mo)C phase. The HT-XRD experiment was halted after heating to 1200 °C because of the specimen's volumetric expansion.

XRD scan show the oxide peaks for ZrC-20TiC in Figure 3.5 are consistently strong between 1000 and 1500 °C, suggesting the surface oxide is stable as the temperature rises. At 1200-1500 °C, there is a mystery peak in the XRD scan at the theta 33°, which could be one of the two possibilities. The first possibility is due to the dissolution between ZrC and TiC producing mixed carbide solid solution species that also produces mixed oxide species during oxidation. Therefore, a species of $(Zr,Ti)O_2$ is likely a product of such composites. Another suspected identity for the mystery peak is ZrC at 33°, which is more plausible, given the species have already been detected as explained in Paper IV.

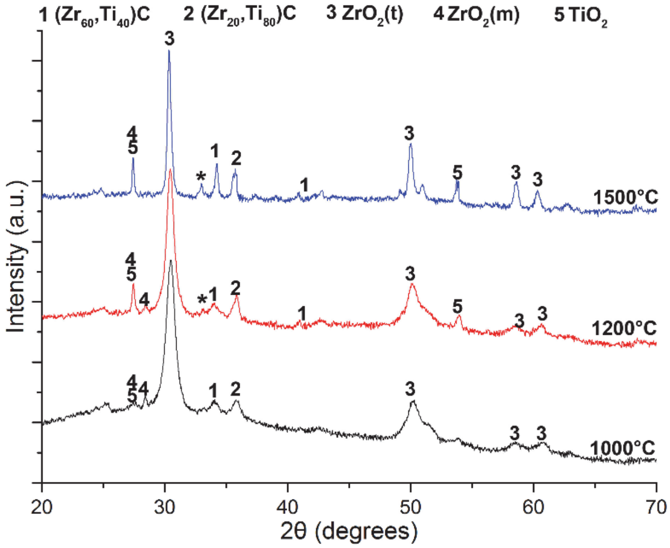

***Figure 3.5** HT-XRD of ZrC-20TiC produced from HPHT SPS. The symbols, *, are expected to be $(Zr,Ti)O_2$.*

3.5 High-temperature thermogravimetric analysis

ZrC-20Mo and ZrC-20TiC along with a sample of pure ZrC sintered by conventional SPS was prepared to undergo thermogravimetric analysis up to 1200 °C as per the limit of the machine. The samples were created from the parameters outlined in Table 3.6. The TGA machine is self-contained and measures the weight change constantly throughout the temperature ramp and dwell. The samples are exposed to simulated air (20 % O_2, 80 % N_2). It is well-known that ZrC undergoes rapid oxidation starting from approximately 700 °C and plateaus at 800 °C and beyond; most of the carbon formed will be oxidised into gaseous species rendering the protective layer useless [81]. Hence, the study was focused on temperatures from 800 °C onwards. The graph in Figure 3.6B reveals significant weight loss of ZrC-20Mo from 800 °C. The TGA supports the notion of catastrophic weight loss with ZrC-20Mo during temperature ramping to 1000 °C. MoO_3 volatilisation is the most likely cause of the rapid weight loss before stabilising again at 1000 °C. Further oxidation penetration occurs at this temperature followed by further volatilisation of MoO_3 in the next ramping to 1200 °C, evident by further weight loss.

***Table 3.6** SPS parameters of samples for HT oxidation studies*

Sample	**Heating rate [°C•min^{-1}]**	**Temperature [°C]**	**Dwell time [s]**	**Pressure [MPa]**
ZrC	100	2200	300	50
ZrC –20Mo	100/300	1600	300	50
ZrC –20TiC	100	1600	600	100

The TGA graphs show that the ZrC-20TiC composite follows similarly along the paralinear oxidation law of pure ZrC, Figure 3.6A, where the parabolic character of oxidation dominates in the initial part of the process [91]. The TGA of ZrC shows oxidation forming at 600 °C and plateauing thereafter towards 1200 °C indicates that the oxidation formation stops eventually. At this point, ZrC oxidation either has already proceeded completely through the sample or there is a protective layer formed. TGA for ZrC-20TiC (Figure 3.6C) shows little oxidation for the composite from 600-800 °C, but there is still steady weight gain up to a dwell point of 1000 °C. This would indicate steady oxide growth on the surface. Later analysis using SEM cross-section images was used to determine the penetration depth of the oxide growth. What is clear from the TGA graph is that ZrC-20TiC only undergoes significant oxidation and weight gain during the ramping rate towards 1200 °C. Yet the weight gain for ZrC-20TiC is still less than that for pure ZrC.

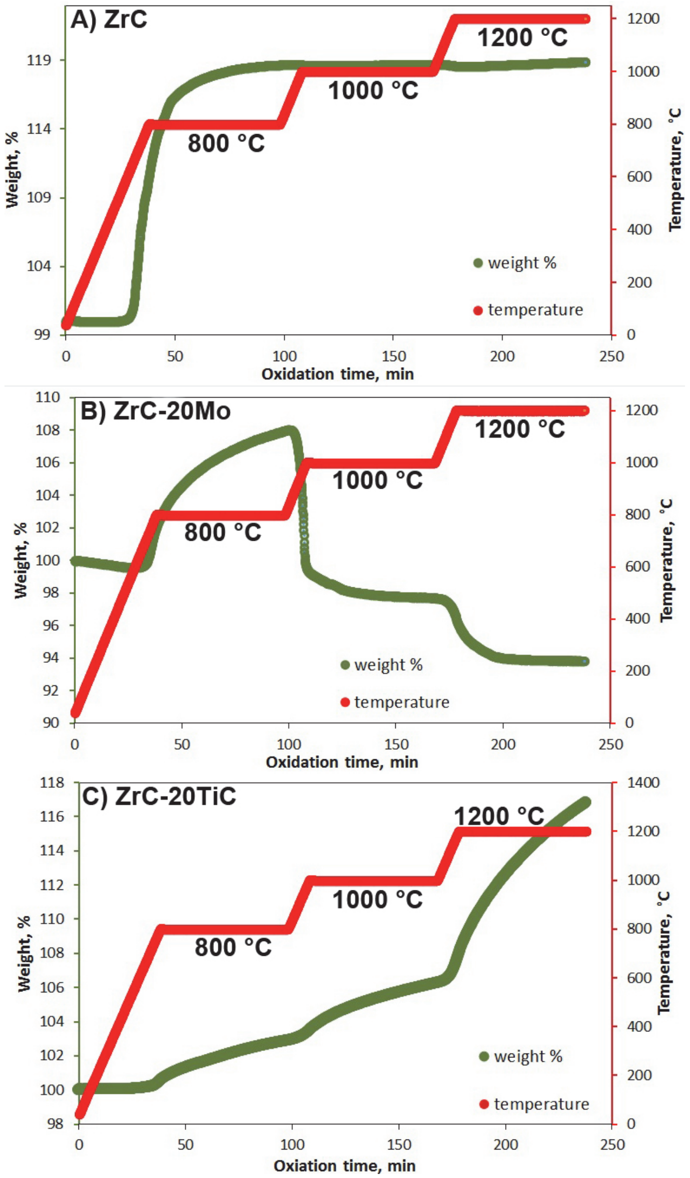

Figure 3.6 *TGA plots percent weight change between 800 – 1200 °C under simulated oxidation in air condition: A) ZrC, B) ZrC-20Mo, C) ZrC-20TiC.*

3.6 High-temperature oxidation in static air furnace

To examine the oxidation behaviour and morphology of the phase changes, a series of SPS samples were created in accordance with Table 3.6 for oxidation testing. However, these SPSed samples had to undergo control slow cooling at 33 °C•min^{-1} to prevent thermal shock and brittleness during grounding and polishing. Sample ZrC-20Mo here with slow cooling revealed the following properties: 2224 HV10 and 5.5 MPa•m$^{1/2}$ for hardness and fracture toughness respectively according to Paper II.

During the HT oxidation testing, individual samples from each of the three specimens of Table 3.6 were placed in the furnace and ramp to a designated temperature, dwelled for an hour, then cooled by ambient air flow. A new sample was apportioned for each new higher temperature point. Figure 3.7 shows the series of all three samples, including the ZrC reference after each stage of oxidation from temperatures 600 - 1200 °C. During the experimental research, a larger number of batch samples were needed for each high-temperature oxidation temperature. However, during the conventional SPS, some samples were produced with visible cracks after SPS, discovered during the grinding and polishing steps. The thermal stresses incurred during the SPS of the sample was attributed to the cracks as in conventional SPS experiment the sample is left to cool via ambient laboratory temperatures. This uncontrolled cooling was replaced with an additional step in the SPS program to allow for slow cooling. For all subsequent samples later synthesised for high-temperature oxidation testing, SPS program included a slow cooling regime of 33 °C•min^{-1}. In subsequent samples, slow cooling after SPS eliminated the cracks and breakages in the samples.

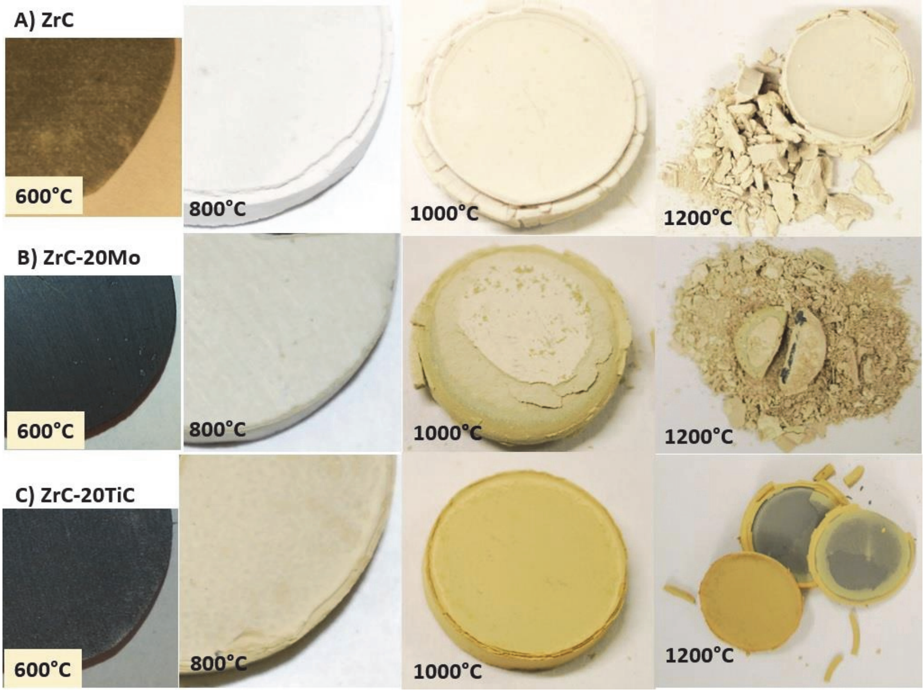

Figure 3.*7 Photograph after oxidation at different temperatures for 1 h then subsequent cooling to room temperature: A) ZrC, B) ZrC-20Mo, and C) ZrC-20TiC. Diameter of each SPS sample is 20 mm. Samples were synthesis according to Table 3.6.*

3.7 X-ray diffraction analysis after HT oxidation in static furnace

HT oxidation in a static air furnace for HPHT SPS produced samples underwent XRD after cooling the sample to room temperature. No other processing was done to the oxidised samples and only the surface was analysed. Both surfaces of ZrC-20Mo and ZrC-20TiC appear with a yellow hue. The vaporisation of MoO_3 has been known to give a light, yellow fume since its melting point is 790 °C [90]. XRD patterns of Figure 3.8 reveal that ZrC-20Mo is mainly composed of two species of (Zr,Mo)C solid solution in the native microstructure at RT. Therefore, when oxidation takes place, the reactions are as follows:

$$2Mo + 3O_2 \rightarrow 2MoO_3 \qquad (3.1)$$

$$ZrC + 2O_2 \rightarrow ZrO_2 + CO_{2(g)} \qquad (3.2)$$

$$ZrC + O_2 \rightarrow ZrO_2 + C_{(s)} \qquad (3.3)$$

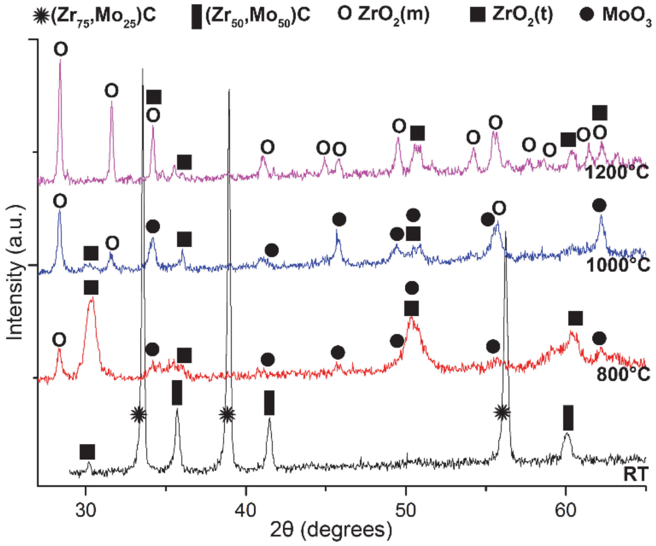

***Figure 3.8** XRD patterns of the surface of ZrC-20Mo at room temperature (RT), and then after 800 °C, 1000 °C, and 1200 °C.*

Typically, Mo alloy such as titanium-zirconium molybdenum (TZM) would volatilise by 800 °C, losing up to 33 % mass [92]. The diffraction intensity of

MoO_3 peaks is subtle at 800 °C, but increase intensity by 1000 °C before disappearing completely at 1200 °C. It is possible that the ZrO_2 phase forms a compact, closed-pore microstructure that acts as a diffusion barrier against oxygen transport [34] so that the local oxygen potential becomes too low to further oxidise Mo and ZrC. This would explain why Mo volatilisation, indicated by significant weight loss, is inhibited until about ~1000 °C according to Figure 3.6B, shown by a steep drop in weight loss. The oxidation temperature up to 1200 °C ultimately causes both ZrC and ZrC-Mo to suffer catastrophic structural damage in a phenomenon known as pesting: disintegration of material into powder [93]. MoO_3 vaporises from the external, cracked surface. Oxygen can then penetrate through the sample into cracks causing volume expansion furthering oxidation until the material is reduced to powder, as seen in Figure 3.7A and B, 1200 °C. MoO_3 is not detectable by XRD above 1000 °C, suggesting that all the surface traces were volatised leaving the remaining ZrO_2 powder. This is supported by TGA plots, which show progress weight loss during the temperature ramping portion of the experiment.

In Figure 3.8, it is important to note that additional oxidation could have occurred during the cooling regime after oxidation heating. Although chemically, the same powder was used for ZrC-20TiC and ZrC-20Mo, the two different SPS processes certainly changed the respective chemical compositions of each composite, however slightly. ZrC-20Mo was shown to have more MoC under HPHT SPS, while ZrC-20TiC produced mixed solid solution carbide at 1600 °C due to HPHT SPS. For the most part, the two XRD scans, whether from HT XRD of the HPHT SPS samples or XRD of the conventional SPS samples from air furnace, follow similar patterns and identifiable chemical species during oxidation. At 1200 °C, there is a contrasting difference; while HT-XRD show a single zirconia peak, there are a multitude of zirconia species in the post oxidation heating XRD for sample ZrC-20Mo. This can be attributed to the oxidation occurring during cooling, where passing through the temperature zone of 1000-800 °C, the remaining ZrC oxidised accordingly.

Out of all three samples, ZrC-20TiC is able to resist severe oxidation damage most effectively up to the highest testing temperature, 1500 °C. From the XRD patterns, Figure 3.9, ZrC-20TiC is sintered as a composition of ZrC and TiC since the higher pressure of SPS forces consolidation of the composite, but at a temperature below the miscibility gaps, inhibiting TiC dissolution into ZrC base on its miscibility gap producing a mix carbide solid solution [67, 70, 94]. Therefore, free TiC is still detected in XRD patterns at room temperature and these particles act as crack propagation deflectors, as shown in Paper I. The oxidation of carbides of group IV transition metals occurs through the formation of an oxy-carbide of the metal plus carbon [34, 78, 95], which is subsequently oxidised to CO and CO_2, eventually yielding metal oxides according to the reaction (3.4):

$$MeC + 2O_2 \rightarrow MeC_xO_y + C_{1-x} + O_{4-y} \rightarrow MeO_2 + CO_2 \qquad (3.4)$$

For ZrC-20TiC at 800 °C, the first signs of oxidation occur mainly with ZrO_2 (from reaction (3.2)) and TiO_2 formation reaction in air (reaction (3.5)). However, taking into account reaction (3.4), the following reactions are reasonable exceptations for ZrC-20TiC:

$$TiO_2 + 2O_2 \rightarrow TiO_2 + CO_{2(g)} \qquad (3.5)$$

$$ZrC + TiC + 3O_2 \rightarrow (Zr,Ti)C_xO_y + C_{1-x} + O_{4-y}$$
$$\rightarrow (Zr_{85},Ti_{15})O_2 + 2CO_{2(g)} \qquad (3.6)$$

Much of the ZrC-20TiC oxidation reaction would follow the route of reaction (3.6) with the mixed carbide solid solution oxides, which is seen in XRD scans starting from 800 °C. It is not clear why ZrC and TiC would oxidise into a mixed carbide structure. $(Zr,Ti)O_2$ solid solution formation is dependent on the pressure and temperature; srilankite was synthesised at 28 kbar and 1440 °C in equilibrium with rutile [96]. There is strong indication for reaction (3.6), based on the assumption that the TiC is fully stoichiometric [97], with strong diffraction peaks at 27° and 36° identified as rutile TiO_2 [98] evident in Figure 3.9, 800-1200 °C. It is also known that ZrO_2 and TiO_2 both have a strong diffraction peak at approximately 27°, which means the suspected mixed oxide peak seen at 1000 and 1200 °C could be an overlapping peak. However, the same cannot be argued for the peak seen at ~32° at 1000 and 1200 °C, which indeed fits with the $(Zr,Ti)O_2$ solid solution presented in other studies [96].

Rutile possesses a slight yellow tinge in its native form, but the most likely explanation for the yellow hue (Figure 3.7C) during ZrC-20TiC high temperature oxidation comes from the yellow pigmentation of monoclinic zirconia as typically happens between 800-1300 °C [99] and supported by the peak intensity of monoclinic ZrO_2 increases between 1000-1200 °C in the XRD. $(Zr,Ti)O_2$ solid solution is a dominate species during the high temperature oxidation testing with increasing diffraction peak intensity between

1000-1200 °C at 27° and 63° (Figure 3.9). It is possible that the synthesis process during SPS could lower the required activation of ZrC and TiC to beable to form $(Zr,Ti)O_2$ at temperatures below that indicated in literature.

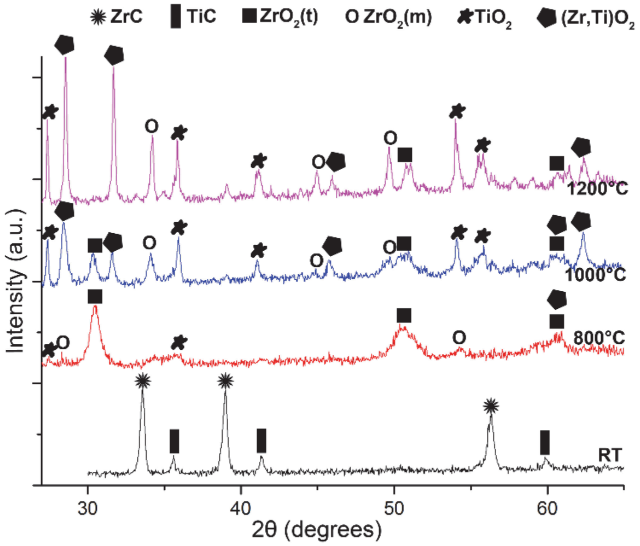

Figure 3.9 *XRD patterns of the surface of ZrC-20TiC at room temperature (RT), and then after 800 °C, 1000 °C, and 1200 °C.*

3.8 SEM analysis of HT oxidation

SEM images of the oxidation process of ZrC-20Mo and ZrC-20TiC were taken between 600-1200 °C after one hour at each temperature. During the experiment, a new sample was used at each temperature oxidation point. The surface of Figure 3.10A shows that even at 600 °C, there is visible depressions of Mo $(Zr_{50},Mo_{50})C$ and etching around the ZrC $(Zr_{75},Mo_{25})C$ grains. There is a clear separation line between zirconia-rich, darker layer with white spots of MoO_3 contrasted to the lighter, unaffected ZrC-Mo layer (Figure 3.10B) in a cross section after the 800 °C test. Figure 3.10C reveals an interlayer between the depleted outer ZrO_2 and MoO_3 layer at 1000 °C (Figure 3.10D), which is shown to be porous from the MoO_3 volatilisation, and an unaffected native layer. EDS scan supports the idea that the surface layer is composed primarily of ZrO_2 and MoO_3 oxides, but also hints of Ni, Ti, and W most likely due from the ball milling mediums used during powder milling. Figure 3.10E displays an interlayer between the oxide and unaffected layer, which is believed to be a part of the mechanism during MoO_3 oxidation. At temperatures between 800-1100 °C, a very thin coating of MoO_2 is formed, which then undergoes oxygen absorption via the reaction (3.7) [92, 100]:

$$O + MoO_2 \rightarrow MoO_3 \tag{3.7}$$

The suspected MoO_2 interlayer at 1000 °C helps to explain the TGA data presented in Figure 3.6B, where the oxidation weight loss due to MoO_3 volatilisation occurs during the ramp rate to a higher temperature but then reverts to paralinear kinetic during the dwell step. Furthermore, the temperature ramping portion of the TGA would have imparted severe changes in thermal gradient across the specimen, further destabilising the sample integrity. Therefore, it can be suggested that the stoichiometry of Mo oxide changes as the scales grow, thus changing the rate of the volatilisation process. A thicker outer layer of remaining ZrO_2 may have been enough to protect the inner MoO_2 layer, or at least slow down its oxidation rate. The final SEM image in Figure 3.10F, in conjunction with the XRD of Figure 3.8, shows only particles of ZrO_2 remaining on the surface as no Mo oxide is detected.

The SEM image in Figure 3.11A shows (dotted red line) a barely visible oxide layer in the composite ZrC-20TiC. Oxidation became more prevalent as the temperature reached 800 °C after 1 h, the oxide layer had already thickness extended by 200 μm composed of a ZrO_2 and TiO_2 rich layer, Figure 3.11B.

This is also the point where the first evidence of the $(Zr,Ti)O_2$ mixed oxide species is detected by XRD. At 1000 °C, both images in Figure 3.7B and Figure 3.11C show loss of adhesion between the oxide and matrix layers. It is unclear why this happens, yet the overall structure of ZrC-TiC shows better integrity than ZrC-Mo or ZrC at 1000-1200 °C. The mixed oxide species, $(Zr,Ti)O_2$, was determined to be tetragonal; hence a mismatch between the cubic (Zr,Ti)C matrix could explain why the layers adhere so loosely. Another reason maybe the mismatch in the coefficient of thermal expansion (CTE) between the oxidised scale and un-oxidised matrix together act as a bilayer structure. Assuming the average linear coefficient of thermal expansion of the oxide scale is greater than that of the carbide-based specimen, then the thermal mismatch stress upon cooldown would be tensile at the exterior surface and compressive within the carbide specimen [101]. The cracks would originate at the exterior surface and terminate at the oxide–carbide interlayer as seen in Figure 3.11C. The cracks at the surface shown in Figure 3.11D and between the bilayer in Figure 3.11E would allow further oxygen penetration into the matrix forcing oxidation. In fact, from Figure 3.7C 1200 °C, there is a clear indication of an oxidation gradient developing between the outer surface (yellow hue) into the depleted zone (lighter yellow hue) and into the matrix (grey). The final image of the oxidised ZrC-TiC surface, Figure 3.11F, shows two contrasting grains, white being undisguisable ZrO_2 and TiO_2, and larger, darker grains to be $(Zr,Ti)O_2$.

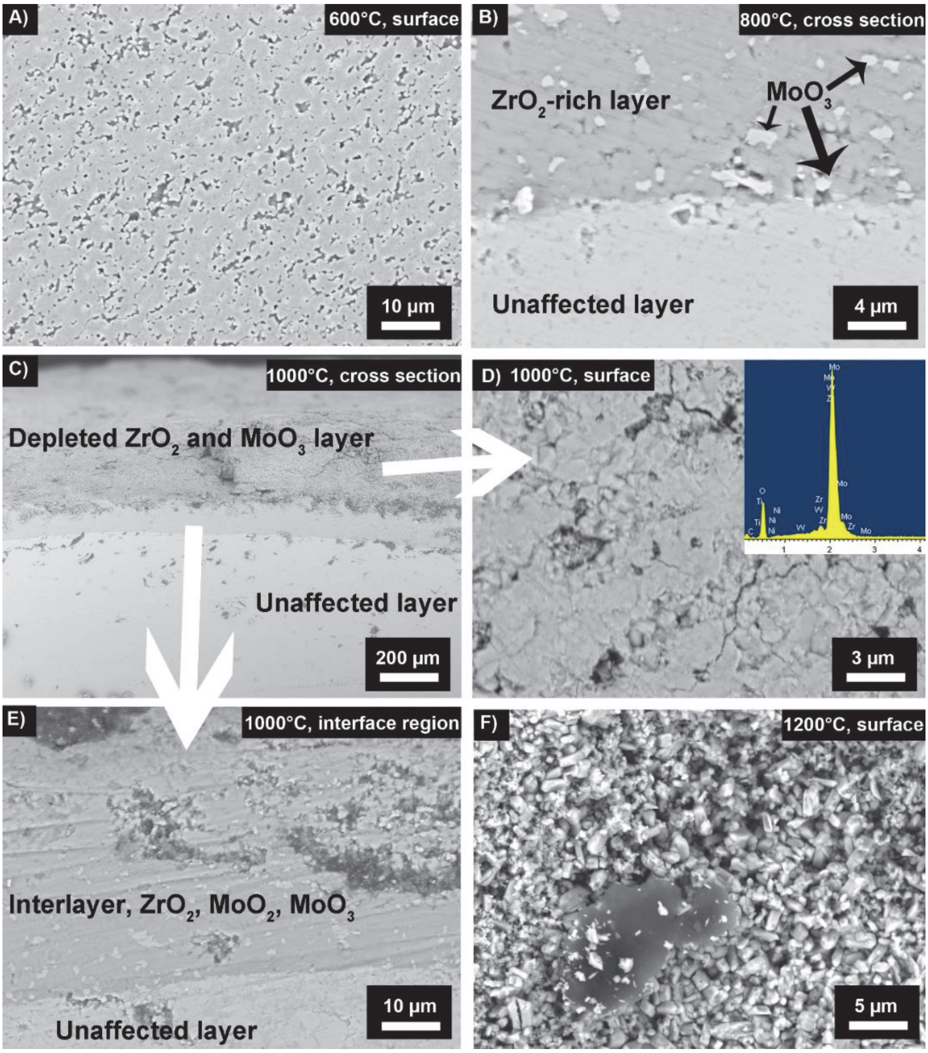

Figure 3.10 *SEM images, including EDS scan, of ZrC-20Mo after different oxidation temperatures in static air.*

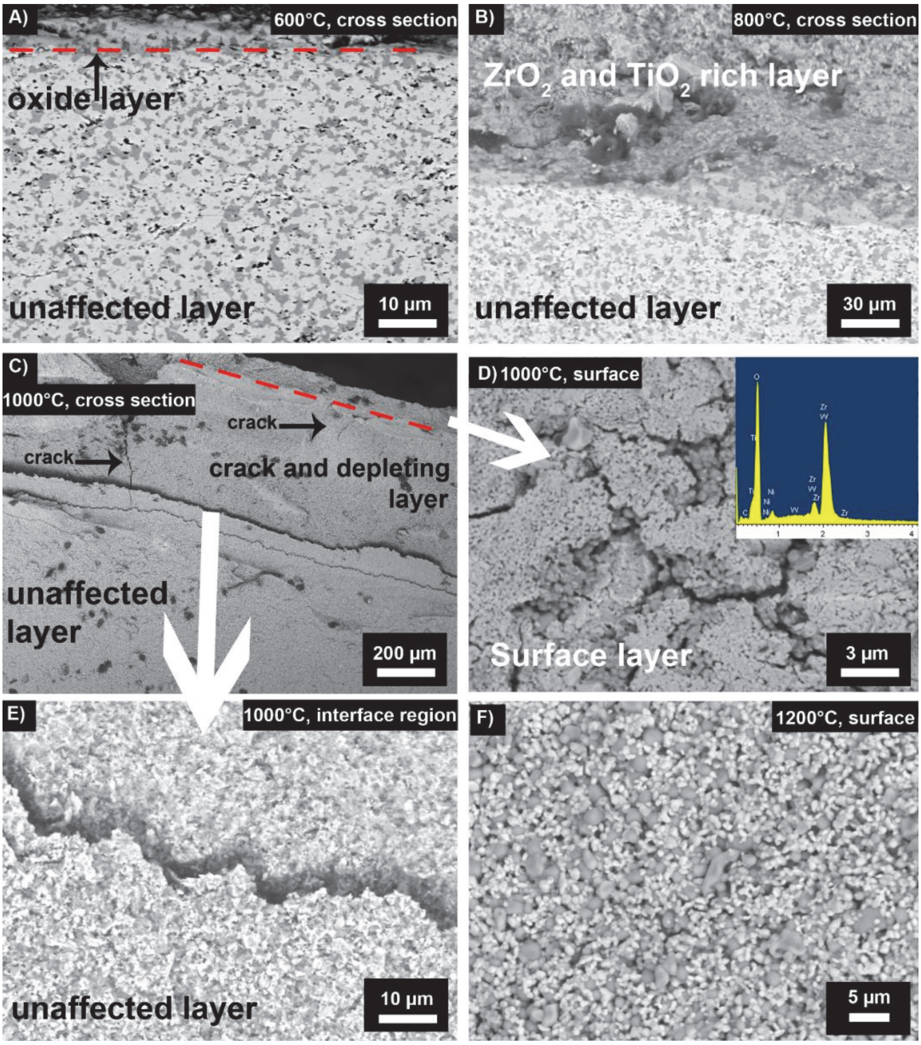

Figure 3.11 *SEM images, including EDS scan, of ZrC-20TiC at different oxidation temperatures in static air.*

3.9 Wear tests for ZrC and TiC doped hardmetals

Paper III details the study on the tribological behaviour of doping WC-8Ni with either ZrC or TiC. Three samples of WC-8Ni hardmetal were synthesised and their respective mechanical properties are shown in Table 3.7. WNO represents a control WC-8Ni sample, while WNT and WNZr contain TiC and ZrC additives respectively. ZrC is most effective being a grain growth inhibitor, in fact, the sample WNZr possess an average grain size half of that of the other two samples. The results of the slurry tests indicate similar negligible wear for all three sampless suggesting that the parameters of the tests were too mild to distinguish any difference in wear.

Table 3.7 *Mechanical properties of ZrC and TiC doped WC-Ni hardmetals*

Material grade	**WC grain size [µm]**	**Mean free path [µm]**	**Relative density [%]**	**Hardness, HV30**	**Indentation Fracture toughness, K_{IC} [MPa·m$^{1/2}$]**
WNO	0.88	0.17	97.4	1296 ± 8	13.5 ± 1.4
WNT	0.94	0.26	96.4	1343 ± 14	11.8 ± 1.2
WNZr	0.48	0.15	99.2	1618 ± 8	10.7 ± 1.4

*WNO = **WC-8Ni***
*WNT = **WC-8Ni-1TiC***
*WNZr = **WC-8Ni-1.3ZrC***

The dry erosion and ASTM G65 rubber wheel test with silica signals an increase in the aggressive wear of the samples compared to slurry erosion. In both the dry erosion and low-stress G65 tests, WNT exhibited differentiation compared to the other two samples as WNT had twice less wear loss, as shown in Figure 3.12. Since WNT has the largest mean free path (MFP), it suggests that fine dust abrasive particles could be in the binder, stalling continuous wear. Even with high hardness, the fine grain structure of WNZr, in conjunction with the relatively low binder content results in low wear resistance, since too much of the binder is exposed to the surface [102-104]. WNT performs well in the dry erosion test due to the enlarged and elongated WC grains. However, the trend for WNT reverses when subjected to the most aggressive test where compressive pressures are applied. The high stress abrasion test sees WNT with the highest wear rate. This result could be attributed to two likely causes: TiC is suggested to lower the WC cemented carbide's compressive strength, leading to lower fracture resistance [105]; or by having larger WC grains due to grain growth that wears the binder interlayers and leads to micro-chipping [102]. In the end, ZrC does little to provide any strengthening of the WC-Ni hardmetal despite evident grain refinement and increased hardness.

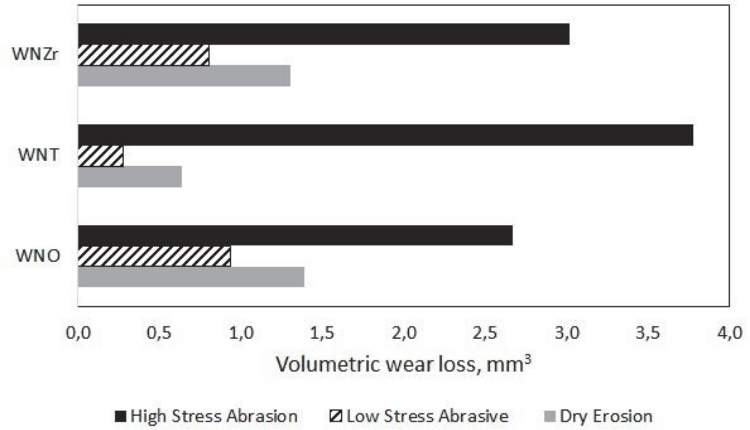

Figure 3.12 *High-stress represents the corner abrasion test against SiC sandpaper; low-stress represents the ASTM G65 rubber wheel test; and dry erosion represents wear caused by flying erodent particles.*
WNO *= WC-8Ni*
WNT *= WC-8Ni-1TiC*
WNZr *= WC-8Ni-1.3ZrC*

3.10 HT wear of PTA welded ZrC or TiC reinforced NiCrSiB hardfacing

The homogeneous distribution of ZrC or TiC particles in the MMC during PTA welding was optimised by the parameters given in Table 2.1. This was necessary due to the density difference between ZrC and TiC; the homogeneity of the carbide in the matrix is showcased in Figure 3.13.

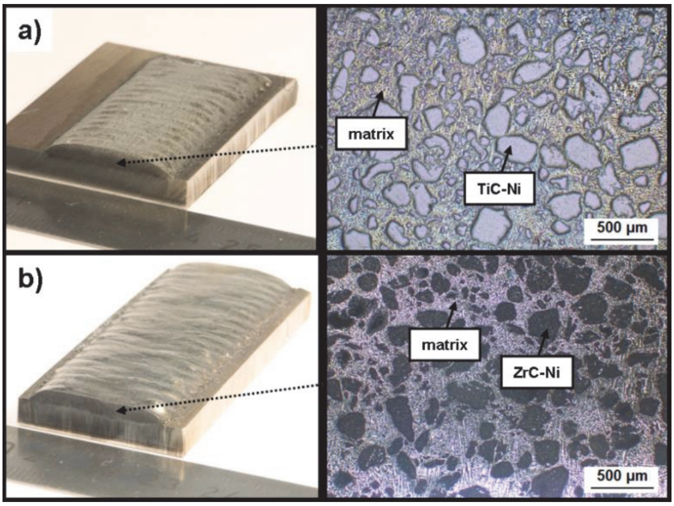

Figure 3.13 *Weld seam analysis and optimal microscopy image of a) TiC-Ni and b) ZrC-Ni reinforced hardfacing.*

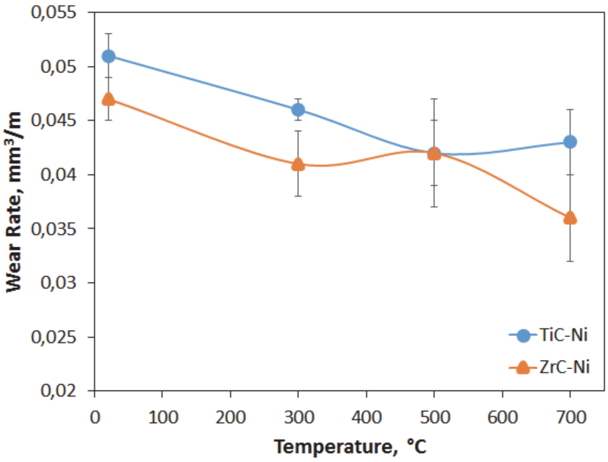

Figure 3.14 *High-temperature cyclic abrasion testing (modified ASTM G65 with heater) for TiC-Ni and ZrC-Ni reinforced hardfacings.*

It is clearly shown that ZrC consistently outperforms the TiC reinforced hardfacing in both impact and three-body abrasion testing. From RT, the ZrC-Ni hardfacing shows an almost 10 % lower wear rate than TiC-Ni and the trend is maintained up to 700 °C shown in Figure 3.14. One possible explanation is that TiC-Ni has larger MFP compared to ZrC-Ni, which under ASTM G65 conditions at RT could lead to more wear as the TiC particles are more readily pulled from the matrix by the abrasive flow. Both TiC-Ni and ZrC-Ni reinforced matrix increase wear resistance with increasing temperatures. This is due to either oxidation of the carbides where oxides provide protection by making the surface lubricious, akin to having a solid lubricant; the softening of silica at elevated temperatures, thus reducing cutting ability of the abrasive; or softening of the matrix allowing silica embedment, thickening the out-layer of the wearable surface.

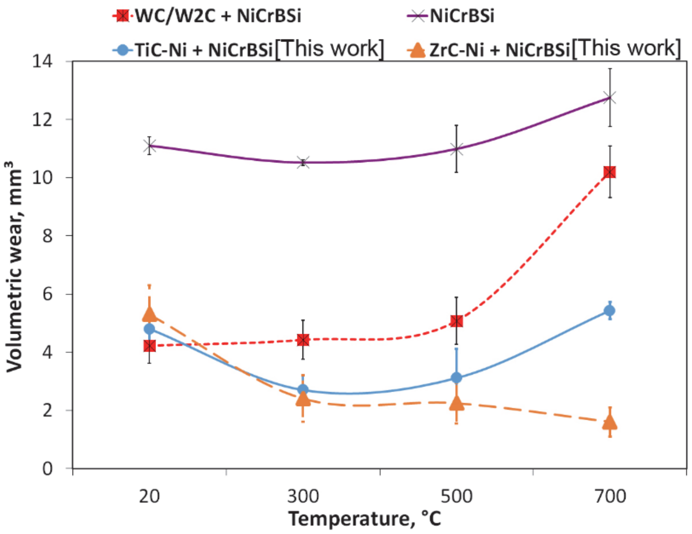

Figure 3.15 *High-temperature cyclic impact abrasion testing of TiC-Ni and ZrC-Ni reinforced hardfacings with added control samples reference NiCrBSi and WC/W$_2$C + NiCrBSi from other works.*

Cyclic impact abrasion at elevated temperatures up to 700 °C demonstrated TiC-Ni and ZrC-Ni reinforcements to have a higher wear resistance from 500 °C compared to WC reinforced or pure MMC, Figure 3.15. Therefore, it can be established that both ZrC-Ni and TiC-Ni reinforcements could be good alternatives to commercially used WC/W$_2$C reinforcements for the Ni-based matrix. Previously it was already proven that especially at elevated temperatures (exceeding 550°C), Cr_3C_2-Ni and TiC-NiMo reinforcements provide better tribological behaviour than tungsten carbide [25]. ZrC-Ni forms a complex solid-solution $(Zr,Cr)_{23}C_6$ with the matrix and $M_{23}CB_6$ in the dendritic γ-Ni matrix, detected in XRD scans, Figure 3.16, imbuing additional oxidation resistance to the matrix and reversing volumetric wear rate. TiC-Ni and ZrC-Ni are able to outperform the WC/W_2C reinforced hardfacing at higher testing temperatures, mainly due to the higher oxidation resistance of those carbides compared to tungsten carbide.

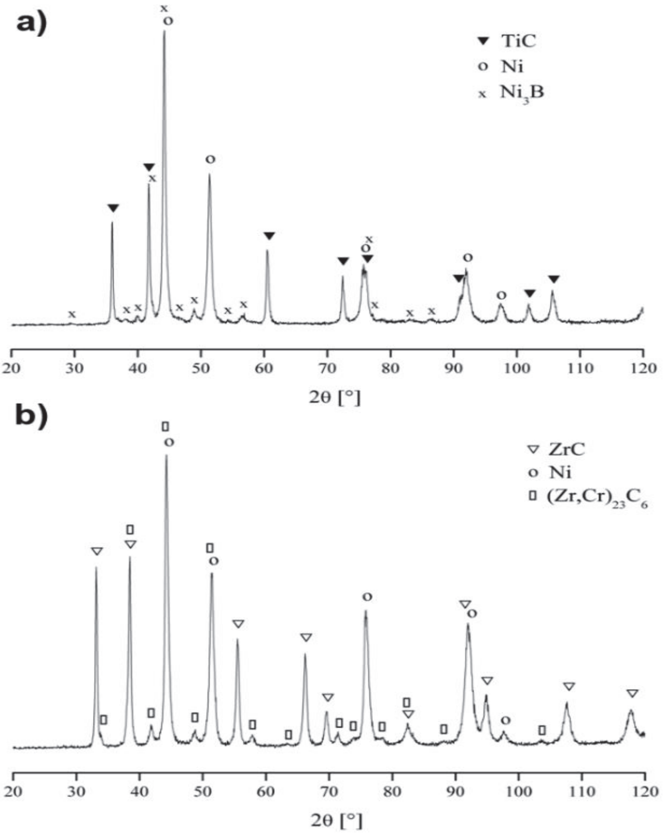

Figure 3.16 *XRD pattern of a) TiC-Ni and b) ZrC-Ni reinforced NiCrSiB hardfacing.*

At elevated temperatures, SEM images (Figure 3.17) clearly show the presence of oxide growth specifically concentrated at the matrix zone and not on the carbide hardfacings when tested at 700 °C. With the ZrC-Ni hardfacing, there is evidence of surface cracking at the cermet zone, Figure 3.17d. Both samples show presence of SiO_2 embedded into the matrix, Figure 3.17a and b. It is interesting to note that much of the TiO_2 then reacts with Ni to form a unique species in $NiTiO_3$ and then increases the wear rate for TiC-Ni at 700 °C. $NiTiO_3$

calcinates above 600 °C and is able to dissolve NiO [106]; this could further expedite the oxidation of the Ni in the cermet zone, leading to disintegration of the TiC-Ni reinforcement and increased wear rate at 700 °C.

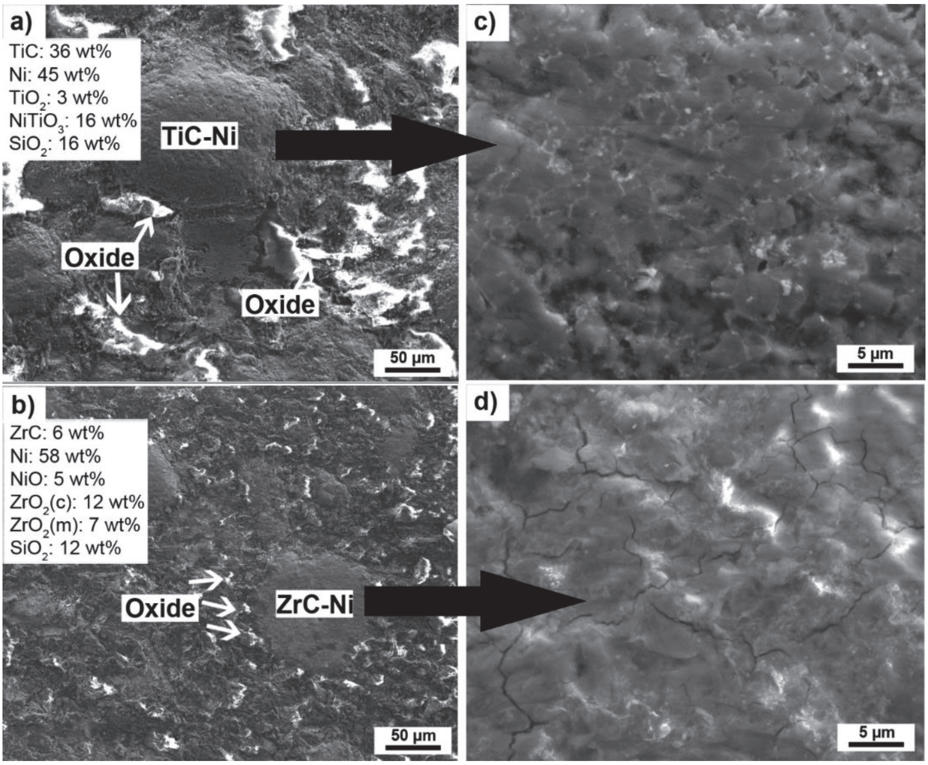

Figure 3.17 *Images of worn surface after HT-CIAT at 700 °C where a) & c) show TiC-Ni and b) & d) show ZrC-Ni reinforced hardfacings respectively. The quantitative XRD analysis is also included reflecting the composition of the surface layer.*

4. CONCLUSIONS

The present work is concentrated on ZrC and its usage as a main constituent in high-temperature composites or as an additive to WC cemented carbide or as a reinforcement particulate to hardfaced coating. The potential to be a suitable material for high-temperature and tribological applications is also investigated. The composites samples were subjected to oxidation testing at temperatures up to 1500 °C. ZrC doped WC cemented carbide was subjected to tribological studies at both low and high stress abrasion. Finally, ZrC reinforced particulates into PTA coatings were subjected to high-temperature cyclic and impact abrasion. From this study, the following conclusions can be drawn:

1. Optimised SPS parameters for composite synthesis are the following:
   a. For ZrC-20TiC, the pressure was 100 MPa and the sintering temperature 1600 °C [paper I].
   b. For ZrC-20Mo, the pressure was 50 MPa and the sintering temperature 2100 °C [paper II].
2. For composite materials, mechanical properties under optimum SPS sintering conditions produced:
   a. ZrC-20TiC at a fracture toughness of 5.4 MPa•m$^{1/2}$, a 25 % improvement over other sintering conditions [paper I].
   b. ZrC-20Mo fracture toughness steadily increased with increasing SPS temperature up to 5.4 MPa•m$^{1/2}$, and improvement over other sintering conditions [paper II].
3. SPS parameters resulted in the following phases being produced:
   a. For ZrC-20TiC, the sintering temperature was below the miscibility gap formation of (Zr,Ti)C, maintaining TiC in the microstructure to act as bridging and crack deflectors [paper I].
   b. For ZrC-20Mo, the microstructure exhibited smaller clusters of Mo solid solution, increasing the value of mechanical toughness [paper II].
4. HPHT SPS of ZrC-20Mo and ZrC-20TiC had minimal impact on the mechanical properties compared to conventional SPS [paper IV].

5. Composite oxidation up to 1500 °C in air:

    a. ZrC-20Mo oxidation caused significant weight loss beyond 800 °C, indicating MoO_3 volatilisation and pesting. This limits this material for future nuclear and space vehicle applications. Testing was done up to only 1200 °C.

    b. ZrC-20TiC showed steady oxidation and weight gain up to 1000 °C, and vigorously resisted oxidation penetration into the microstructure. At 1500 °C, mixed oxide species $(Zr,Ti)O_2$ was detected.

6. ZrC or TiC doped into WC-8wt%Ni, the following wear behaviour was observed [paper III]:

    a. TiC addition increases the MFP in WC-8Ni to resist fine abrasive and low-stresses. TiC additive could be an option to enhance tools wear resistance for soft ground TBM.

    b. TiC decreases the cemented carbide's ability to resist high-stress abrasion.

    c. ZrC refines WC grains and increases hardness, but does not improve wear resistance when compared to the control.

7. PTA welding was optimised to using lower welding current for ZrC-Ni and TiC-Ni reinforced MMC to ensure homogenous and viable coatings.

8. ZrC-Ni or TiC-Ni reinforced MMC hardfaced coating via PTA welding gave the following results:

    a. ZrC-Ni outperforms TiC-Ni reinforcement under oxidation abrasion conditions up to 700 °C.

    b. ZrC-Ni forms a complex solid-solution $(Zr,Cr)_{23}C_6$ with the NiCrBSi matrix.

    c. Under hot ASTM G65 abrasion testing, the larger MFP of TiC-Ni particles made carbide washout more readily resulting in higher wear rate.

The scientific novelty

This thesis centres on ZrC, it highlights this carbide in three different applications: as a composite base material, as a dopant, and as a reinforcement particulate. Although ZrC-Mo and ZrC-TiC composites were previously studied, this is the first time the respective composites have been synthesised with SPS and HPHT to investigate the influence of compaction pressure on material properties. In the current research, ZrC-20TiC showed that a higher than conventional compaction pressure during SPS and sintering below the temperature of the compositions miscibility gap can improve the fracture toughness by 25 %.

For both composites, the experiments with high-temperature oxidation are all novel investigations for this composition with temperatures up to 1500 °C to determine whether they are viable for application in the future nuclear and space vehicle applications where operating temperatures could reach 1000 °C. Although ZrC-20Mo falters at 800 °C, ZrC-20TiC shows promise by outperforming both pure ZrC and ZrC-20Mo up to 1000 °C.

Wear mechanism of ZrC-doped WC-8Ni hardmetal were studied in different tribological conditions to characterise the wear mechanics under wet, dry, low, high stress conditions. The results add another layer of knowledge to the effect of carbide additives to existing hardmetal materials meant for industrial tools.

Finally, using ZrC reinforcement into the MMCs applied a PTA coating was performed for the first time and shows an improvement in the high-temperature abrasive wear over TiC and commercial WC reinforcement.

For future work, the potential to use ZrC as a base phase may be optimised in different compositions for industrial applications. The PTA coating using reinforced ZrC particles are shown to outperform WC reinforcements. There only needs to be the commitment.

5. REFERENCE

[1] Pierson HO. *Handbook of Refractory Carbides and Nitrides* Westwood, NJ: William Andres Publishing/Noyes; (1996).
[2] Sommers A, Wang Q, Han X, T'Joen C, Park Y, Jacobi A. Ceramics and ceramic matrix composites for heat exchangers in advanced thermal systems—A review. *Applied Thermal Engineering*. (2010) 30, 1277-91.
[3] Pan Y, Li DY, Zhang H. Enhancing the wear resistance of sintered WC–Co composite by adding pseudo-elastic TiNi constituent. *Wear*. (2011) 271, 1916-21.
[4] Weidow J, Andrén H-O. Grain and phase boundary segregation in WC–Co with TiC, ZrC, NbC or TaC additions. *International Journal of Refractory Metals and Hard Materials*. (2011) 29, 38-43.
[5] Poetschke J, Richter V, Holke R. Influence and effectivity of VC and Cr3C2 grain growth inhibitors on sintering of binderless tungsten carbide. *International Journal of Refractory Metals and Hard Materials*. (2012) 31, 218-23.
[6] Zikin A, Ilo S, Kulu P, Hussainova I, Katsich C, Badisch E. Plasma Transferred ARC (PTA) Hardfacing of Recycled Hardmetal Reinforced Nickel-matrix Surface Composites. *Materials Science*. (2012) 18, 12-7.
[7] Azevedo CRF. Selection of fuel cladding material for nuclear fission reactors. *Engineering Failure Analysis*. (2011) 18, 1943-62.
[8] Landwehr SE, Hilmas GE, Fahrenholtz WG, Talmy IG, Wang H. Thermal properties and thermal shock resistance of liquid phase sintered ZrC–Mo cermets. *Materials Chemistry and Physics*. (2009) 115, 690-5.
[9] Zhang X, Liu N. Effects of ZrC on microstructure, mechanical properties and thermal shock resistance of TiC–ZrC–Co–Ni cermets. *Materials Science and Engineering: A*. (2013) 561, 270-6.
[10] NASA. *Orbiter Thermal Protection System*. NASAfacts. www.nasa.gov: National Aeronautics and Space Adminstration; (2006). p. 1-8. (accessed July 23, 2016).
[11] Starflinger J, Schulenberg T, Marsault P, Bitterman D, Maraczy C, Laurien E, et al. *GIF R&D Outlook for Generation IV Nuclear Energy Systems*. Gen IV International Forum(2009). p. 32.
[12] Shimada S. TEM Observation of the ZrC/ZrO2 Interface Formed by Oxidation of ZrC Single Crystals. *Journal of Materials Synthesis and Processing*. (1998) 6, 191-5.
[13] Association WN, "World Energy Needs and Nuclear Power," http://www.world-nuclear.org/information-library/current-and-future-generation/world-energy-needs-and-nuclear-power.aspx (accessed July 23, 2016).
[14] Association WN, "Generation IV Nuclear Reactors," http://www.world-nuclear.org/information-library/nuclear-fuel-cycle/nuclear-power-reactors/generation-iv-nuclear-reactors.aspx (accessed July 23, 2016).
[15] Jayaraj J, Krishnaveni P, Krishna DNG, Mallika C, Mudali UK. Corrosion investigations on zircaloy-4 and titanium dissolver materials for MOX fuel dissolution in concentrated nitric acid containing fluoride ions. *Journal of Nuclear Materials*. (2016) 473, 157-66.
[16] Whitmarsh CL. *Review of Zircaloy-2 and Zircaloy-4*. 17th ed. Oak Ridge National Laboratory: U.S. Atomic Energy Commission; (1962).
[17] Katoh Y, Vasudevamurthy G, Nozawa T, Snead LL. Properties of zirconium carbide for nuclear fuel applications. *Journal of Nuclear Materials*. (2013) 441, 718-42.

[18] Monti R, Pezzella G. *Design Criteria for Low Risk Re-entry Vehicles*. Proceedings of the fifth European Symposium on Aerothermodynamics for Space Vehicles. Cologne, Germany: European Space Agency; (2005). p. 563-71.

[19] Savino R, De Stefano Fumo M, Paterna D, Serpico M. Aerothermodynamic study of UHTC-based thermal protection systems. *Aerospace Science and Technology*. (2005) 9, 151-60.

[20] Detournay E, Richard T, Shepherd M. Drilling response of drag bits: Theory and experiment. *International Journal of Rock Mechanics and Mining Sciences*. (2008) 45, 1347-60.

[21] Ren X, Miao H, Peng Z. A review of cemented carbides for rock drilling: An old but still tough challenge in geo-engineering. *International Journal of Refractory Metals and Hard Materials*. (2013) 39, 61-77.

[22] Jakobsen P, Lohne J. Challenges of methods and approaches for estimating soil abrasivity in soft ground TBM tunnelling. *Wear*. (2013) 308, 166-73.

[23] Nurminen J, Näkki J, Vuoristo P. Microstructure and properties of hard and wear resistant MMC coatings deposited by laser cladding. *International Journal of Refractory Metals and Hard Materials*. (2009) 27, 472-8.

[24] Zhang X, Ma J, Fu L, Zhu S, Li F, Yang J, et al. High temperature wear resistance of Fe–28Al–5Cr alloy and its composites reinforced by TiC. *Tribology International*. (2013) 61, 48-55.

[25] Zikin A, Antonov M, Hussainova I, Katona L, Gavrilović A. High temperature wear of cermet particle reinforced NiCrBSi hardfacings. *Tribology International*. (2013) 68, 45-55.

[26] Zikin A, Badisch E, Hussainova I, Tomastik C, Danninger H. Characterisation of TiC–NiMo reinforced Ni-based hardfacing. *Surface and Coatings Technology*. (2013) 236, 36-44.

[27] Zikin A, Hussainova I, Katsich C, Badisch E, Tomastik C. Advanced chromium carbide-based hardfacings. *Surface and Coatings Technology*. (2012) 206, 4270-8.

[28] Kuzmanovic J, Danninger H, Gierl C, Zbiral J, Halwax E, Zikin A. Preparation and Properties of Sintered Fe and Ni based MMCs reinforced with fused Tungsten Carbide particles. *Powder Metallurgy Progress*. (2012) 12, 84-98.

[29] Zhang Q, He J, Lui W, Zhong W. Microstructure characteristics of ZrC-reinforced composite coating produced by laser cladding . *Surface and Coatings Technology*. (2003) 162, 140-6.

[30] Barbatti C, Garcia J, Brito P, Pyzalla AR. Influence of WC replacement by TiC and (Ta,Nb)C on the oxidation resistance of Co-based cemented carbides. *International Journal of Refractory Metals and Hard Materials*. (2009) 27, 768-76.

[31] Pellegrino S, Thomé L, Debelle A, Miro S, Trocellier P. Radiation effects in carbides: TiC and ZrC versus SiC. *Nuclear Instruments and Methods in Physics Research Section B: Beam Interactions with Materials and Atoms*. (2014) 327, 103-7.

[32] Song GM, Wang YJ, Zhou Y. Elevated temperature ablation resistance and thermophysical properties of tungsten matrix composites reinforced with ZrC particles. *Journal of Material Science*. (2001) 36, 4625-31.

[33] Barnier P, Brodhag C, Thevenot F. Hot-pressing kinetics of zirconium carbide. *Journal of Material Science*. (1986) 21, 2547-52.

[34] Shimada S, Inagaki M. Microstructural observation of the ZrCyZrO2 interface formed by oxidation of ZrC. *Journal of Materials Research*. (1996) 11, 2594-7.

[35] Yung DL, Kollo L, Hussainova I, Žikin A. *Reactive Sintering of Zirconium Carbide-based composites*. 8th International DAAAM Baltic Conference. Tallinn, Estonia: Industrial Engineering; (2012). p. 1-6.

[36] Chu A, Qin M, Rafi ud d, Zhang L, Lu H, Jia B, et al. Carbothermal synthesis of ZrC powders using a combustion synthesis precursor. *International Journal of Refractory Metals and Hard Materials*. (2013) 36, 204-10.
[37] Leconte Y, Maskrot H, Combemale L, Herlin-Boime N, Reynaud C. Application of the laser pyrolysis to the synthesis of SiC, TiC and ZrC pre-ceramics nanopowders. *Journal of Analytical and Applied Pyrolysis*. (2007) 79, 465-70.
[38] Combemale L, Leconte Y, Portier X, Herlin-Boime N, Reynaud C. Synthesis of nanosized zirconium carbide by laser pyrolysis route. *Journal of Alloys and Compounds*. (2009) 483, 468-72.
[39] Dollé M, Gosset D, Bogicevic C, Karolak F, Simeone D, Baldinozzi G. Synthesis of nanosized zirconium carbide by a sol–gel route. *Journal of the European Ceramic Society*. (2007) 27, 2061-7.
[40] Mahday A, El-Eskandarany M, Ahmed HA, Amer AA. Mechanically induced solid state carburization for fabrication of nanocrystalline ZrC refractory material powders. *Journal of Alloys and Compounds*. (2000) 299, 244-53.
[41] Tsuchida T, Yamamoto S. Mechanical activation assisted self-propagating high-temperature synthesis of ZrC and ZrB2 in air from Zr/B/C powder mixtures. *Journal of the European Ceramic Society*. (2004) 24, 45-51.
[42] Bocanegra-Bernal MH. Hot Isostatic Pressing (HIP) technology and its applications to metals and ceramics. *Journal of Material Science*. (2004) 39, 6399-420.
[43] Zhao L, Jia D, Duan X, Yang Z, Zhou Y. Pressureless sintering of ZrC-based ceramics by enhancing powder sinterability. *International Journal of Refractory Metals and Hard Materials*. (2011) 29, 516-21.
[44] Teber A, Schoenstein F, Têtard F, Abdellaoui M, Jouini N. The effect of Ti substitution by Zr on the microstructure and mechanical properties of the cermet Ti1-xZrxC sintered by SPS. *International Journal of Refractory Metals and Hard Materials*. (2012) 31, 132-7.
[45] Tan YQ, Chen C, Li FZ, Zhang HB, Zhang GJ, Peng SM. Enhancement of sinterability and mechanical properties of B4C ceramics using Ti3AlC2as a sintering aid. *RSC Adv*. (2015) 5, 76309-14.
[46] Guillon O, Gonzalez-Julian J, Dargatz B, Kessel T, Schierning G, Räthel J, et al. Field-Assisted Sintering Technology/Spark Plasma Sintering: Mechanisms, Materials, and Technology Developments. *Advanced Engineering Materials*. (2014) 16, 830-49.
[47] Orrù R, Licheri R, Locci AM, Cincotti A, Cao G. Consolidation/synthesis of materials by electric current activated/assisted sintering. *Materials Science and Engineering: R: Reports*. (2009) 63, 127-287.
[48] Vanmeensel K, Laptev A, Hennicke J, Vleugels J, Vanderbiest O. Modelling of the temperature distribution during field assisted sintering. *Acta Materialia*. (2005) 53, 4379-88.
[49] Chen W, Anselmi-Tamburini U, Garay JE, Groza JR, Munir ZA. Fundamental investigations on the spark plasma sintering/synthesis process. *Materials Science and Engineering: A*. (2005) 394, 132-8.
[50] Wang S, He D, Zou Y, Wei J, Lei L, Li Y, et al. High-pressure and high-temperature sintering of nanostructured bulk NiAl materials. *Journal of Materials Research*. (2011) 24, 2089-96.
[51] Berg S, Häggblad H-Å, Jonsén P. High-pressure compaction modelling of calcite (CaCO3) powder compact. *Powder Technology*. (2011) 206, 259-68.
[52] Berg S, Jonsén P, Häggblad H-Å. Experimental characterisation of CaCO3 powder mix for high-pressure compaction modelling. *Powder Technology*. (2010) 203, 198-205.

[53] Sachse W, Ruoff AL. Elastic moduli of precompressed pyrophyllite used in ultrahigh-pressure research. *Journal of Applied Physics*. (1975) 46, 3725.
[54] Kim J-H, Seo M, Kang S. Effect of carbide particle size on the properties of W–ZrC composites. *International Journal of Refractory Metals and Hard Materials*. (2012) 35, 49-54.
[55] Sun S-K, Zhang G-J, Wu W-W, Liu J-X, Suzuki T, Sakka Y. Reactive spark plasma sintering of ZrC and HfC ceramics with fine microstructures. *Scripta Materialia*. (2013) 69, 139-42.
[56] Pierrat B, Balat-Pichelin M, Silvestroni L, Sciti D. High temperature oxidation of ZrC–20%MoSi2 in air for future solar receivers. *Solar Energy Materials and Solar Cells*. (2011) 95, 2228-37.
[57] Hussainova I, Voltšihhin N, Cura E, Hannula S-P. Densification and characterization of spark plasma sintered ZrC–ZrO2 composites. *Materials Science and Engineering: A*. (2014) 597, 75-81.
[58] Yung D, Voltsihhin N, Hussainova I, Kollo L, Traksmaa R. *Sintering of Zirconium carbide-based composites*. In: Useldinger DR, editor. Euro PM2012. Basal, Switzerland: EUROPM; (2012). p. 1-6.
[59] Yung DL, Kollo L, Hussainova I, Žikin A. Reactive Sintering of ZrC-TiC Composites. *Key Engineering Materials*. (2012) 527, 20-5.
[60] Nomura N, Suzuki T, Nakatani S, Yoshimi K, Hanada S. Joining of oxidation-resistant Mo-Si-B multiphase alloy to heat-resistant Mo-ZrC in-situ composite. *Intermetallic*. (2003) 11, 51-6.
[61] Suzuki T, Matsumoto H, Nomura N, Hanada S. Microstructures and fracture toughness of directionally solidified Mo-ZrC eutectic composites. *Science and Technology of Advanced Materials*. (2002) 3, 137-43.
[62] Landwehr SE, Hilmas GE, Fahrenholtz WG, Talmy IG. Processing of ZrC-Mo Cermets for High-Temperature Applications, Part I: Chemical Interactions in the ZrC-Mo System. *Journal of the American Ceramic Society*. (2007) 90, 1998-2002.
[63] Landwehr SE, Hilmas GE, Fahrenholtz WG, Talmy IG. Processing of ZrC–Mo Cermets for High Temperature Applications, Part II: Pressureless Sintering and Mechanical Properties. *Journal of the American Ceramic Society*. (2008) 91, 873-8.
[64] Landwehr SE, Hilmas GE, Fahrenholtz WG, Talmy IG, DiPietro SG. Microstructure and mechanical characterization of ZrC–Mo cermets produced by hot isostatic pressing. *Materials Science and Engineering: A*. (2008) 497, 79-86.
[65] Takida T, Mabuchi M, Nakamura M, Igarashi T, Doi Y, Nagae T. Mechanical properties of a ZrC-dispersed Mo alloy processed by mechanical alloying and spark plasma sintering. *Materials Science and Engineering: A*. (2000) 276, 269-72.
[66] Ohser-Wiedemann R, Martin U, Seifert HJ, Müller A. Densification behaviour of pure molybdenum powder by spark plasma sintering. *International Journal of Refractory Metals and Hard Materials*. (2010) 28, 550-7.
[67] Liu S, Hu W, Xiang J, Wen F, Xu B, Yu D, et al. Mechanical properties of nanocrystalline TiC–ZrC solid solutions fabricated by spark plasma sintering. *Ceramics International*. (2014) 40, 10517-22.
[68] Adjaoud O, Steinle-Neumann G, Burton BP, van de Walle A. First-principles phase diagram calculations for the HfC–TiC, ZrC–TiC, and HfC–ZrC solid solutions. *Physical Review B*. (2009) 80, 134112.
[69] Li Y, Katsui H, Goto T. Spark plasma sintering of TiC–ZrC composites. *Ceramics International*. (2015) 41, 7103-8.

[70] Markström A, Frisk K. Experimental and thermodynamic evaluation of the miscibility gaps in MC carbides for the C–Co–Ti–V–W–Zr system. *Calphad*. (2009) 33, 530-8.

[71] Borgh I, Hedström P, Blomqvist A, Ågren J, Odqvist J. Synthesis and phase separation of (Ti,Zr)C. *Acta Materialia*. (2014) 66, 209-18.

[72] Ma T, Hedström P, Ström V, Masood A, Borgh I, Blomqvist A, et al. Self-organizing nanostructured lamellar (Ti,Zr)C — A superhard mixed carbide. *International Journal of Refractory Metals and Hard Materials*. (2015) 51, 25-8.

[73] Bonny K, De Baets P, Vleugels J, Huang S, Van der Biest O, Lauwers B. Impact of Cr3C2/VC addition on the dry sliding friction and wear response of WC–Co cemented carbides. *Wear*. (2009) 267, 1642-52.

[74] Espinosa L, Bonache V, Salvador MD. Friction and wear behaviour of WC–Co–Cr3C2–VC cemented carbides obtained from nanocrystalline mixtures. *Wear*. (2011) 272, 62-8.

[75] Shatov AV, Ponomarev SS, Firstov SA. Modeling the effect of flatter shape of WC crystals on the hardness of WC-Ni cemented carbides. *International Journal of Refractory Metals and Hard Materials*. (2009) 27, 198-212.

[76] Verfondern K, Nabielek H, Kendall JM. Coated particle fuel for high temperature gas cooled reactors. *Nuclear Engineering and Technology*. (2007) 39.

[77] Pizon D, Charpentier L, Lucas R, Foucaud S, Maître A, Balat-Pichelin M. Oxidation behavior of spark plasma sintered ZrC–SiC composites obtained from the polymer-derived ceramics route. *Ceramics International*. (2014) 40, 5025-31.

[78] Voitovich RF, Pugach EA. High Temperature Oxidation of ZrC AND HfC. *Poroshkovaya Metallurigiya*. (1973) 11, 67-74.

[79] Hou X-M, Chou K-C. Investigation of the effects of temperature and oxygen partial pressure on oxidation of zirconium carbide using different kinetics models. *Journal of Alloys and Compounds*. (2011) 509, 2395-400.

[80] Kuriakose AK, Margrave JL. The Oxidation Kinetics of Zirconium Diboride and Zirconium Carbide at High Temperatures. *Journal of The Electrochemical Society*. (1964) 111, 827.

[81] Zhao L, Jia D, Duan X, Yang Z, Zhou Y. Oxidation of ZrC–30vol% SiC composite in air from low to ultrahigh temperature. *Journal of the European Ceramic Society*. (2012) 32, 947-54.

[82] Ma B, Han W, Guo E. Oxidation behavior of ZrC-based composites in static laboratory air up to 1300°C. *International Journal of Refractory Metals and Hard Materials*. (2014) 46, 159-67.

[83] Tian C, Gao D, Zhang Y, Xu C, Song Y, Shi X. Oxidation behaviour of zirconium diboride–silicon carbide ceramic composites under low oxygen partial pressure. *Corrosion Science*. (2011) 53, 3742-6.

[84] Sergejev F, Antonov M. Comparative study on indentation fracture toughness measurements of cemented carbides. *Proceedings of Estonian Academia*. (2006) 12, 388-98.

[85] Oliver W, Pharr G. An improved technique for determining hardness and elastic modulus using load and displacement sensing indentation experiments. *Journal of Material Research*. (1992) 7, 1564-83.

[86] Umalas M, Hussainova I, Reedo V, Young D-L, Cura E, Hannula S-P, et al. Combined sol–gel and carbothermal synthesis of ZrC–TiC powders for composites. *Materials Chemistry and Physics*. (2015) 153, 301-6.

[87] Garg P, Park S-J, German RM. Effect of die compaction pressure on densification behavior of molybdenum powders. *International Journal of Refractory Metals and Hard Materials*. (2007) 25, 16-24.
[88] Anselmi-Tamburini U, Garay JE, Munir ZA. Fast low-temperature consolidation of bulk nanometric ceramic materials. *Scripta Materialia*. (2006) 54, 823-8.
[89] Tan Y, Ma CL, Kasama A, Tanaka R, Yang J-M. High temperature mechanical behavior of Nb–Mo–ZrC alloys. *Materials Science and Engineering: A*. (2003) 355, 260-6.
[90] Zhang J, Mei G, Zhao S, Meng H, Xie Z. A fused glass coating for oxidation protection of Mo–W–ZrO2 cermet. *Surface and Coatings Technology*. (2015) 261, 189-94.
[91] Lavrenko VA, Glebov LA, Pomitkin AP, Chuprina VG, Protsenko TG. High-Temperature Oxidation of Titanium Carbide in Oxygen. *Oxidation of Metals*. (1975) 9, 171-9.
[92] Smolik GR, Petti DA, Schuetz ST. Oxidation and volatilization of TZM alloy in air. *Journal of Nuclear Materials*. (2000) 283, 1458-62.
[93] Yanagihara K, Przybylski K, Maruyama T. The Role of Microstructure on Pesting During Oxidation of MoSi2 and Mo(Si,AI)2 at 773 K. *Oxidation of Metals*. (1997) 47, 277-93.
[94] Razumovskiy VI, Ruban AV, Odqvist J, Dilner D, Korzhavyi PA. Effect of carbon vacancies on thermodynamic properties of TiC–ZrC mixed carbides. *Calphad*. (2014) 46, 87-91.
[95] Silvestroni L, Sciti D, Balat-Pichelin M, Charpentier L. Zirconium carbide doped with tantalum silicide: Microstructure, mechanical properties and high temperature oxidation. *Materials Chemistry and Physics*. (2013) 143, 407-15.
[96] Troitzsch U, Christy AG, Ellis DJ. The crystal structure of disordered (Zr,Ti)O2 solid solution including srilankite: evolution towards tetragonal ZrO2 with increasing Zr. *Physics and Chemistry of Minerals*. (2005) 32, 504-14.
[97] Gherrab M, Garnier V, Gavarini S, Millard-Pinard N, Cardinal S. Oxidation behavior of nano-scaled and micron-scaled TiC powders under air. *International Journal of Refractory Metals and Hard Materials*. (2013) 41, 590-6.
[98] Thamaphat K, Limsuwan P, Ngotawornchai B. Phase Characterization of TiO2 Powder by XRD and TEM. *Journal of Nature Science*. (2008) 42, 357-61.
[99] Calatayud JM, Pardo P, Alarcón J. V-containing ZrO2 inorganic yellow nano-pigments. *Journal of the Royal Society of Chemistry*. (2015) 5, 58669-78.
[100] Olander DR, Schofill JL. Investigation of the convective-diffusion limited oxidation of molybdenum by the rotating disk method. *Metallurgical Transactions*. (1970) 1, 2775.
[101] Lipke DW, Ushakov SV, Navrotsky A, Hoffman WP. Ultra-high temperature oxidation of a hafnium carbide-based solid solution ceramic composite. *Corrosion Science*. (2014) 80, 402-7.
[102] Konyashin I, Ries B. Wear damage of cemented carbides with different combinations of WC mean grain size and Co content. Part II: Laboratory performance tests on rock cutting and drilling. *International Journal of Refractory Metals and Hard Materials*. (2014) 45, 230-7.
[103] Konyashin I, Ries B. Wear damage of cemented carbides with different combinations of WC mean grain size and Co content. Part I: ASTM wear tests. *International Journal of Refractory Metals and Hard Materials*. (2014) 46, 12-9.

[104] Konyashin I, Ries B, Lachmann F. Near-nano WC–Co hardmetals: Will they substitute conventional coarse-grained mining grades? *International Journal of Refractory Metals and Hard Materials*. (2010) 28, 489-97.
[105] van der Merwe R, Sacks N. Effect of TaC and TiC on the friction and dry sliding wear of WC–6wt.% Co cemented carbides against steel counterfaces. *International Journal of Refractory Metals and Hard Materials*. (2013) 41, 94-102.
[106] Tietz F, Dias FJ, Dubiel B, Penkalla HJ. Manufacturing of NiO/NiTiO3 porous substrates and the role of zirconia impurities during sintering. *Materials Science and Engineering*. (1999) B68, 35-41.

ACKNOWLEDGEMENTS

I wish to thank the many people who helped me during my PhD research. My family back in Vancouver, Canada, especially my parents who deeply miss their son for so many years as I travelled to far off corners of the world.

My deepest appreciation has to go to my immediate supervisors Dr. Irina Hussainova and Dr. Maksim Antonov, whose guidance, perseverance, and patience made this research work worthy. Their steady hands, good humour, and words of encouragement allowed me to finish what I started four years ago to become a doctor of philosophy of engineering. I am also very grateful to Dr. Miguel A. Rodriguez of the Instituto de Ceramica y Vidrio for the ideas and counsel to perform high-pressure SPS.

The technical help from people like Birgit Maaten (TUT), Lauri Kollo (TUT), Hans Vallner (TUT), Rainer Traksmaa (TUT), Mart Viljus (TUT), Slawomir Cygan (IOSP), Jolanta Cyboron (IOSP) deserve recognition for helping me to synthesise and analyse results. In fact, a portion of the thesis research was made during critical cooperation with the Institute of Advanced Manufacturing Technology in Krakow, Poland.

I would also like to thank Austrian Center of Competence of Tribology (AC2T) Research GmbH for providing me with internship opportunity in 2012 where I made experiments with fellow colleague Arkadi Zikin, and cooperated to published a joint paper.

Special thanks go to the friends I have made over the four year: Marek Tarraste, Marek Jõeleht, Kaspar Kallip, Maria Drozdova, Zorjana Mural, and many others. You brought inspiration into my life and made me a better man.

The bulk of my thesis work and funding is acknowledged to the support from the European Commission project NeTTUN, from the Seventh Framework Programme for Research, Technological Development and Demonstration (FP72007-2013) under Grant Agreement 280712. This work was also partially supported by institutional research funding IUT 19-29 of the Estonian Ministry of Education and Research. Archimedes targeted grant AR12133 (NanoCom) is also gratefully appreciated for supporting this study. The financial support of the European Social Fund's Doctoral Studies and Internationalization Programme DoRa, which is carried out by Foundation Archimedes, as well as PUT1063 (I. Hussainova) and B56 (M. Antonov), are highly appreciated.

ABSTRACT

ZrC-based and ZrC-doped Composites for High-Temperature and Wear Applications

Advancing technology will always warrant development into new and better materials capable of withstanding rigorous applications and oxidative environments. The nuclear field utilises composite claddings to encase radioactive materials, while operating at high temperatures up to 1000 °C under oxidation conditions. Similarly, spacecraft require heat shields during atmospheric re-entry under conditions up to 1200 °C, also under oxidation. Zirconium carbide (ZrC) is one of such materials that is resistant to irradiation damage, and has a high-temperature melting point. However, ZrC is also plagued by low fracture toughness and propensity to oxidation damage. The focus of this research thesis can be divided in three streams: 1) ZrC composites synthesised by SPS technology; 2) using as ZrC additives in hardmetals; and 3) ZrC reinforcement particulate carbide in PTA applied coatings. In the first part, the research analyses ZrC-based composites as an improvement to pure ZrC in terms of toughness and oxidation resistance. In the latter two parts, the research examines ZrC as an additive: a dopant to WC cemented carbide to improve wear resistance; and separately, as a reinforcement particulate to Ni alloy for high-temperature wear abrasion.

The first part is an investigation focused on two ZrC composites: ZrC-20Mo and ZrC-20TiC. Spark plasma sintering (SPS) and the use of high compaction pressures during sintering offer a faster approach to fully consolidated powder composite. Sintering ZrC-20Mo is a temperature dependent process, relative to the amount of Mo in the composite. The highest indentation fracture toughness for ZrC-20Mo was observed for the sample SPSed at 2100 °C, irrespective of pressure. Conversely, ZrC-20TiC yielded improved mechanical indentation fracture toughness with higher compaction pressures (100 MPa) at the same sintering temperature. By inhibiting the miscibility gap due to lowered SPS temperature, TiC can exist as a crack deflector component improving toughness. The effect of HPHT SPS on synthesising ZrC-20Mo and ZrC-20TiC had minimal impact on mechanical properties compared to conventional SPS. HPHT SPS also afforded the opportunity to sinter ZrC-20Mo in a non-carburising environment as the samples were encased in tantalum foil. However, rather having Mo react with native graphite, the Mo instead reacted with ZrC, producing a solid solution (Zr,Mo)C and MoC.

ZrC-20Mo and ZrC-20TiC composites underwent high-temperature XRD testing. In ZrC-20Mo, ZrC oxidised into ZrO_2 species, while the Mo species yielded MoO_3, which is volatile and vaporised above 800 °C. ZrC-20Mo underwent MoO_3 vaporisation and pesting at 1200 °C, where the sample was reduced to powder. However, there was also evidence suggesting mixed oxide formation. ZrC-20TiC produced a thin, plate-like crust, which inhibited the progression of oxide penetration deep into the macrostructure. The surface was characterised by the formation of the typical ZrO_2 and TiO_2 compounds, but also mixed oxides $(Zr,Ti)O_2$.

When ZrC was doped into WC-8Ni and subjected to a series of increasing aggressive tribological wear tests, the results show ZrC to be ineffective in providing any tangible wear resistance benefits compared to pure WC-Ni. Conversely, addition of TiC provides improved resistance to low-stress abrasion wear conditions, but became increasingly less effective with high-stress wear.

Finally, in the third stream, ZrC was sintered with nickel and processed into granulate powders to be used as a reinforcement particulate to metal matrix composite hardfacing applied by PTA welding. The new coatings proved to resist abrasion and impact abrasion wear up to 700 °C compared to commercial WC reinforcement. This is due to the higher oxidation resistance up to 700 °C and formation of protective oxide layers and mixed oxide layers on the carbide and surrounding matrix.

In conclusion, from the three research streams, it is for the first time ZrC-Mo is studied by SPS technology. SPS at higher compaction pressures improves the fracture toughness of ZrC-20TiC. Furthermore, the study of oxidation mechanics and behaviour of ZrC-Mo and ZrC-TiC composites offers detailed insight into the weight change and phase transitions and species at high-temperatures. Although ZrC is not an effective dopant for WC hardmetals, using ZrC as a reinforced hardfacing in PTA coating showed ZrC to be an effective alternative to WC for high-temperature wear abrasion applications.

KOKKUVÕTE

ZrC baasil ja ZrC-ga legeeritud komposiitmaterjalid rakendusteks kõrgtemperatuursetes ja kulumistingimustes

Arenev tehnoloogia tagab alati uute ning paremate rasketes ning oksüdatiivsetes keskkondades töötavate materjalide arengu. Tuumaenergeetikas kasutatakse radioaktiivsete materjalide vooderdamiseks komposiitpindeid, mis töötavad oksüdatiivses keskkonnas temperatuuril kuni 1000 °C. Sarnaselt nõuavad kosmoseraketid vooderdust, mis peab vastu atmosfääri sisenemisel temperatuurile kuni 1200 °C ning oksüdeerumisele. Üheks materjaliks, mis talub kiiritusest tekitatud kahjustusi kõrgetel temperatuuridel on tsirkooniumkarbiid (ZrC). Samas on ZrC puuduseks madal purunemissitkus ning oksüdatsioonikindlus.
Käesoleva uurimustöö võib jagada kolmeks osaks: 1) Sädeplasmapaagutuse (SPS) teel valmistatud ZrC komposiidid (uuritakse ZrC sitkuse ning oksüdatsioonikindluse tõstmise võimalusi); 2) ZrC lisandi kasutamine dopeeriva agendina kulumiskindluse tõstmiseks WC baasil kõvasulamites; 3) ZrC lisandi kasutamine Ni baasil PTA pinnetes kõrgtemperatuurse abrasiivkulumiskindluse tõstmiseks.

Esimeses osas keskendutakse kahele ZrC komposiidile: ZrC-20Mo ja ZrC20TiC. Pulbrite kiiremat konsolideerimist võimaldab SPS meetodi kasutamine koos kõrgendatud survetega. ZrC-20Mo paagutamine on temperatuurist sõltuv protsess, mis sõltub ka Mo kogusest koostises. Kõrgeim purunemissitkus saavutati paagutades 2100 °C juures, kusjuures pressimissurve mõju ei avaldanud. Vastupidiselt, et tõsta ZrC-20TiC purunemissitkust, oli vajalik kasutada kõrgendatud pressimissurveid (100 MPa) sarnastel paagutustemperatuuridel. Faaside segunemise piiramine tänu madalamale SPS temperatuurile, parandab TiC materjali sitkust prao liikumise takistajana. Kõrgtemperatuurse ning kõrgsurve (HPHT) SPS mõju teistele ZrC-Mo ja ZrC-TiC mehhaanilistele omadustele võrreldes tava SPS-ga, puudus. HPHT SPS katsetused viidi ZrC-Mo puhul läbi ka mittekarburiseerivas keskkonnas, kasutades Ta fooliumiga kaetud katsekehi. Selle asemel, et Mo reageeriks grafiidiga, toimus reaktsioon ZrC-ga saades (Zr,Mo)(C) ja Mo(C) tardlahuse.

ZrC-20Mo ja ZrC-TiC komposiitidele tehti kõrgtemperatuursed XRD uuringud. ZrC-20Mo puhul ZrC muundus ZrO_2 osakesteks ning Mo ühendid muutusid volatiilseks MoO_3 faasiks, mis aurustus temperatuuridel üle 800 °C. ZrC-Mo puhul toimus MoO_3 aurustumine 1200 °C juures, kus komposiidid muutusid pulbriks. Samuti leiti tõendeid seguoksiidide tekke kohta. ZrC-20TiC pinnale tekkis õhuke plaatjas koorik, mis takistas oksiidide tungimist sügavale makrostruktuuri. Pinnal leiti tüüpilisi ZrO_2 ja TiO_2 ühendeid kui ka $(Zr,Ti)O_2$ seguoksiide.

Triboloogiliste uuringute käigus (teine osa) selgitati, et WC-8Ni kõvasulamite legeerimine ZrC osakestega on ebaefektiivne tõstmaks WC-Ni kulumiskindlust. TiC seevastu tõstab madalal survel abrasiivkulumiskindlust, kuid oli ebaefektiivne kõrgemate survete juures.

Kolmandas uurimissuunas paagutati ZrC koos nikliga, moodustades komposiitgraanulid, mida kasutati metallmaatrikskomposiitsete PTA pinnete valmistamiseks. Uudsete pinnete juures leiti, et antud materjalidel on kõrge abrasiooni ja löökabrasioonkulumiskindlus temperatuuridel kuni 700 °C, mis on kõrgem tööstuslikest pinnetest WC baasil. See on tänu kõrgemale oksüdatsioonikindlusele, kui tekib kaitsvate oksiidide kiht karbiididele ja ümbritsevale maatriksile.

Kokkuvõtteks, kolmes erinevas uuringusuunas uuriti esmakordselt SPS konsolideerimist SPS meetodil. Kõrgete pressimissurvete juures tõstab SPS ZrC-20TiC purunemissitkust. Oksüdatsiooniprotsessi mehhaanika uurimine andis detailse ülevaate ZrC-Mo ja ZrC-TiC komposiitide kõrgtemperatuursetest kaalu- ning faasimuutustest. Kuigi ZrC ei ole WC kõvasulamite puhul efektiivne legeerlisand on ta ZrC PTA pinnete komponendina kasutades alternatiiviks WC-le kõrgtemperatuurse kulumiskindluse tingimustes.

Curriculum vitae

1. Personal data

Name	Der-Liang
Date and place of birth	30.12.1982, Vancouver, Canada
E-mail address	der-liang.yung@ttu.ee

2. Education

Period	Educational institution	Education (Programme/degree)
2010	Tallinn University of Technology	Sustainable Energetics and Materials Sciences / Master
2005	Simon Fraser University	Biochemistry / Bachelor
2000	Ideal Mini School	Sciences / High school

3. Language competence/skills (fluent, good, basic skills)

Language	Level
English	Fluent
French	Fluent
Chinese	Basic

4. Professional employment

Period	Organization	Position
2010-…	Tallinn University of Technology, Tallinn, Estonia	Researcher
2007 - 2009	Voluntary Service Overseas	Intern
2006 - 2007	NetCrop overseas, industry Canada	Intern

5. Activities

Period	Organisation	Position
2012-2014	International Club tutor, TUT	Member
2012	BEST Estonia	Participant
2010-2011	Canadian representative, Teeviit	Volunteer

6. Research visits

Period	Organisation
3.2016-3.2016	Institute of Advanced Manufacturing Technology, Krakow Poland, research stint
10.2014-3.2015	Institute of Ceramics and Glasses, Madrid, Spain, DORA internship
06.2011.08-2011 06.2012-08-2012	AC2T research GmbH; Vienna, Austria, research internship

7. Fellowships and awards

Period	Organisation
2016	FameLab final speaker contestant representing Estonia
2015	Award for the student speakers, 2nd place 24th International Conference BALTMATTRIB-2015
2013	Award for the student speakers, 2nd place 22nd International Conference BALTMATTRIB-2013
2012	Cum Laude MSc Engineering, TUT

Elulookirjeldus

1. Isikuandmed

Ees- ja perekonnanimi	Der-Liang Yung
Sünniaeg ja –koht	30.12.1982 Vancouver, Kanada
E-posti aadress	der-liang.yung@ttu.ee

2. Hariduskäik

Lõpetamise aeg	Õppeasutus (nimetus lõpetamise ajal)	Haridus (kraad/eriala)
2010	Tallinna Tehnikaülikool	Sustainable Energetics and Materials Sciences / Magister
2005	Simon Fraser University	Biokeemia / Bakalaureus
2000	Ideal Mini School	Loodusteadused / High school

3. Keelteoskus

Keel	Tase
Inglise	Emakeel
Prantsuse	Emakeel
Hiina	Kõrg

4. Täiendusõpe

Töötamise aeg	Tööandja nimetus	Ametikoht
2010-…	Tallinna Tehnikaülikool, Tallinn, Estonia	Nooremteadur
2007 - 2009	Voluntary Service Overseas	Nooremteadur
2006 - 2007	NetCrop overseas, industry Canada	Nooremteadur

5. Tegevus

Töötamise aeg	**Asutus**	**Ametikoht**
2012-2014	International Club juhendaja, TUT	Liige
2012	BEST Estonia	Liige
2010-2011	Canadian representative, Teeviit	Vabatahtlik

8. Enesetäendamine

Kestus	**Asutus**
3.2016-3.2016	Institute of Advanced Manufacturing Technology, Krakow Poland, Nooremteadur
10.2014-3.2015	Institute of Ceramics and Glasses, Madrid, Spain, DORA Nooremteadur
06.2011.08-2011 06.2012-08-2012	AC2T research GmbH; Vienna, Austria, Nooremteadur

9. Fellowships and awards

Aasta	**Asutus**
2016	FameLab final speaker contestant representing Estonia
2015	Award for the student speakers, 2nd place 24th International Conference BALTMATTRIB-2015
2013	Award for the student speakers, 2nd place 22nd International Conference BALTMATTRIB-2013
2012	Cum Laude MSc Tallinna Tehnikaülikool

Other publications

Submitted papers, which contents are included in the thesis, BUT NOT YET PUBLISHED

Yung DL, Maaten B, Antonov M, Hussainova I. Spark plasma sintered ZrC-Mo cermets: Oxidation of spark plasma sintered ZrC-Mo and ZrC-TiC composites. *International Journal of Refractory Metals and Hard Materials*. (under review)

Author's contribution: Design of experiments, testing, writing, data analysis

Yung DL, Zikin A, Hussainova I, Danninger H, Badisch E, Gavrilovic A. Oxidation and Tribological performances of ZrC-Ni and TiC-Ni cermet reinforced PTA hardfacings at elevated temperatures. *Surfaces and Coatings Technology*. (under review)

Author's contribution: Testing, writing, data analysis

Some of the work during the PhD period centred on research and development concerning Project NeTTUN: research into new materials for tunnel boring machine drag bits inserts. Much of the research focused on cemented WC-Co/WC-Ni, their synthesis and wear behaviour. Below are some of the publications. These results are not included in the thesis.

1. Umalas M, Hussainova I, Reedo V, **Yung DL,** Cura E, Hannula SP, Lõhmus R, Lõhmus A. Combined sol–gel and carbothermal synthesis of ZrC–TiC powders for composites. *Materials Chemistry and Physics*. (2015) 153, 301−306, DOI: dx.doi.org/10.1016/j.matchemphys.2015.01.017

2. **Yung DL**, Antonov M, Hussainova I, Veinthal R, Hogmark S. Effect of coarse-to-fine WC grain ratio on mechanical properties and abrasive wear of WC-8Co cemented carbides. *Tribology*. (2016) 47 (265), 103−115, DOI: http://yadda.icm.edu.pl/yadda/element/bwmeta1.element.baztech-348c404f-1e34-47a3.a432-7a6dc6c29849

Author's contribution: Design of the experiments; Testing; Data analysis; Writing

3. Marou Alzouma O, Azman MA, **Yung DL**, Fridrici V, Kapsa Ph. Influence of different reinforcing particles on the scratch resistance and microstructure of different WC–Ni composite. *Wear*. (2016) 352–353, 130−135, DOI: dx.doi.org/10.1016/j.wear.2016.02.011

   Author's contribution: Synthesis of the tested samples; Writing concerning material synthesis

4. Antonov M, Veinthal R, **Yung DL**, Katušin D, Hussainova I. Mapping of impact-abrasive wear performance of WC–Co cemented carbides. *Wear*. (2015) 332-333, 971−978,
   DOI: dx.doi.org/10.1016/j.wear.2015.02.031

   Author's contribution: Synthesis of the tested samples; Writing concerning material synthesis; Presenting results at Wear of Materials Conference

5. **Yung DL.**, Dong M, Hussainova I. Effect of grain growth inhibitors VC/Cr3C2 on WC-ZrO_2-Ni composite mechanics. In: D. Loca (Ed.). Engineering Materials & Tribology XXII (106−109). Trans Tech Publications Ltd. (*Key Engineering Materials*. (2014) 604).

   Author's contribution: Design of the experiments; Testing; Data analysis; Writing

Approbation (conferences)

6. **Yung D**, Antonov M, Hussainova I, Veinthal R, Hogmark S. Composite and structure of bimodal WC-Co materials related to mechanical properties and abrasive wear. Ed. Silva Gomes, Shaker A. Meguid Ed. J.F. Silva Gomes, Shaker A. Meguid. *6th International Conference Mechanics and Materials in Design.* (2015), 253−255.

7. **Yung DL**, Dong M, Hussainova I. Comparing tungsten carbide based composites reinforced by alumina nanofibers or zirconia. *In: Proceedings of the PM13 International Conference on Powder Metallurgy and*

Particulate Materials, 8: International Conference on Powder Metallurgy and Particulate Materials. June 24 - 27, 2013, Chicago, USA. USA: MPIF/APMI Metal Powder Industry Publications, USA, 24−35.

8. **Yung DL**, Kollo L, Hussainova I, Zikin A. Reactive sintering of zirconium carbide based systems. *In: Otto, T.,* Ed. Otto, T. TUT press, 783−788. *Proceedings of the 8th International Conference of DAAAM Baltic Industrial Engineering.* 19-21st April 2012, 566-570, Tallinn, Estonia

9. Zikin A, **Yung DL**, Hussainova I, Danninger H, Pirso J, Gavrilović-Wohlmuther A. (2013). Deposition and characterization of refractory cermet particle reinforced Ni-based PTA hardfacings. *In:* Austria, *Proceedings of the 18th PLANSEE Seminar*. (2013), 356-361

Paper I: Yung DL, Hussainova I, Rodriguez MA, Traksmaa R. Processing of ZrC-TiC Composites by SPS. *Key Engineering Materials*. (2016) 674, 94–99, DOI: 10.4028/www.scientific.net/KEM.674.94

Processing of ZrC-TiC composites by SPS

Der-Liang Yung[1,a*], Irina Hussainova[1,b], Miguel A. Rodriguez[2,c], Rainer Traksmaa[1,d]
[1]Dept of Material Engineering; Tallinn University of Technology, Ehitajate 5, 19086 Tallinn, Estonia
[2]Institute de Ceramica y Vidrio; Campus De Cantablanco, C/Kelsen 5, 28049 Madrid, Spain
[a] der-liang.yung@ttu.ee, [b] Irina.Hussainova@ttu.ee, [c] mar@icv.csic.es, [d] Rainer.Traksmaa@ttu.ee

Keywords: Spark Plasma Sintering, ZrC-based composites, Mechanical Properties, Microstructure

Abstract

ZrC – TiC composites containing 20 wt.% TiC, along with and without 0.2 wt.% graphite were prepared by spark plasma sintering (SPS) at temperatures between 1600 - 1900 °C for 10 min under pressure up to 100 MPa. The addition of free carbon tends to reduce the appearance of tertiary phases in the microstructure according to scanning electron microscope (SEM) images. However, free carbon also reduced the mechanical properties of Vickers' hardness and fracture toughness of the composites. SPS data showed when pressure was increased to 100 MPa, evident grain growth started to occur at a temperature as low as 1600 °C resulting in relative density > 100%. Samples produced at 1600 °C, but with maximum allowable pressure according to the SPS machine, yielded samples with greater hardness and fracture toughness compared to samples produced at 1900 °C.

Introduction

Ultra High Temperature Ceramics (UHTCs) are found in applications ranging from materials for cutting tools, jet engine parts, nose caps and leading edge re-entry space aircraft. Zirconium carbide (ZrC) is one such material given its high melting point (3500 °C), resistance to irradiation, and refractory hardness (~25GPa). However, full densification of pure ZrC is an ongoing challenge and the material's low fracture toughness (~4 MPa $m^{1/2}$) and flexure strength (~250 MPa) is a limiting factor in the scope of possible applications [1-5]. Previous efforts have included using nanopowder dopants such as yttria stablised zirconia. The presence of tetragonal zirconia is meant to induced toughening through residual stresses and possible transformation of zirconia grains [1]. However, zirconia toughening is a complicated process compounded by the need to have exact parameters and optimization. Using elemental molybdenum to make ZrC-Mo cermets has shown to increase overall composition flexure strength, even at a cost of hardness [2, 6-8]. Molybdenum facilitates easier densification of the material due to the formation of liquid phase Mo_2C at temperatures exceeding 2000 °C. The result is that ZrC grains become encased in a continuous matrix Mo and Mo_2C [2].

Recently, research has veered towards using spark plasma sintering (SPS) as a fast, ideal way to sinter ZrC and its composites [9-11]. Due to the rapid sintering process alluded to SPS, material grain growth is limited, thereby, yielding improved mechanical properties. Although SPS grants superior temperature and pressure control to the sintering process, the applied pressures during sintering is restricted to the type of machine and available molds. Previous research on SPS has centered on sintering samples at pressure up to only 50 MPa [1, 11, 12]. Yet, using a system like Sinter-HIP, a pressure of up to 200 MPa is achievable under pressurized argon, usually for purposes of eliminating porosity from the microstructure [13]. In the present study, samples of ZrC-20wt.%TiC are subjected to SPS under varying temperatures. Pressure is dialed to the maximum allowable, given the model of SPS and the size of the graphite molds. The goal is to determine the effect of compaction pressure during sintering to the resulting mechanical properties. The ZrC and TiC powders have also undergone high-energy attrition milling to enhance the composite sinterability [14]. Mechanical test including hardness and fracture toughness and flexural strength are measured along with scanning electron microscope (SEM) and x-ray diffraction (XRD) analysis.

Materials and Methods

Commercially available ZrC powder (~3.6 μm, Pacific Particulate Materials, 99% purity ZrC-7643) underwent high-energy attrition milling with 20 wt.% of TiC powder (2-3 μm, Pacific Particulate Materials, 99% purity TiC-2088). This composed of sample PH1. The blend was milled using WC-Co medium (6-7 mm Ø) at a ball-to-powder ratio of 12:1 wt.% for 48 h at 800 rpm in ethanol. A second batch of ZrC-TiC powders in the same proportions was almost made, PH2, contained 0.2 wt.% of free graphite additives (6.2-12.5 μm, TIMREX, 99.4% purity KS10) mixed in with the mill.

Spark plasma sintering technique (Dr. Sinter SPS-1050-CE) was used to sinter powders under argon at 1600-1900 °C. This SPS has the capability, using 20 mm Ø graphite, cylindrical molds, to compact samples up to 100 MPa and at temperatures up to 2000 °C. The heating rate was set at a relatively slow 100 °C/min with a dwelling time of 10 min at the final temperature for all samples. ZrC-TiC composites are densified by means of solid state sintering, which is a common pathway for producing high temperature ceramics and composites. The compaction pressure was initially applied at room temperature and kept constant throughout the sintering regime.

Specimen density was determined by Archimedes' method with distilled water as an immersing medium. The bulk Vickers' hardness was estimated with Indectec hardness measuring machine (HV10) and the indentation fracture toughness (IFT) was calculated by resorting to both an average of the Palmqvist and Median crack systems [15]. The reported hardness and fracture toughness constitute the mean and standard deviation values of 10 indentations. To determine transverse rupture strength (TRS), samples were cut to the appropriate pieces using a low-speed rotary cutter fitted with diamond disk. After the samples were grinded and polished to a 3 μm diamond finish, three-point bending tests were perform under a 5 T Instron press. The microstructure was examined under scanning electron microscopy (FE-SEM Hitachi S-4700, Japan) after diamond polishing to 1 μm and gold plating. Chemical composition was analyzed with X-ray diffraction analysis (XRD, Philips PW3830 X-ray Generator, 4 kW, Cu-Anode) using CuK$_\alpha$ radiation at the accelerating voltage of 40 kV and a filament current of 30 mA with a scan step size of 0.02° and a count time of 0.4 s at each step.

Results and Discussion

While compaction pressure is kept at 100 MPa for all experiments, the differences in mechanical properties can be attributed to the sintering temperature and the presence or absence of free graphite. Table 1 shows the mechanical properties of the samples and relative density in dependence on the sintering temperature. The difference in density is mainly due to the intrinsic nature of SPS: high energy, low-voltage pulsed current, and high localized temperatures [16]. At a temperature of 1900 °C, due to the added reactivity from high-energy milling of the powders and relatively long dwelling time (10 min), the grains evidently coarsen. This is reflected in the mechanical properties of hardness and fracture toughness where samples sintered at 1900 °C show lower values compared to those sintered at 1600 °C. However, larger grains due to the coarsening and grain growth would result in improved bending strength between the two temperatures. The stark contrast with grain refinement is show in Fig. 1, where SEM images show sample PH1 at 1900 °C and 1600 °C, respectively. The microstructure of PH1 sintered at 1600 °C exhibits a fine, uniform microstructure with no exaggerated grain growth, Fig. 1b. The pattern of breakage during the bending tests appears to indicate an intragranular fracture for the grains for PH1 sintered at 1900 °C. This is evident by the appearance of smooth surfaces at particular breakage points seen in Fig. 1a.

Table 1. Mechanical properties of PH1 and PH2 at different SPS temperatures

Sample Code	Temperature °C	Densification [%]	Hardness [HV10]	IFT [MPa*m$^{1/2}$]	TRS [MPa]
PH1	1900	101.7	1731±26	4.6±1.2	742±56
PH2	1900	101.5	1643±31	4.1±1.1	840±78
PH1	1600	98.4	1898±53	5.3±1.5	688±134
PH2	1600	98.5	1728±33	5.3±1.5	744±74

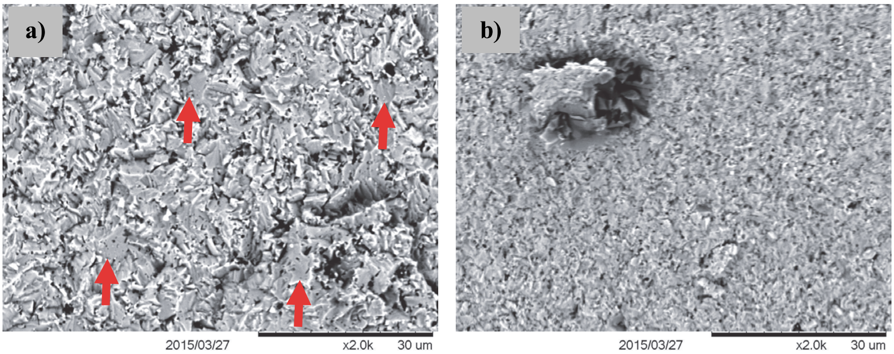

Fig. 1. SEM morphology of the unpolished, cross-section of PH1 at 1900 °C (a) and 1600 °C (b), respectively. Red arrows indicate smooth breakage points of grains Fig.1a.

Data collected during the SPS cycle supports the notion that grain coarsening occurs at higher temperatures. Although pressure is kept constant throughout the entire sintering regime, the SPS compaction piston compresses incrementally during the process until reaching 1600 °C. In the initial sintering until 1900 °C, the piston is seen to compress and stops shortly at approximately 1600 °C before depressing gradually as the temperature increases beyond 1600 °C, Fig. 2a. This would indicate that the window of grain coarsening would occur at temperatures beyond 1600 °C. Further optimization of the SPS regime could be considered since the temperature ramp rate is relatively slow and the dwell time is long. Fig. 2b. shows that a fully densified sample is already achieved at 1600 °C, before the dwell time, suggesting a slow ramp rate and high compaction pressure is more than sufficient for densification.

The effect of free graphite addition to the milled powder was also studied. Carbon seems to have an impact on transverse rupture strength and hardness. Other research with carbon nanotubes up to 0.5 wt.% significantly increases the fracture toughness of ZrC-TiC composites [17]. Carbon level could also affect grain coarsening, where average grain size increases with increasing carbon activity [18]. At either sintering temperature, the PH2 exhibited better bending strength at the expense of hardness, Table 1, than samples with no free graphite.

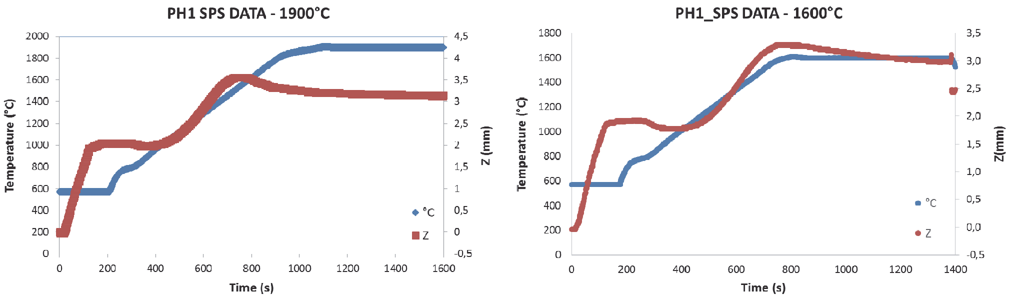

a) **b)**

Fig. 2. SPS data cycle regime detailing the compaction piston movement (Z) in relation to temperature for samples PH1 at 1900 °C (a) and 1600 °C (b), respectively.

The purpose behind performing an experiment by adding free graphite to ZrC-TiC powder surrounded the supposed issue of carbon vacancies, specifically the effect of sub-stoichiometry on the basic thermodynamic properties of the system. The effect of carbon vacancies on the critical temperature of the miscibility gap can be as high as 600 °C range [12]. This could affect the composition of ZrC-TiC, depending on sintering temperature. None of the SEM images shows appearance of a third carbon phase in the microstructure, nor any additional peaks in XRD analysis.

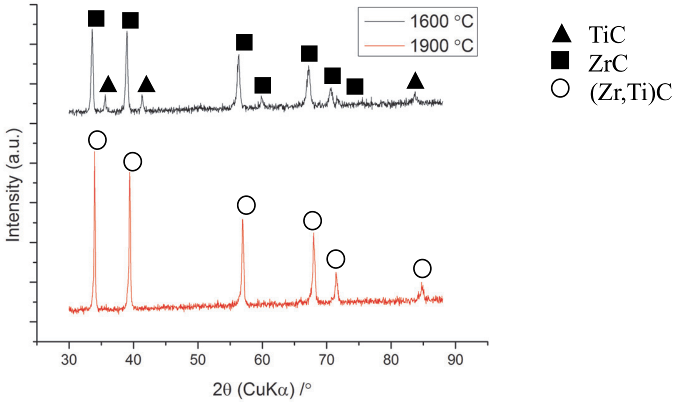

Fig. 3. XRD patterns of ZrC-TiC PH1 at 1900 °C (bottom, red) and 1600 °C (top, black), respectively.

XRD analysis on sample PH1 at the two temperatures show a contrast view of the chemical composition. Fig. 3. shows that at 1900 °C, all the peaks indicate the presence of a solid-state (Zr,Ti)C phase. The higher sintering temperature drives the formation of (Zr,Ti)C; the miscibility gap for a composition of ZrC-20wt.%TiC has been established to be ~1900 °C [16]. This phenomenon can explain the lower fracture toughness results as the lack of a dual phase structure inhibiting TiC's ability to act as a toughening carbide. This also explains the difference in relative densities in Table 1, where samples sintered at 1900 °C showed above relative density due to the driven yield of (Zr,Ti)C. Under high-resolution SEM images of crack propagation for PH1 at 1600 °C, the second phase TiC acts as crack deflectors, Fig. 4a; the crack is seen to stop subsequently and deviate around the TiC grain before continuing. Fig. 4b show a crack deviating underneath the TiC particle like a bridge.

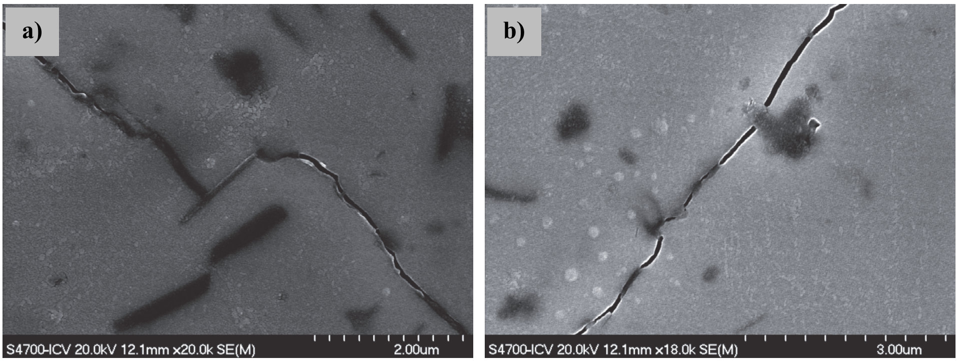

Fig. 4. PH1 sintered at 1600 °C: a) TiC crack deflector along the grain; b) TiC deflects crack under the grain.

Conclusion

ZrC-20wt.%TiC composites were made with and without graphite dopant and sintered under 100 MPa, spark plasma sintering at 1600 and 1900 °C. Results indicate that the addition of free graphite improves the toughness of the composites, but lowers hardness. The role of maximum allowable compaction pressure from SPS allowed ZrC-20wt.%TiC to be sintered at 1600 °C with refine microstructure and better mechanical properties as compared to the sample produced at 1900 °C. Sintering at 1600 °C allowed ZrC-20wt.%TiC to maintain its dual carbide structure allowing TiC to act as toughening agent and deflect crack propagation around or underneath the TiC grains.

Acknowledgements

The Archimedes' Foundation of Estonia under the auspices of the Dora 6 program granted financial support for this research. The author also wishes to thank the Institute de Ceramica y Vidrio, Madrid, Spain, for hosting the research and providing materials and access to facilities and expertise. This work was also supported by institutional research funding IUT (19-29) of the Estonian Ministry of Education and Research.

References

[1] I. Hussainova, N. Voltšihhin, E. Cura and S.-P. Hannula, *Densification and characterization of spark plasma sintered ZrC–ZrO2 composites.* Materials Science and Engineering: A. 597: (2014) p. 75-81

[2] S.E. Landwehr, G.E. Hilmas, W.G. Fahrenholtz and I.G. Talmy, *Processing of ZrC–Mo Cermets for High Temperature Applications, Part II: Pressureless Sintering and Mechanical Properties.* Journal of the American Ceramic Society. 91(3): (2008) p. 873-878

[3] C.B. P. Barnier, F. Thevenot, *Hot-pressing kinetics of zirconium carbide.* Journal of Material

Science. 21: (1986) p. 2547-2552

[4] M. Umalas, I. Hussainova, V. Reedo, D.-L. Young, E. Cura, S.-P. Hannula, R. Lõhmus and A. Lõhmus, *Combined sol–gel and carbothermal synthesis of ZrC–TiC powders for composites.* Materials Chemistry and Physics. 153: (2015) p. 301-306

[5] D.L. Yung, L. Kollo, I. Hussainova and A. Žikin, *Reactive Sintering of ZrC-TiC Composites.* Key Engineering Materials. 527: (2012) p. 20-25

[6] S.E. Landwehr, G.E. Hilmas, W.G. Fahrenholtz and I.G. Talmy, *Processing of ZrC?Mo Cermets for High-Temperature Applications, Part I: Chemical Interactions in the ZrC?Mo System.* Journal of the American Ceramic Society. 90(7): (2007) p. 1998-2002

[7] S.E. Landwehr, G.E. Hilmas, W.G. Fahrenholtz, I.G. Talmy and S.G. DiPietro, *Microstructure and mechanical characterization of ZrC–Mo cermets produced by hot isostatic pressing.* Materials Science and Engineering: A. 497(1-2): (2008) p. 79-86

[8] X. Zhang, N. Liu and C. Rong, *Microstructure and fracture toughness of TiC–ZrC–WC–Mo–Ni cermets.* International Journal of Refractory Metals and Hard Materials. 26(4): (2008) p. 346-356

[9] Y. Li, H. Katsui and T. Goto, *Spark plasma sintering of TiC–ZrC composites.* Ceramics International. 41(5): (2015) p. 7103-7108

[10] S. Liu, W. Hu, J. Xiang, F. Wen, B. Xu, D. Yu, J. He, Y. Tian and Z. Liu, *Mechanical properties of nanocrystalline TiC–ZrC solid solutions fabricated by spark plasma sintering.* Ceramics International. 40(7): (2014) p. 10517-10522

[11] D. Sciti, S. Guicciardi and M. Nygren, *Spark plasma sintering and mechanical behaviour of ZrC-based composites.* Scripta Materialia. 59(6): (2008) p. 638-641

[12] V.I. Razumovskiy, A.V. Ruban, J. Odqvist, D. Dilner and P.A. Korzhavyi, *Effect of carbon vacancies on thermodynamic properties of TiC–ZrC mixed carbides.* Computer Coupling of Phase Diagrams and Thermochemistry. 46: (2014) p. 87-91

[13] M.H. Bocanegra-Bernal, *Hot Isostatic Pressing (HIP) technology and its applications to metals and ceramics.* Journal of Material Science. 39: (2004) p. 6399-6420

[14] L. Zhao, D. Jia, X. Duan, Z. Yang and Y. Zhou, *Pressureless sintering of ZrC-based ceramics by enhancing powder sinterability.* International Journal of Refractory Metals and Hard Materials. 29(4): (2011) p. 516-521

[15] F. Sergejev, M. Antonov; *Comparative study fracture toughness cermet and composites.* Proceedings of Estonian Academia. 12(4): (2006) p. 388-398

[16] S.-K. Sun, G.-J. Zhang, W.-W. Wu, J.-X. Liu, T. Suzuki and Y. Sakka, *Reactive spark plasma sintering of ZrC and HfC ceramics with fine microstructures.* Scripta Materialia. 69(2): (2013) p. 139-142

[17] R.B. Acicbe and G. Goller, *Densification behavior and mechanical properties of spark plasma-sintered ZrC–TiC and ZrC–TiC–CNT composites.* Journal of Materials Science. 48(6): (2012) p. 2388-2393

[18] I. Borgh, P. Hedström, T. Persson, S. Norgren, A. Borgenstam, J. Ågren and J. Odqvist, *Microstructure, grain size distribution and grain shape in WC–Co alloys sintered at different carbon activities.* International Journal of Refractory Metals and Hard Materials. 43: (2014) p. 205-211

Paper II: **Yung DL**, Antonov M, Hussainova I. Spark plasma sintered ZrC-Mo cermets: Influence of temperature and compaction pressure. *Ceramics International*. (2016) 42 (11), 12907−12913, DOI: dx.doi.org/10.1016/j.ceramint.2016.05.059

Ceramics International 42 (2016) 12907–12913

Contents lists available at ScienceDirect

Ceramics International

journal homepage: www.elsevier.com/locate/ceramint

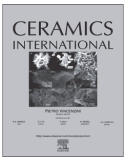

Spark plasma sintered ZrC-Mo cermets: Influence of temperature and compaction pressure

Der-Liang Yung*, Maksim Antonov, Irina Hussainova

Department of Mechanical Engineering, Tallinn University of Technology, Ehitajate tee 5, Tallinn 19086, Estonia

ARTICLE INFO

Article history:
Received 14 March 2016
Received in revised form
21 April 2016
Accepted 9 May 2016
Available online 13 May 2016

Keywords:
Spark plasma sintering
Cermets
Mechanical Properties
ZrC-Mo

ABSTRACT

The microstructure analysis and mechanical characterisation were performed on a ZrC-20 wt%Mo cermet that was spark plasma sintered at various temperatures ranging between 1600 and 2100 °C under either 50 or 100 MPa of compaction pressure. The composite reached ~98% relative density for all experiments with an average grain size between 1 and 3.5 μm after densification. The nature of SPS technology caused a faster densification rate when higher compaction pressures were applied. The difference in compaction pressures produced different behaviors in densification and grain structure: 1900 °C, 100 MPa produced excessive grain growth in ZrC; 1600 °C, 50 MPa revealed a very clear ZrC grain structure and Mo diffusion between carbide grains; and 2100 °C, 50 MPa exhibited the highest overall mechanical properties due to small clusters of Mo phases across the microstructure. In fact, this particular sintering regime gave the most optimal mechanical values: 2231 HV10 and 5.4 MPa*m$^{1/2}$, and 396 GPa Young's modulus. The compaction pressure of SPS played a pivotal role in the composites' properties. A moderate 50 MPa pressure caused all three mechanical properties to increase with increasing sintering temperature. Conversely, a higher 100 MPa pressure caused fracture toughness and Young modulus to decrease with increasing sintering temperature.

1. Introduction

Zirconium carbide (ZrC) is a refractory transition metal carbide from the Group IV of the periodic table and it has received attention as either an additive or a base material for composite alloys. ZrC's most notable properties includes its high melting pointing (~3420 °C), high hardness (~25.5 GPa), high electrical conductivity (7.8 × 10^{-7} Ω cm), and high Young modulus of elasticity (~400 GPa) [1]. A common application for ZrC alloys is in the nuclear industry in the form of shields for cladding nuclear materials [2–8]. ZrC outperforms silicon carbide (SiC) amorphization during irradiation exposure due to its mixture of covalent, metallic and ionic bonds [8]. Unfortunately, pure ZrC is also plagued by low fracture toughness (~4.0 MPa*m$^{1/2}$), which makes it undesirable for mechanically rigorous applications [1,9–12]. Because it is a promising refractory carbide, various attempts have been made to improve the toughness and mechanical performance of ZrC including *syn*thesising ZrC based cermets using molybdenum (Mo) [4,10,13–17]; producing carbide-carbide composites with titanium carbide (TiC) resulting in solid-state solution depending on sintering temperature [7,12,18–20]; or producing carbide-ceramic composites using zirconia's tetragonal toughening mechanism [9].

In studies of Mo-ZrC cermets, the samples were produced by arc melting for joining composites in conditions up to 2000 °C in Ar atmosphere with annealing in cast materials [21,22]. Landwehr et al. [4,10,13,14] performed a series of experiments with ZrC-Mo composites sintered in carburising and carbon-free environments in vacuum up to 2200 °C. Though the research showed that ZrC and Mo can be densified by liquid phase sintering, the formation of Mo_2C was a common occurrence when sintering Mo in a carburising environment yielding spots of brittle areas in the microstructure. It was determined that the presence of Mo_2C was not detected at 2100 °C in the carbon-free atmosphere, confirming the existing phase equilibria in the Zr–Mo–C system [10,13]. For a ZrC-40 vol%Mo cermet, using hot isostatic pressing (HIP) up to 1800 °C at 200 MPa for 1 h, yielded a fracture toughness value of 6.6 MPa*m$^{1/2}$ with approximately 380 GPa Young's modulus value [14]. Using spark plasma sintering (SPS) in ZrC-Mo research has been rather limited. One example includes a study where ZrC particle-dispersed reinforcements into a Mo alloy matrix formed by SPS has been shown to improve the strength and plastic elasticity by two folds [15]. However, SPS technology applied to the synthesis of ZrC-Mo cermets has not been done.

Part of the reason why SPS is not common with cermet research maybe the nature of the technology. SPS's intrinsic features

---

* Corresponding author.
E-mail address: der-liang.yung@ttu.ee (D.-L. Yung).

http://dx.doi.org/10.1016/j.ceramint.2016.05.059
0272-8842/

include rapid heating rates, low sintering temperatures, and short holding times. Typically, SPS experiments involving WC-Co cermets, for example, yielded cemented carbides sintered in solid-state with relatively high hardness, but also lower fracture toughness compared to the same cermets produced by sinterHIP technology. In addition, SPSed cermets contained more eta phases in the microstructure for WC-Co [23–25]. Previous studies performed by the authors of this paper demonstrated that a composition of ZrC-20 wt% Mo (~ZrC-14 vol%Mo) was the optimal ratio for the cermet sintered under vacuum up to 1900 °C with mechanical properties HV$_{10}$ 1690 and 5.6 MPa*m$^{1/2}$ [26]. In this study, the same ZrC-20 wt%Mo composition is produced and undergoes a series of SPS experiments at temperatures ranging from 1600 to 2100 °C using two compaction pressures: 50 MPa or 100 MPa. These composites were then characterised under scanning electron microscopy (SEM), X-ray diffraction (XRD), and mechanical properties testing including hardness, fracture toughness, elastic modulus, and densification.

2. Materials and methods

Commercially available ZrC (~3.6 μm, Pacific Particulate Materials, 99% purity ZrC-7643) and Mo (1.0–3.0 μm, Pacific Particulate Materials, 99% purity Mo-7164) powders underwent ball milling in a ZrC-20 wt%Mo composition for 48 h. TiC-NiMo balls in a 8:1 wt% ball to powder ratio along with ethanol were used as milling mediums. The powder was dried for 24 h at 50 °C, then sieved to 200 μm.

A spark plasma sintering furnace (FCT Systeme GmbH) was used to sinter powders under vacuum between 1600 and 2100 °C. This SPS machine has the capability, using 20 mm Ø graphite (5 μm, Carbone of America, Grade 2333) cylindrical moulds, to compact samples up to 100 MPa and at temperatures up to 2200 °C. The heating parameters in Fig. 1 shows an example of one ZrC-Mo SPS experiments at 1900 °C with a relatively slow heating rate, 100 °C*min^{-1} up to 1300 °C, then a fast ramp at 300 °C*min^{-1} up to the final temperature, followed by a 5 min dwell. All samples were processed with the same heating parameters, but with the variable difference being final temperatures (1600–2100 °C) and compaction pressures (either 50 MPa or 100 MPa). The compaction pressure was applied starting from room temperature and kept constant throughout the entire sintering regime. One SPS experiment needed to be perform under nitrogen (N_2) gas (approx. 60 mbars) when the temperature exceeded 2000 °C to maintain the integrity of the graphite mould.

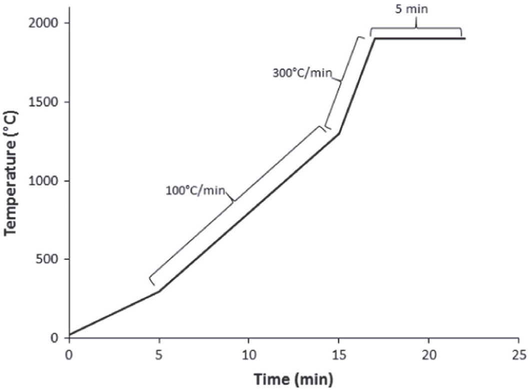

Fig. 1. heating parameters indicating ramp rate and dwell time for all samples; this final temperature is 1900 °C.

Specimen density was determined by Archimedes' method with distilled water as an immersing medium. The bulk Vickers' hardness was estimated with Indectec hardness measuring machine (HV$_{10}$) and the indentation fracture toughness (IFT) was calculated by resorting to the Palmqvist method [27]. Instrumented indentation testing for Young's moduli values was performed on a personal computer controlled Zwick 2.5/TS1S rig fitted with nano-indenter at 10 N load [28]. The reported mechanical properties constitute the mean standard deviation values of 6 indentations. The microstructures were examined under scanning electron microscopy (FE-SEM Hitachi S-4700, Japan) after diamond polishing to 1 μm and etching with $HF:HNO_3:H_2O$ (1:1:2 vol%) solution for 10 s. Chemical composition was analyzed with X-ray diffraction analysis (XRD, Philips PW3830 X-ray Generator, 4 kW, Cu-Anode) using CuK$_\alpha$ radiation. The accelerating voltage was 40 kV with a filament current of 30 mA, a scan step size of 0.02°, and a count time of 0.4 s at each step.

3. Results and discussions

3.1. *Densification of ZrC-Mo*

Sintering ZrC-Mo with SPS quickly poses two challenging aspects. The first is the well-known fact that Mo reacts with carbon, carburising itself into Mo_2C. Since SPS moulds in this case are typically composed of graphite, compaction dies and sheets, the carburisation of Mo in the final composite can reach 200 μm into the sample at 2000 °C [29]. The second challenge revealed itself during the SPS experiment of ZrC- Mo at 100 MPa beyond 1900 °C due to the intrinsic nature of the material and this proved to be impractical to continue for the sake of the lab equipment. While using 50 MPa, sintering was done up to 2100 °C without difficulty; however, applying 100 MPa caused problems in the post sintering processing. All samples sintered with 100 MPa survived the sintering intact; however, there was excessive extrusion of material around the centre of the mould and compacting dies. Although the moulds never broke during sintering, the breakages of the mould came when trying to extract the samples from the graphite moulds at room temperature. This occurred for samples sintered at 1800 and 1900 °C using 100 MPa of pressure. The decision was made to limit the experiments at these temperatures due to the limits of using graphite moulds. All samples SPSed using 100 MPa compaction used graphite Grade 2333 moulds, but even then, the excessive extrusion and bulging at the compaction centre of the mould caused them to break during extraction. No problems were reported when sintering the ZrC-Mo cermet using 50 MPa pressure.

The application of two compaction pressures at various temperatures between 1600 and 2100 °C shows pressure to have an influence on the densification of the material. There is an evident trend with the relative density of the ZrC-Mo cermet as indicated in Fig. 2: increasing sintering temperature slightly lowers the densification of the composite. The most likely explanation is a decrease in the fraction of Mo, which has a higher density (10.3 g/cm^3), compared to Mo_2C (approximately 8.9 g/cm^3), the carburisation product that forms as Mo reacts with graphite. The trend is duplicated at both compaction pressures; applying the higher 100 MPa pressure increased the overall densification by an additional 1% compared to samples pressed at 50 MPa. The fear with higher compaction pressures is the possibility to exceed the limiting factor of the powder's deformation degree, which would produce cracks in the microstructure. The resulting porosity due to high compacting pressure would lead to decrease in relative density of the sintered material [30]. This is not the case with ZrC-

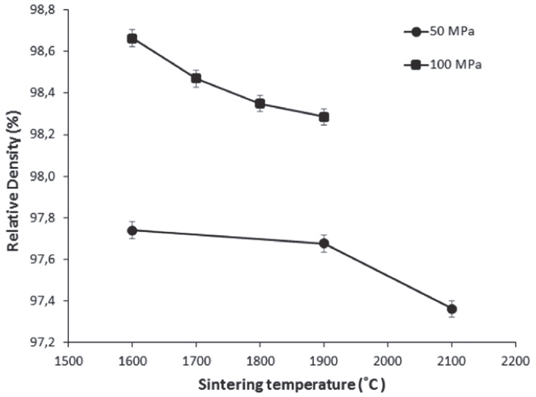

Fig. 2. Relative densities of ZrC-Mo with increasing temperature and different compaction pressures.

Mo in this study as the increase pressure leads to particle rearrangement and more effectively pack the metallic ductile Mo particles around ZrC. The applied pressure increases the number of contact points between particles as they come closer to each other, thereby reducing the effective diffusion distance leading to higher amount of densification [31]. Instead, the densification results of this study reflect the master sintering curve of Mo reinforcing the notion that the higher compaction pressure increases the activation energy and densification of Mo [32].

All experiments in this study had the compaction pressure applied starting from room temperature and the motion of the piston was recorded during the whole sintering process. The so called "relative piston travel", measured in millimetres, contains information about linear intrinsic shrinkage of every sample. However, to make a proper interpretation of the data, the experimental values had to be corrected. Normally, this would be a complicated process, taking into account the initial amount of powder in the mould, its filling behavior, and the thermal expansion of the dies, graphite sheets, and mould [33]. To simplify this, the relative density shown in Fig. 3 only takes into account the initial powder amount in the mould being different in both experiments as less material could be loaded into the mould when pressing at 100 MPa. Therefore, the relative densities were calculated based on the relative piston travel displacement and the initial powder weight; the diameter remained a constant 20 mm. The effect of pressure and densification was studied in the form of a graph detailing the densification of the material during sintering. The graph in Fig. 3 clearly shows the influence of compaction pressure on the relative densification of the materials. Another important notice from Fig. 3 is that material densification occurs at approximately 1200 °C and of course accelerates faster for the 100 MPa compaction. As indicated in the graph, the higher compaction pressure increased the densification rate by as much as 5% at approximately 1300 °C. This is also the point where the sintering regime ramped very quickly to 300 °C*min^{-1} as shown in Fig. 1. The main reason to incorporate this sudden jump is that previous experiments have shown that Mo grain growth during SPS beings at approximately 1300 °C [29]. In order to prevent excessive grain growth, the decision was made to adjust the sintering regime as to have very fast ramping starting from 1300 °C to the end temperature.

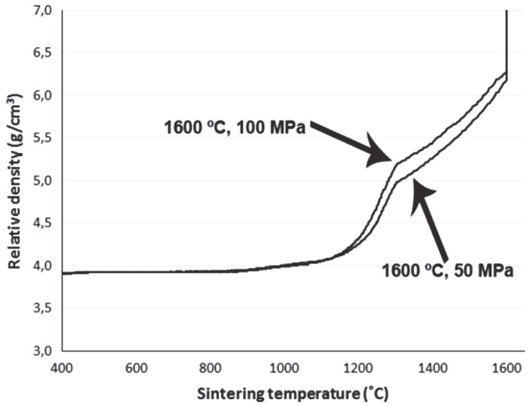

Fig. 3. Graph showing the relative density over temperature calculated from the relative piston travel during sintering. Both samples approach full densification at 1600 °C.

3.2. XRD analysis

X-ray diffraction analysis was performed on each ZrC-20 wt% Mo composites at the various sintering temperatures and pressures. In all samples tested except the one sintered at 2100 °C, ZrC was detected as (Zr, Mo)C regardless of the applied pressure. There is a nominal trend in the intensity of Mo with increasing temperature as seen in Fig. 4. The black arrows focus particular attention to the intensity of Mo, which can be a general indication of the concentration of Mo in the sample. In all instances, raising the sintering temperature from 1600 to 2100 °C saw a progressive decrease in Mo intensity, probably due to more Mo dissolution into ZrC. This decrease in Mo content with increasing sintering temperatures is reflected in the decreasing densities of the samples seen in Fig. 2. Unlike previous studies [10,13,14], only the sample sintered at 2100 °C gave a very faint Mo_2C signal as seen in Fig. 4. Of particular note was the processing of the composite surface after SPS, including diamond grinding and polishing.

If there was any Mo carburisation during sintering, the depths of penetration into the composite would be at most 200 μm [29] making any traces removed during post sintering processing. Of course, the other main reason why Mo_2C was only faintly detected has to do with the intrinsic nature of SPS technology: the short sintering time and fast ramp rates. It is also important to note that 2100 °C is also a threshold temperature for Mo phase boundary where Mo_2C no longer forms, but instead reverts back into Mo [10]. Of course, the rapid cooling that proceeds a SPS experiment

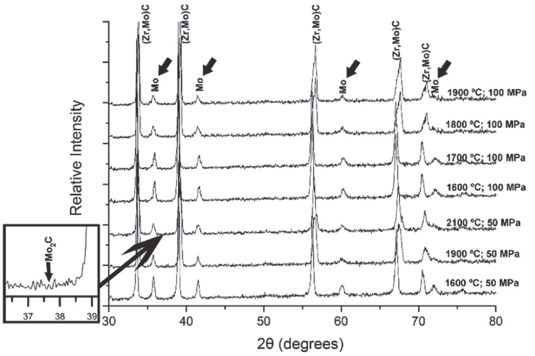

Fig. 4. XRD spectra for ZrC-Mo at various SPS temperatures and two compaction pressures. Black arrows indicate the intensity of Mo with different sintering temperatures. Side image shows faint Mo_2C detected at high SPS temperatures.

Table 1
Lattice parameters of ZrC and the corresponding amount detectable of Mo based on XRD.

Composite	Lattice parameter (Å)	Relative [Mo] vol%
1600 °C_50 MPa	4.640	16.2
1900 °C_50 MPa	4.614	10.2
2100 °C_50 MPa	4.579	11.4
1600 °C_100 MPa	4.632	16.0
1700 °C_100 MPa	4.630	15.4
1800 °C_100 MPa	4.624	11.6
1900 °C_100 MPa	4.604	9.3

also means there is little time for all Mo_2C to disappear. Nevertheless, the 5 min dwell time at 2100 °C was significant enough to allow the percentage of surface Mo to reach 11.4% in Table 1.

The XRD analysis show the ZrC peaks were found to shift to a higher 2θ values as compared to their normal stoichiometric compound. As seen in Fig. 4 with the subtle, obvious shifting in ZrC peaks and tabulated in Table 1, the lattice parameter values of ZrC slowly decreases with increasing SPS temperature. In work by Landwehr et al. [10,14], they state that ZrC higher 2θ values indicate Mo dissolution into ZrC. This was accompany with an increase in solid solution Mo with increasing Mo content up to 40 vol% Mo in the ZrC-Mo composition. In this study and based on the XRD analysis, the relative surface Mo content decreases as sintering temperature goes higher. This could be attributed to the formation of Mo_2C through carburisation, which was subsequently removed during sample grinding and polishing. There is one exception to this trend with the sample at 2100 °C where the decreasing intensity of Mo reverses due to Mo phase boundary. Most likely though, the decrease in relative Mo content is due to the dissolution of Mo into ZrC as indicated by the lattice parameter reduction of ZrC. There is no detectable stoichiometric ZrC in microstructure. This would support why the XRD consistently showed the existence of (Zr, Mo)C mix carbide.

3.3. Mechanical properties

When it comes to cermets or cemented carbides, the prime mechanical properties prioritised has been Vickers hardness and fracture toughness – where the balance of these two parameters usually skew towards having the highest fracture toughness possible. The detail values for hardness, fracture toughness, Young moduli, relative densities are tabulated in Table 2.

Assembling the hardness and fracture toughness into a single graph, Fig. 5(A), it clearly shows that Vickers' hardness increases with increasing sintering temperature. Using a compaction pressure of 50 MPa was much more effective at producing a more viable material as also indicated by the fracture toughness increasing with rising temperature. Temperature has the greatest beneficial impact on the mechanical properties for samples sintered at 50 MPa, yet comparing Figs. 2 and 5(A) and (B), there would seem to be a disconnect with dropping relative density and an increase in hardness and Young's modulus. This is due to the decrease in Mo intensity as shown in XRD scans of Fig. 4 and thus leading to less volumetric Mo in the solid solution and therefore the high mechanical properties of hardness and Young's modulus become more reflective of ZrC. At 2100 °C and 50 MPa, the values are 2231 HV10 and 5.4 MPa*m$^{1/2}$ along with the highest value for Young modulus at 396 GPa. However, increase compaction pressure 100 MPa along with increasing temperature has a clearly detrimental effect on overall mechanical properties as both fracture toughness and elastic modulus drop by as much 25% on average between 1600 and 1900 °C. Fig. 5(B) shows the steady drop in Young's modulus values with increasing temperature under 100 MPa compaction pressure; the opposite is true for using 50 MPa pressure, where the Young's modulus increases.

Table 2
Relative density and mechanical properties of the composites.

Composite Sintering	Relative density [%]	Hardness [HV_{10}]	K_{IC} [MPa*m$^{1/2}$]	Young Modulus [GPa]
1600 °C_50 MPa	97.7	2139 ± 20	5.1 ± 0.5	300 ± 23
1900 °C_50 MPa	97.7	2174 ± 18	5.5 ± 0.6	346 ± 16
2100 °C_50 MPa	97.4	2231 ± 14	5.4 ± 0.6	396 ± 14
1600 °C_100 MPa	98.7	2051 ± 54	5.4 ± 0.6	374 ± 30
1700 °C_100 MPa	98.5	2065 ± 33	4.2 ± 0.6	353 ± 15
1800 °C_100 MPa	98.3	2157 ± 50	4.2 ± 0.6	294 ± 28
1900 °C_100 MPa	98.3	2139 ± 51	3.9 ± 0.6	291 ± 21

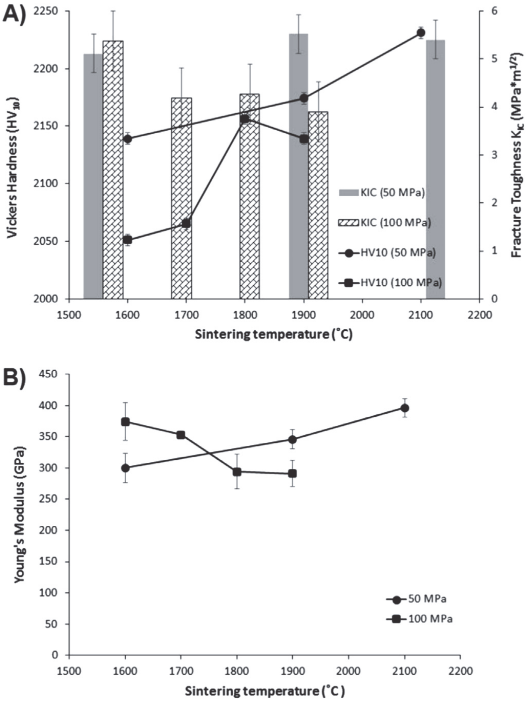

Fig. 5. A) mechanical properties of Vickers' hardness and fracture toughness and B) elastic Young's modulus for all samples separated by compaction pressures.

When comparing the mechanical results from this study to previous research done on ZrC-Mo, the field of study is limited given the novelty of our research. Landwehr et al.'s [14] used base values measured using a composition of ZrC-20vol%Mo, which had a hardness of ~1700 HV_1, toughness 2.5 MPa*m$^{1/2}$, and Young modulus ~375 GPa. They had the mindset to model their hardness values after a pair of WC-Co cermet models, where the hardness values were determined empirically based on Hall-Petch behavior [34,35]. Fracture toughness and Young modulus were extrapolated from various studies into a linear correlation with increasing vol% Mo in a volumetric rule of mixtures graph [36,37]. According to this theory, a typical ZrC-14 vol%Mo composite, as is the case of this study, should give the following estimated properties: 1800 HV, 3.0 MPa*m$^{1/2}$, and 375 GPa Young's modulus. The SPS sample in this study gave a high value of 2231 HV10 and 5.4 MPa*m$^{1/2}$, and 396 GPa Young's modulus at 2100 °C, 50 MPa. Of course, using models rather than direct comparisons of composites has

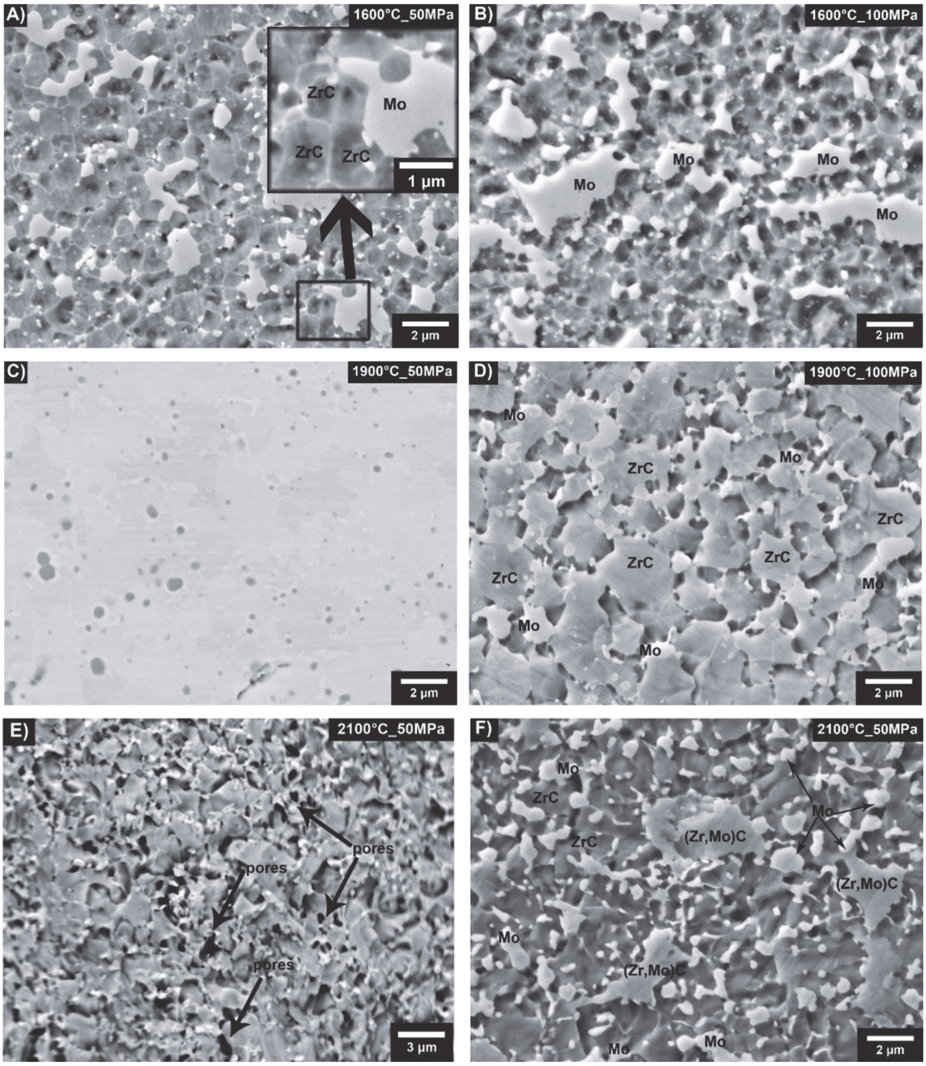

Fig. 6. SEM micrograph of ZrC-20 wt%Mo SPSed at various indicated temperatures and compaction pressures. Mo is the lighter phase and ZrC is the darker phase. C) is the only sample not acid etched to show no surface porosity. Black arrows on E) show microscopic pores in an unpolished, cross section. The sample was acid etched for only 5 s

particular flaws: the issue of porosity, the method of measurement, and the actual number of phases are not fully taken into account. The hardness in this study was taken as macrohardness (HV_{10}) and fracture toughness calculated from Palmqvist values by Vickers' indentation thus possibly giving a lower, yet more conservative value. As for phase and porosity, they are discussed in the next section.

3.4. Microstructure

The microstructure of some of the SPSed ZrC-Mo samples characterised by surface SEM after acid etching are shown in Fig. 6. Etching with strong acids, particularly hydrogen fluoride was necessary to reveal any kind of surface morphology from the SEM images. The etching was limited to only 10 s since any longer caused an adverse reaction, which severely tarnished the surface. Fig. 6(C), sintered at 1900 °C, 50 MPa, is the only sample examined by SEM, but not having acid etching to show no discernable porosity, at least on the surface. Of course, this is no proof the sample achieved 100% densification. Based on relative densities calculated from theoretical density (Table 2), coupled with the XRD theoretical quantities of surface Mo phase (Table 1), the amount of porosity could be estimated to be 1–2.3% for all samples depending on the sintering temperature and compaction pressure. This level is in agreement with the supposed porosity for ZrC-Mo sintered via hot pressed [14]. An unpolished cross section was examined in Fig. 6 (E), where even at the highest sintering temperature (2100 °C) and moderate compaction pressures (50 MPa), there exist microscopic pores. This is also the sample with the lowest relative density value.

In Fig. 6 A and B, the microstructures have very similar resemblance: Mo is dispersed across the surface existing as clusters with several larger, white globs. Looking closely at Fig. 6(A), the microstructure reveals ZrC grain boundaries with the individual grains being 1–2 μm in size on average. The starting ZrC powder is 3.6 μm, which leads to the conclusion that ZrC grain growth was minimal during densification. The smaller grain size could be attributed to the ball milling leading to a subsequent refinement of the particles. It is, however, unclear whether the Mo phase form interconnected phases in-between the ZrC grains. The grain boundaries in the SEM seem sufficiently bright to suggest ZrC-Mo formed a two phase, interpenetrating microstructure, typical of liquid phase sintering via HIP [10,13,14]. Conversely, looking at Fig. 6(D), the combination of high compaction pressure and seemingly threshold high temperature for ZrC-Mo causes extensive grain growth across the microstructure. This is certainly supported by the poor mechanical properties for a sample sintered at 1900 °C, 100 MPa, where fracture toughness and Young's modulus drop to 3.9 MPa*m$^{1/2}$, and 291 GPa respectively. SEM for 1700 and 1800 °C, 100 MPa possessed increasing ZrC grain growth, which is also back up by their falling fracture toughness and Young's modulus values.

It is surprising that the only sample to exhibit any detectable Mo_2C phase via XRD is also herald as to possess the best mechanical properties for hardness, toughness, and Young's modulus. Fig. 6(F) shows the surface of the ZrC-Mo composite sintered at the highest SPS temperature 2100 °C, 50 MPa showing smaller bright, white globs of Mo phases on a grey ZrC phase background. The phases that appear lifted are probably the (Zr, Mo)C solid solution mixed carbides. Looking back at the XRD analysis, Fig. 4 and lattice parameter of Table 1, both the decreasing Mo intensity and the decreasing lattice parameter of ZrC suggest a change on the surface volume of Mo depending on sintering conditions. Judging from the SEM images, Fig. 6(F) has a more uniform dispersion of Mo phase and smaller clusters of Mo compared to Fig. 6 A or B. explain why ZrC-Mo sintered at 2100 °C, 50 MPa possesses superior mechanical properties compared to all other samples. The critical flaw size analysis was performed by Landwehr et al. [14] suggested Mo cluster sizes are the critical flaw in ZrC-Mo and that the smaller sizes would lead to better fracture toughness. Hence, this could explain why ZrC-Mo sintered at 2100 °C, 50 MPa possesses superior mechanical properties compared to all other samples.

4. Conclusions

ZrC-20 wt%Mo composite was spark plasma sintered at various temperatures at either 50 or 100 MPa compaction pressure. Increase in processing temperature causes relative density to fall for the composite, but doubling the compaction pressure increases the overall pressure by 1%. Higher compaction pressure was shown to increase the densification rate of the sample at the same temperature. XRD analysis demonstrates that the materials have (Zr, Mo)C and Mo peaks, while only at a sintering temperature of 2100 °C was Mo_2C detectable. The lattice parameter of ZrC decreases with increasing sintering temperature, shifting ZrC peaks to higher 2θ, thus suggesting further Mo dissolution into ZrC. SEM images showed that at the highest SPS temperature, 2100 °C and 50 MPa, small clusters of Mo phases are presented resulting in higher indentation fracture toughness of the composite. In fact, this particular sintering regime gave the most optimal mechanical values: 2231 HV10 and 5.4 MPa*m$^{1/2}$, and 396 GPa Young's modulus. The compaction pressure of SPS played a pivotal role for the composite properties. Moderate 50 MPa pressure caused hardness, fracture toughness, and Young modulus to increase with increasing temperature. Conversely, a higher 100 MPa pressure caused fracture toughness, and Young modulus to decrease with increasing sintering temperature.

Acknowledgments

This work was supported by the Estonian Research Council under PUT1063 (I. Hussainova) and the Institutional Research Funding IUT 19-29 of the Estonian Ministry of Education and Research. The author would also like to thank technicians Rainer Traksmaa for XRD analysis and Mart Viljus for SEM imaging.

References

[1] H.O. Pierson, Handbook of Refractory Carbides and Nitrides, William Andres Publishing/Noyes., Westwood, NJ, 1996.

[2] D. Cédat, C. Rey, M. Clavel, J. Schmitt, M. Le Flem, A. Allemand, Microstructural characterization of a composite Mo reinforced by 25 at% TiC, J. Nucl. Mater. 385 (3) (2009) 533–537.

[3] G. Filacchioni, E. Casagrande, U. De Angelis, G. De Santis, D. Ferrara, Effect of strain rate on tensile properties of TZM and Mo-5%Re, J. Nucl. Mater. 307 (311) (2002) 705–709.

[4] S.E. Landwehr, G.E. Hilmas, W.G. Fahrenholtz, I.G. Talmy, H. Wang, Thermal properties and thermal shock resistance of liquid phase sintered ZrC–Mo cermets, Mater. Chem. Phys. 115 (2–3) (2009) 690–695.

[5] M. Le Flem, A. Allemand, S. Urvoy, D. Cédat, C. Rey, Microstructure and thermal conductivity of Mo–TiC cermets processed by hot isostatic pressing, J. Nucl. Mater. 380 (1–3) (2008) 85–92.

[6] M. Umalas, I. Hussainova, V. Reedo, D.-L. Young, E. Cura, S.-P. Hannula, R. Lõhmus, A. Lõhmus, Combined sol–gel and carbothermal synthesis of ZrC–TiC powders for composites, Mater. Chem. Phys. 153 (2015) 301–306.

[7] Y. Li, H. Katsui, T. Goto, Effect of heat treatment on the decomposition of TiC–ZrC solid solutions by spark plasma sintering, J. Eur. Ceram. Soc. (2016).

[8] S. Pellegrino, L. Thomé, A. Debelle, S. Miro, P. Trocellier, Radiation effects in carbides: TiC and ZrC versus SiC, Nucl. Instrum. Methods Phys. Res. Sect. B: Beam Interact. Mater. At. 327 (2014) 103–107.

[9] I. Hussainova, N. Voltšihhin, E. Cura, S.-P. Hannula, Densification and characterization of spark plasma sintered ZrC–ZrO_2 composites, Mater. Sci. Eng.: A 597 (2014) 75–81.

[10] S.E. Landwehr, G.E. Hilmas, W.G. Fahrenholtz, I.G. Talmy, Processing of ZrC-Mo cermets for high-temperature applications, part i: chemical interactions in the ZrC-Mo system, J. Am. Ceram. Soc. 90 (7) (2007) 1998–2002.

[11] P. Barnier, C. Brodhag, F. Thevenot, Hot-pressing kinetics of zirconium carbide, J. Mater. Sci. 21 (1986) 2547–2552.

[12] D.L. Yung, L. Kollo, I. Hussainova, A. Žikin, Reactive Sintering of ZrC-TiC Composites, Key Eng. Mater. 527 (2012) 20–25.

[13] S.E. Landwehr, G.E. Hilmas, W.G. Fahrenholtz, I.G. Talmy, Processing of ZrC–Mo Cermets for High Temperature Applications, Part II: Pressureless Sintering and Mechanical Properties, J. Am. Ceram. Soc. 91 (3) (2008) 873–878.

[14] S.E. Landwehr, G.E. Hilmas, W.G. Fahrenholtz, I.G. Talmy, S.G. DiPietro, Microstructure and mechanical characterization of ZrC–Mo cermets produced by hot isostatic pressing, Mater. Sci. Eng.: A 497 (1–2) (2008) 79–86.

[15] T. Takida, M. Mabuchi, M. Nakamura, T. Igarashi, Y. Doi, T. Nagae, Mechanical properties of a ZrC-dispersed Mo alloy processed by mechanical alloying and spark plasma sintering, Mater. Sci. Eng.: A 276 (2000) 269–272.

[16] D. Yung, I. Hussainova, M. Rodriguez, R. Traksmaa, Processing of ZrC-TiC composites by SPS, Key Eng. Mater. 674 (2016) 94–99.

[17] X. Zhang, N. Liu, Effects of ZrC on microstructure, mechanical properties and thermal shock resistance of TiC–ZrC–CO–Ni cermets, Mater. Sci. Eng.: A. 561 (2013) 270–276.

[18] Y. Li, H. Katsui, T. Goto, Spark plasma sintering of TiC–ZrC composites, Ceram. Int. 41 (5) (2015) 7103–7108.

[19] S. Liu, W. Hu, J. Xiang, F. Wen, B. Xu, D. Yu, J. He, Y. Tian, Z. Liu, Mechanical properties of nanocrystalline TiC–ZrC solid solutions fabricated by spark plasma sintering, Ceram. Int. 40 (7) (2014) 10517–10522.

[20] A. Teber, F. Schoenstein, F. Têtard, M. Abdellaoui, N. Jouini, The effect of Ti substitution by Zr on the microstructure and mechanical properties of the cermet Ti1-xZrxC sintered by SPS, Int. J. Refract. Met. Hard Mater. 31 (2012) 132–137.

[21] N. Nomura, T. Suzuki, S. Nakatani, K. Yoshimi, S. Hanada, Joining of oxidation-resistant Mo-Si-B multiphase alloy to heat-resistant Mo-ZrC in-situ composite, Intermetallic 11 (2003) 51–56.

[22] T. Suzuki, H. Matsumoto, N. Nomura, S. Hanada, Microstructures and fracture toughness of directionally solidified Mo-ZrC eutectic composites, Sci. Technol. Adv. Mater. 3 (2002) 137–143.

[23] D. Sivaprahasam, S.B. Chandrasekar, R. Sundaresan, Microstructure and mechanical properties of nanocrystalline WC–12Co consolidated by spark plasma sintering, Int. J. Refract. Met. Hard Mater. 25 (2) (2007) 144–152.

[24] C.B. Wei, X.Y. Song, J. Fu, X.M. Liu, Y. Gao, H.B. Wang, S.X. Zhao, Microstructure

and properties of ultrafine cemented carbides—differences in spark plasma sintering and sinter-HIP, Mater. Sci. Eng.: A. 552 (2012) 427–433.
[25] S. Zhao, X. Song, C. Wei, L. Zhang, X. Liu, J. Zhang, Effects of WC particle size on densification and properties of spark plasma sintered WC–Co cermet, Int. J. Refract. Met. Hard Mater. 27 (6) (2009) 1014–1018.
[26] D. Yung, N. Voltsihhin, I. Hussainova, L. Kollo and R. Traksmaa. Sintering of Zirconium carbide-based composites. in Euro PM2012. Basal, Switzerland: EUROPM, 2012.
[27] F. Sergejev, M. Antonov, Comparative study on indentation fracture toughness measurements of cemented carbides, Proc. Est. Acad. 12 (4) (2006) 388–398.
[28] W. Oliver, G. Pharr, An improved technique for determining hardness and elastic modulus using load and displacement sensing indentation experiments, J. Mater. Res. 7 (6) (1992) 1564–1583.
[29] R. Ohser-Wiedemann, U. Martin, H.J. Seifert, A. Müller, Densification behaviour of pure molybdenum powder by spark plasma sintering, Int. J. Refract. Met. Hard Mater. 28 (4) (2010) 550–557.
[30] A. Kapylou, V. Urbanovich, R. Andrievski, D. Kuznetsov, A. Nohrin, P. Klimczyk, Effect of compacting pressure, powder degassing and thermobaric treatment on densification and properties of nanocrystalline titanium nitride, Process. Appl. Ceram. 3 (3) (2009) 161–166.
[31] P. Barick, D. Chakravarty, B.P. Saha, R. Mitra, S.V. Joshi, Effect of pressure and temperature on densification, microstructure and mechanical properties of spark plasma sintered silicon carbide processed with β-silicon carbide nano-powder and sintering additives, Ceram. Int. 42 (3) (2016) 3836–3848.
[32] P. Garg, S.-J. Park, R.M. German, Effect of die compaction pressure on densification behavior of molybdenum powders, Int. J. Refract. Met. Hard Mater. 25 (1) (2007) 16–24.
[33] U. Anselmi-Tamburini, J.E. Garay, Z.A. Munir, Fundamental investigations on the spark plasma sintering/synthesis process, Mater. Sci. Eng.: A 407 (1–2) (2005) 24–30.
[34] H. Lee, J. Gurland, Hardness and deformation of cemented tungsten carbide, Mater. Sci. Eng. 33 (1) (1978) 125–133.
[35] H. Engqvist, S. Jacobson, N. Axén, A model for the hardness of cemented carbides, Wear 252 (2002) 384–393.
[36] B.V. Cockeram, The mechanical properties and fracture mechanisms of wrought low carbon arc cast (LCAC), molybdenum–0.5pct titanium–0.1pct zirconium (TZM), and oxide dispersion strengthened (ODS) molybdenum flat products, Mater. Sci. Eng.: A 418 (1–2) (2006) 120–136.
[37] Z. Fan, P. Tsakiropoulos, A.P. Miodownik, Prediction of Young's modulus of particulate two phase composites, Mater. Sci. Technol. 8 (10) (1992) 922–929.

Paper III: **Yung DL**, Antonov M, Veinthal R, Hussainova I. Wear behaviour of doped WC-Ni based hardmetals tested by four methods. *Wear*. (2016) 352-353, 171−179, DOI: dx.doi.org/10.1016/j.wear.2016.02.015

Wear 352-353 (2016) 171–179

Contents lists available at ScienceDirect

Wear

journal homepage: www.elsevier.com/locate/wear

Wear behaviour of doped WC–NI based hardmetals tested by four methods

Der-Liang Yung, Maksim Antonov, Renno Veinthal, Irina Hussainova*

Department of Materials Engineering, Tallinn University of Technology, Ehitajate 5, 19086 Tallinn, Estonia

ARTICLE INFO

Article history:
Received 21 September 2015
Received in revised form
11 February 2016
Accepted 12 February 2016
Available online 27 February 2016

Keywords:
Cemented carbides
Abrasive wear
Erosive wear
Slurry erosion
Titanium carbide
Zirconium carbide

ABSTRACT

Cemented tungsten carbide systems have been widely used in machine tools, ammunition rounds, and sporting equipment, as they possess the necessary combination of hardness and toughness to endure wear environments. In most applications, the abrasion phenomena has been identified as one of the sources of surface damage and material degradation. In this work, WC–Ni hardmetal is doped with zirconium carbide or titanium carbide to improve its abrasive and erosive wear resistance. TiC has been known to produce platelet grain structure meant for strengthening leading to enhanced abrasion resistance. ZrC can suppress grain coarsening and abnormal growth of WC grains while increasing hardness. Tribological characteristics are obtained from slurry and dry erosion, as well as high and low stress abrasion tests. The composite of WC–8Ni–TiC works best overall for various wear conditions with exception of high stress abrasion. WC–8Ni–ZrC does not provide any benefit of wear resistance in this study. Wear rate and mechanisms of wear were analysed by and discussed based on scanning electron microscopy studies.

1. Introduction

Since its initial invention in 1923, cemented tungsten carbide (WC) systems have been widely used as a viable replacement to common steel as tool bits in geo-engineering for rock drilling, mineral cutting, gas and oil drilling, and tunnelling projects [1]. For the purposes of large-scale earth excavation, using tunnel boring machines (TBMs) fitted with WC-based hardmetal dragbits is a well-established and popular engineering feat to excavate tunnels usually for modern, underground train networks [2]. Cemented carbide tools possess a finite lifespan depending on the excavation's ground abrasivity and subsequent wear of the tool [3]. Research to extend the lifespan of tools focuses on achieving predictability on the wear of the tools [1,3–5]. Industrially, this information is valuable to the initial direct manufacturing cost of tools, to the efforts to reduce TBM downtime, and above all, to minimise delays to the project. For soft ground tunnelling, the tools and dragbits are subjected to hyperbaric working environment, and as such, any replacement or repair work becomes a diver operation [2]. Having tools with enhanced lifespan can mitigate the risk to workers needed to make tool replacement operations as the number of instances for tool replacement is reduced.

The WC-based cemented carbides have proven to possess the combination of hardness and fracture toughness meant to endure wear; however, it has also been shown that wear resistance values are not always correlated with high mechanical properties [4–6]. Doping hardmetals with oxides or carbides can alter the grain structure in the WC-based hardmetals leading to different wear characteristics. Decades of research have determined that varying the amount of carbide to metallic binder ratio greatly affects the mechanical properties of the cemented carbide. Adding more binder typically yields a material with higher ductility and toughness, whereas less binder content yields higher values for hardness and better wear resistance [7]. Using additives, such as zirconia (ZrO_2) to dope cemented carbides, exploits the mechanism of stress induced transformation of tetragonal zirconia into monoclinic polymorphs. The replacement of the carbides with small amounts of yttria stabilised zirconia suppresses the formation of truncated triangular prism shaped WC grains and results in WC grain refinement [8–10]. The martensitic transformation, with increase in volume of zirconia particle, allows volume flux under loading, resulting in crack closures. Therefore, this leads to an increase in material resistance to crack propagation. The final result is an increase in fracture toughness of doped materials, while maintaining similar hardness parameters [11]. Furthermore, ZrO_2 has been shown to improve the wear and abrasive resistance of WC cemented carbides by inhibiting transgranular crack propagation through the microstructure since wear is generated from brittle fracture of carbides and removal of WC grains [9].

Vanadium and chromium carbide (VC and Cr_3C_2) have already been well documented [12–14] for their grain growth inhibitor ability and enhancements to wear properties. During a typical pin

---

* Corresponding author.
E-mail address: irina.hussainova@ttu.ee (I. Hussainova).

http://dx.doi.org/10.1016/j.wear.2016.02.015

on disc test, wear would start at the binder phase by a combination of plastic deformation and/or micro-abrasion, which in turn facilitates the removal of WC grains. The addition of grain growth inhibitors significantly reduces the coefficient of friction value and limits the increase of this parameter even under increasing contact loads [13]. The increase in hardness due to VC and Cr_3C_2 is attributed to the microabrasion resistance as a result of reduced grain size in the microstructure [12]. Given the research into VC and Cr_3C_2, other carbides such as titanium carbide (TiC) or zirconium carbide (ZrC) have received less attention. TiC has been known to increase the hardness and strength of cemented carbides by changing the shape of the WC grain into flatter triangular prisms with lower values of shape equiaxiality [15]. These flatter shaped WC grains are able to decrease the number of inter-crystalline fracture along the carbide-carbide interfaces, and thereby, in theory, improve wear resistance concurrently [16]. Given the similar shape and characteristics of ZrC to TiC, added fraction of ZrC nano-powder can increase the hardness and fracture toughness of WC [17]. ZrC has been seen to segregate to the WC grain boundaries and thus refine and inhibit grain growth in WC–Co systems [18].

In this work, WC–Ni hardmetal was doped with zirconium carbide or titanium carbide and the subsequent composite is examined under four different methods of wear conditions. The selection of binder element into our WC system would naturally rest with the default choices of either nickel (Ni), or traditionally, cobalt (Co). Cobalt has a relatively high compatibility with WC, particularly the strong interfacial bonding with the carbide leading to the desired combination of hard reinforcement within a ductile matrix [19]. However, nickel has been shown to be more ductile than cobalt, which can reduce loss of WC grains during erosion of binder phase [3]. Tribological testing included high-stress abrasion tests where two working surfaces rub together with sufficient force to crush granular abrasive materials; and low-stress wear where the abrasive material is able to slide freely over a surface in sliding wear conditions. These were represented in the laboratory by using high-stress abrasion sand paper testing and low-stress abrasion. Dry and wet erosion tests were also conducted as these tests impart the particular characteristics of TBM drilling when lubricant fluids are injected between the cutter heads and excavated ground.

Table 1
Composition of materials.

Material grade	wt%			
	WC	Ni	TiC	ZrC
WNO	92.0	8	–	–
WNT	91.0	8	1	–
WNZr	90.7	8	–	1.3

2. Materials and methods

2.1. Sample preparation

Cemented WC–8 wt%Ni composites doped with two different additives were made using powder metallurgical methods. Commercial powders WC (100 nm, H.C. Starck, 99%), Ni (0.3 µm, K10, 99%), along with additive carbides TiC (40 nm, Sigma-Aldrich, 99%), and ZrC (40 nm, H.C. Starck, 99%) were used to make the composites. The volumetric content of additives (TiC, ZrC) was kept at 0.2 vol%, or 1.0 wt% and 1.3 wt% respectively. The powders were mixed under ball milling conditions (WC–Co containers and

Table 2
Overview of abrasive wear test methods applied with increasing stress of each test.

Increasing test stress

Test method	**Slurry erosion**	**Low stress abrasion with rubber wheel**	**Dry erosion**	**High stress abrasion**
Scheme		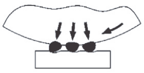		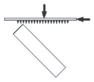
Shape of particles	Angular	Rounded	Rounded	Angular
Size of particles	Fine	Large	Large	Medium
Hardness of particles	HV 1100 (SiO_2)	HV 1100 (SiO_2)	HV 1100 (SiO_2)	HV 2500 (SiC)
Impact	Yes	No	Yes	No
Stress	Low	Low	Medium	High

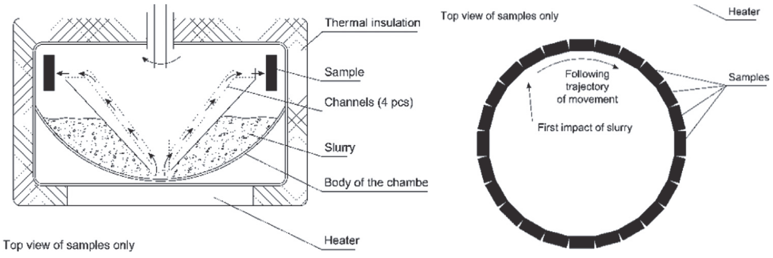

Fig. 1. Schematic of the side (above) and top view (below) of the slurry testing device [22].

balls, 12:1 wt% ball to powder ratio, ethanol milling liquid, 48 h milling time). Powders were mixed with 1 wt% organic paraffin and pressed at 45 MPa into green samples. Pre-sintering was done under flowing H_2 at 500 °C to for 1 h. Samples underwent sinter hot isostatic pressing (sinter-HIP) at 1450 °C (10 °C min^{-1} to 1200 °C, dwell 30 min, then 10 °C min^{-1} to the final temperature for 30 min, split between vacuum, followed by 30 MPa argon pressure). Sample designation and composition of the cemented carbides created and studied are shown in Table 1.

2.2. Characterisation and testing

Basic mechanical properties were evaluated including hardness (HV30) and fracture toughness by indentation using the equation outlined by the Palmqvist crack system [20]. The mean grain size of WC and mean free path for Ni binder were determined according to intercept method [21]. Sintered samples were ground using a diamond polish to 0.5 μm before undergoing wear testing. Four different abrasive wear test methods were applied for testing of developed materials as displayed in Table 2. All the tests were performed at room temperature. The weight loss of samples was measured to the nearest 0.1 mg using GR-202 balance (A&D Instruments). Tests were repeated at least 3 times and average values recorded.

2.3. Slurry erosion

Fig. 1 shows the schematic of the slurry test device. The slurry is accelerated by centrifugal force from the bottom of the pot via pipes and impacts the samples [22]. Slurry erosion was conducted at a velocity of 20.1 m s^{-1} using a slurry mixture of 2 kg water to 0.4 kg of silica abrasive with mean size of 54 μm (N4 grade from *Sibelco*) for a duration of 12 h. The silica abrasive of such size form stable suspension even with low intensity of agitation and particles are equispaced within the volume of the liquid. Fresh abrasive was used for every test. The same abrasive was circulating inside the device during the whole test. The weight loss of samples was measured and converted into volumetric wear loss (mm^3) by applying the density of material.

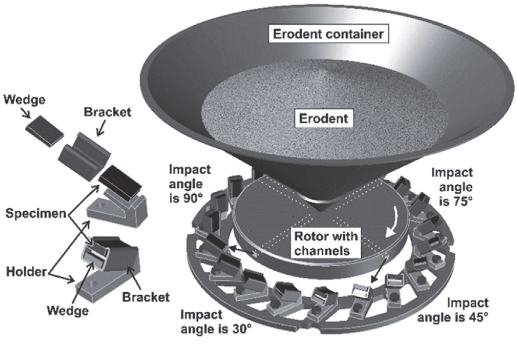

Fig. 2. Centrifugal erosion accelerator according to GOST 23.201–78.

2.4. Dry erosion

Four-channel centrifugal accelerator working according to GOST 23.201–78 described elsewhere [23] was used for the dry erosion test seen in Fig. 2. The impact angle was 30°; particle impact velocity was 50 m s^{-1}; 15 kg of silica sand with 0.1–0.4 mm particle size were used. The mass flux of erodent particles that impact the target ($M1$ [kg]) is defined in relation to the angle under which the jet of erodent particles is attacking the sample, δ, and the total mass of erodent particles that is used for the test (M [kg]):

$$M1 = M\frac{\delta}{360} \tag{1}$$

For the rotor diameter of 0.2 m and the width of exposed area of 12 mm, the δ angle is calculated to be 8.5°. The weight loss of samples was measured and converted into volumetric wear loss (mm^3) by applying the density of material. The erosion rate was determined as volume loss of the target sample per mass of erodent particles striking the sample (I_v, $\text{mm}^3\ \text{kg}^{-1}$) using the following equation:

$$Iv = \frac{\Delta m}{M1 \cdot \rho} \tag{2}$$

where Δm is the mass loss (mg) and ρ is density of the sample under consideration. The volumetric erosion rate is used to compare materials due to their different density values.

2.5. High stress abrasion

The prismatic rectangular and cylindrical pins (according to ASTM G132-95) or balls are used for conformal and non-conformal abrasive tests against sand paper [24]. Due to the high wear resistance of the

Table 3
Mechanical properties of materials.

Material grade	WC grain size (μm)	MFP (μm)	Relative density (%)	Hardness (HV30)	K_{IC} ($\text{MPa m}^{1/2}$)
WNO	0.88	0.17	97.4	1296 ± 8	13.5 ± 1.4
WNT	0.94	0.26	96.4	1343 ± 14	11.8 ± 1.2
WNZr	0.48	0.15	99.2	1618 ± 8	10.7 ± 1.4

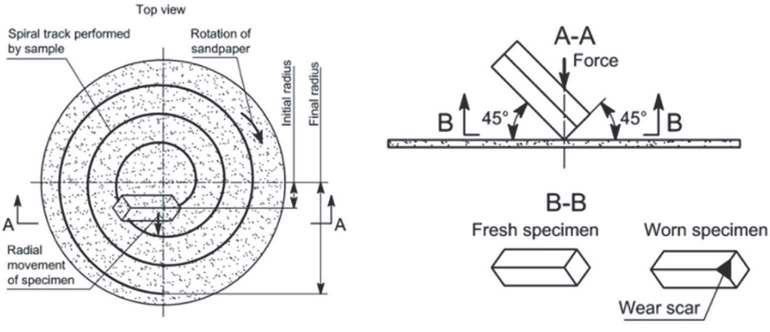

Fig. 3. High stress abrasion test setup.

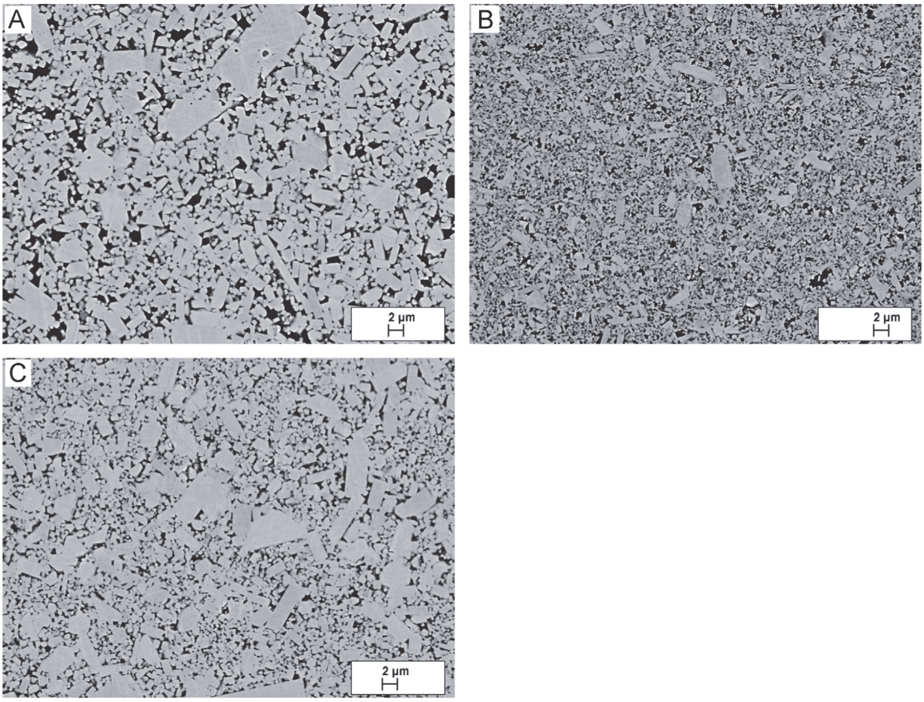

Fig. 4. SEM image of (A) WNT, (B) WNZr, and (C) WNO.

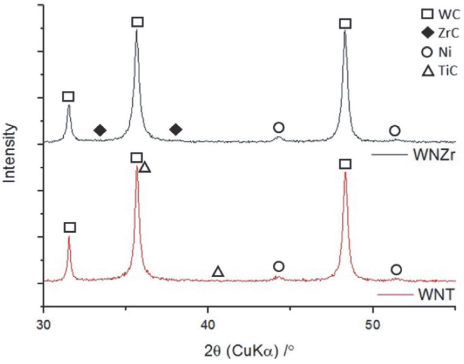

Fig. 5. XRD patterns of WNT (bottom) and WNZr (top).

test materials, it was decided to apply non-conformal test when the corner of the rectangular prismatic specimen is pressed against the rotating disc covered by P180 (82 μm) SiC abrasive paper from *Buehler*, Fig. 3. The CETR/Bruker UMT-2 tribometer with servo-controlled loading was used for testing. The sample's corner was diamond ground to provide a uniform rectangular corner.

The load was 0.5 N; linear abrasion (distance) was 135.7 m; initial radius was 5 mm; final radius was 55 mm; and the duration of test was 1 h. The tests were done at room temperature. Rotational speed was kept at constant level (12 min^{-1}). The average velocity was 0.038 m s^{-1}. The low velocity was required for servo controlled load adjustment during significant vertical displacement of the sharp corner in the beginning of the test. The fresh abrasive was continuously supplied into wear zone. Volume lost was evaluated by measuring the dimensions of the wear scar remaining after testing and by applying the equation for calculation of the volume of the triangular pyramid lost. An Optical microscope Discovery V20 SteREO equipped with AxioVision software from *Carl Zeiss* was used. Test results are reported as volume loss in cubic millimetres per load and distance ($\text{mm}^3\ \text{N}^{-1}\ \text{m}^{-1}$).

2.6. Low stress abrasion

Abrasive testing was performed using the rubber-rimmed rotary wheel machine according to the modified ASTM65-94 method with a reduced diameter of the wheel disk for testing small sized specimens and cutting down expenses during development stage of a new material [24]. The wheel diameter was 80 mm by breadth 8 mm. Ottawa silica sand with particle size 0.2–0.3 mm (AFS 50–70) and feeding rate 300 g min^{-1} was used as abrasive. Circumferential velocity was 2 m s^{-1}; linear abrasion was 1436 m. The load of 22.6 N with the wheel of given size ensures the same contact stress as experienced during the test with larger wheel of standard size (diameter 228.6 mm, breadth 12.7 mm) and load of 130 N. The weight loss of samples was measured and converted into volumetric wear loss (mm^3) by applying the density of material. Test results are reported as volume loss in cubic millimetres per load and distance ($\text{mm}^3\ \text{N}^{-1}\ \text{m}^{-1}$).

3. Results and discussions

3.1. Mechanical characteristics

The mechanical properties and the grain morphology, including mean free path (MFP) were measured as shown in Table 3. WC

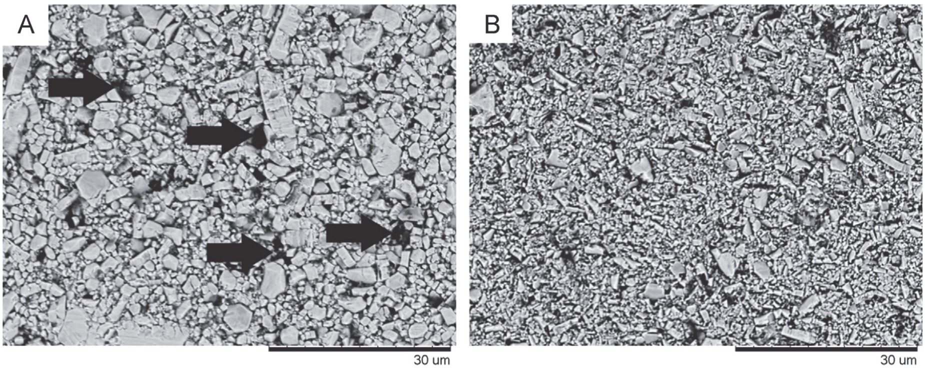

Fig. 6. SEM of slurry erosion samples: (A) WNO with lost carbide grains (black arrows) and (B) WNT.

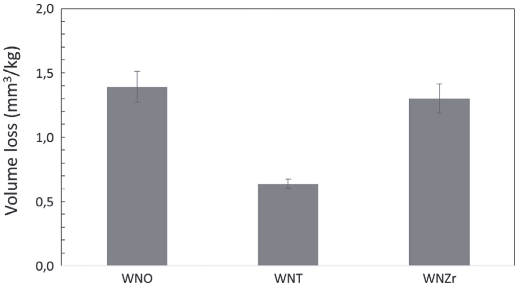

Fig. 7. Wear rate of materials under dry erosive conditions.

grain size in the material with TiC added was somewhat coarser as compared to the other samples, Fig. 4. Sample WNT is determined to have a higher hardness than the control WNO. It could be argued that the presence of 1 wt% of TiC in the binder phase might increase the in-situ hardness of the binder and thus the total hardness of the alloy. In fact, in WC–Co cemented carbides doped with TiC, the Ti segregates to the grain boundaries between the WC and Co phases [18]. However, given the small quantity of TiC, it is more likely the TiC influences the kinetics of WC grain growth. Doping WC-Ni with TiC has shown to transform WC crystals to a flatter triangular prism, thus increasing the hardness of cemented carbide by as much as 8–15% [15].

ZrC does a much better job as a grain growth inhibitor producing a fine grain microstructure with an average grain size half the size of the control WNO sample. This is also reflected in the mechanical properties with WNZr achieving a high hardness of HV30 1618 and near full relative density. The average grain size of WC grain doped with ZrC is only 0.48 μm compared with ~0.90 μm for either WNO or WNT samples as measured by the intercept method. Given the miniscule amount of TiC or ZrC, the carbide additive phases do not appear on SEM images; however, XRD analysis does indeed show, albeit minute, presence of respective carbides in the composite, Fig. 5. The peak of (W,Ti)C was not detected in the analysis, but the peaks of TiC and WC do overlap [25].

3.2. Slurry erosion vs dry erosion wear

To determine how the addition of TiC or ZrC affect WC-Ni during wear, four separate wear tests are conducted. In the case of slurry erosion, the water serves as a carrying media, as a lubricant, as a dampener that reduce the freedom of abrasive particle movement, as a corrosive substance, as coolant, and as a cleaning substance that can remove particles from fine cracks and cavities that are not accessible by abrasive particles. The particles of the abrasive used during the slurry test was SiO_2 with a hardness of HV 1100, much less than the bulk hardness any of the cemented carbides tested. The water should act like a lubricant causing the abrasives to slide rather than roll across the test surface. The largest mean free path with sample WNT is only 0.26 μm, which would put it in the realm of ultrafine size. Wear rate was expected to be negligible for all samples. However, because the fine abrasive particles possess sharp angles and due to the presence of water, the crushing of the abrasives during in-situ test has shown to escalate the aggressiveness of the abrasives [26]. The results for slurry erosion were the same for all samples (not shown) with an average of 0.28 mm^3/12 h volume wear. Although this wear value is significantly less compared to results with dry erosion, SEM images still show the formation of porosity due to carbide grain lost on the sample surface, Fig. 6.

Dry erosion test shows differentiation between samples with WNT exhibiting twofold less wear loss than either the control or WNZr, Fig. 7. WNT suffered only a 0.64 mm^3/kg compared to 1.30 or 1.39 mm^3/kg for WNZr and WNO respectively. During dry erosive wear testing, the samples are subjected to impact by large, abrasive particles at high speed. The impact angle of 30° invokes a cutting mode of wear on the materials. The extra impact energy on the surface of the microstructure causes both fracturing of coarser WC grains, but also embedded crushed abrasive in-between grains at the binder phase. Since WNT has a MFP twice that of the other two samples, the fine dust abrasive particles become embedded in-between the WC grains, stalling the continue wear of the surface. WNT is abled to outperform WNO and WNZr due to its larger MPF. WNO suffers from fracturing of the coarse WC grains as seen in Fig. 8A.

The higher hardness of sample WNZr should give higher wear resistance than WNT or WNO [12,13]; however, this is not the case. Given the binder content for all three samples stay constant, the main differential between WNZr and WNO is resulting WC grain size. Studies by Konyashin et al. [5,27,28] indicate the influence of binder content to average WC grain size ratio plays a key role in the wear resistance of WC cemented carbides even when all samples show similarly high hardness. Comparing coarse WC grains and fine-grain WC with the same binder content show the coarse grain composite to have higher wear resistance. Since there is a twofold WC grain size difference between WNZr and WNT, there is a higher proportion of soft binder phase on the surface of WNZr subjected to abrasive particle during performance testing leading to greater wear. WNZr fine grain microstructure, a material with moderate metallic binder, moderate hardness, and high fracture toughness are found to have an extremely low wear-resistance compared to standard coarse and ultra-coarse-grained WC system of similar mechanical properties [5]. Therefore, one of the major reasons why sample WNT seem to work well under the dry erosion test would be the effect of enlarging, and growing elongated WC grains.

3.3. *High-stress vs low stress abrasion*

The high-stress abrasive wear test conditions are severe for samples due to the high hardness of the abrasives, their sharpness, and the high-applied loads. Fig. 9 shows the results with respective to volumetric wear rate with WNT suffering the most wear. Neither TiC nor ZrC additives are particularly good at influencing the microstructure of WC–Ni to withstand high-stress abrasive wear when compared to the controlled sample. Fig. 10B shows WNT suffers from homogenous wear where both carbides and matrix are evenly worn and removed from the surface resulting in well pronounced grooves. The wear for WNT is even more pronounced as compared to WNO, even though WNT possesses higher hardness values. The material loss is likely due to two causes: first, TiC lowers the compressive strength of WC cemented carbides, lowering the fracture resistance [29]; second, the dynamics with coarse grain WC is wearing of the binder interlayers and subsequent micro-chipping [27]. One of the major wear mechanism comes loose abrasive particles that fracture and wear

carbide grains, which then act as micro-abrasives facilitating further material removal. The high stress abrasive tests were done under compressive loads; hence, WNT does not perform well. All three samples in Fig. 10 show evidence of binder smearing, given the abrasive nature of the test rig (sample corner contacting and rubbing again abrasive sandpaper).

WNO, as it is seen in Fig. 10A, suffers from a combination of 3-body abrasion with some WC grains removed and acting as an abrasive and also the retention of adhered abrasive particles on the surface, leading to a development of layers of particles providing protection against further wear [30]. Although WNZr possesses the highest hardness of the three samples, the hardness value of SiC is consequently higher. The harder and larger SiC particle in this test can easily damage the fine structure of WNZr leading to pull out of carbide grains and formation of cavities as seen in Fig. 10C. The submicron and near-nano cemented carbides are characterized by lower wear-resistance in comparison with the coarse-grain grade due to their reduced fracture toughness, fracture resistance and resistance to micro-fatigue [27,28]. This is shown in the sample WNO, which possesses the highest fracture toughness of all the samples.

Under low-stress abrasive conditions, large, blunt, but relatively soft silica abrasive is pressed against the sample via rubber wheel. The results of low-stress abrasive wear testing are shown in Fig. 11. WNT exhibited the best result showing a threefold wear resistance compared to WNZr. This is unexpected result since based on hardness alone, WNZr was expected to possess the best wear resistance as typically materials with high wear resistance have lowered coefficient of friction due to the high coercivity value indicating fine carbide grain size [13,29]. The low wear resistance of WNZr is attributed to the generalised high wear rate of WC cemented carbide possessing fine grain microstructure. Even with high hardness, due to WC grain refinement by ZrC, the WC grains are nevertheless of a micron size after some grain growth during sintering. WNZr represents the sample with the smallest WC grains thus even with a binder content of 8 wt%, this still exposes too much of the binder to the surface resulting in low wear resistance [5,27,28].

Depending on the appropriate laboratory tests, the results of WC cemented carbide wear resistance can be skewed one way or the other demonstrating the critical effect of grain size to the ability to resist wear. Konyashin et al. [28] shows that depending on low-stress or high-load wear tests, different aspects of the mechanical properties become important. Hardness and fracture toughness played an important role in wear damage during high-stress abrasion tests such as ASTM B611, while mean free path in the carbide microstructure is important to wear-resistance in low-stress abrasion ASTM G65 tests. This is evidently shown in Fig. 9 where under high-stress abrasion, sample WNZr and WNO outperform WNT due to properties of higher hardness in WNZr and higher toughness in WNO. WNT does not possess the necessary hardness and, particularly, fracture toughness combination to withstand high abrasion wear.

However, WNT performs better under low stress due to the sample's high MPF value. Under ASTM-G65 testing conditions, the movement of the abrasive over the contact surface plays a significant role in wear. In the low abrasion testing, WNT's high MFP means fine grains of abrasive are caught in-between the carbide grains giving an artificial protection against further wear. Given an

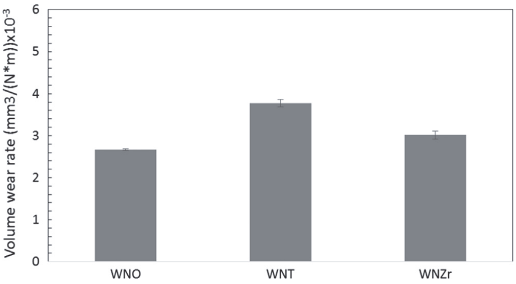

Fig. 9. Wear rates of materials under high-stress abrasive conditions.

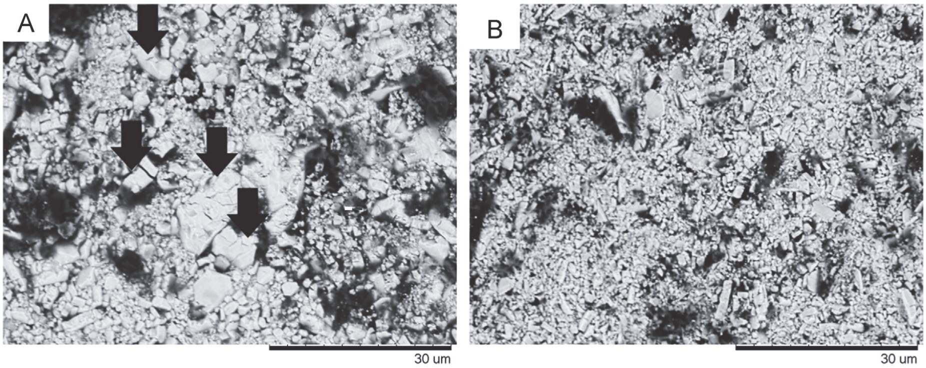

Fig. 8. SEM of dry erosion samples: (A) WNO with crack WC grains (black arrows) and (B) WNT.

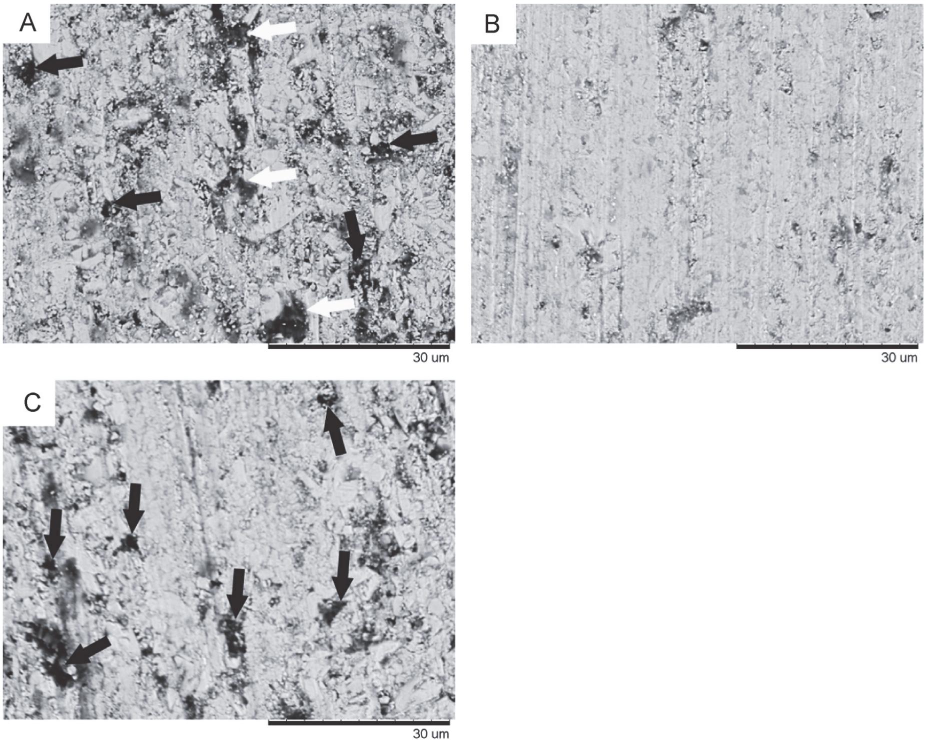

Fig. 10. SEM of samples under high-stress abrasion: (A) WNO, (B) WNT (C) WNZr. Black arrows indicate porosity due to carbide grain lost. White arrows indicate the leftover adhered abrasive particles. (B) WNT shows fine vertical grooves due to even wear.

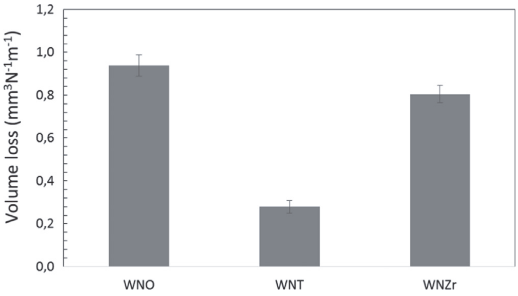

Fig. 11. Wear rate of materials under low-stress abrasive conditions.

applied load on a particle, high hardness favours particle sliding (grooving) whilst low hardness favours particle rolling [31]. Under low contact stress for cemented carbides, the prevailing mechanism of wear remain plastic deformation and microabrasion [32]. This is shown in Fig. 12 where the carbide grains are pull from WNT surface. Although WNO and WNT both possess larger grains compared to WNZr, WNO's MFP is significantly less than WNT, thus less abrasive fine dust is adhered to the surface. The lack of artificial protection from the adherence of fine abrasive dust leads WNO to further fracturing and fragmentation seen in Fig. 12A. These exposed WC grain undergo fracturing and the accumulate plastic deformation before removal from the surface [33]. Fig. 13 shows a scatter graph plotting wear loss versus MFP; WNT possesses two points performing well in the low-stress wear (dry erosion, G65 test), but a dramatic increase in wear under high-abrasion testing. Overall, TiC additive into WC–8 wt%Ni works best for a host of wear conditions except anything with a high stress factor as summarised in Fig. 14. The figure also shows WNZr does not seen to fit in any category showing any deviation from the control sample WNO. Its main role as a grain growth inhibitor that can increase the hardness of the cemented carbide is evident, but offers no wear benefits.

4. Conclusions

Fine grain WC powder was used to make WC–8 wt%Ni cemented carbides with either TiC or ZrC additives. The samples were subjected to wear resistance test under two schemes: 1) slurry verses dry erosion; 2) high stress verses low stress abrasion. Microstructural analysis and mechanical characterisation reveal ZrC to have a grain growth inhibition effect on WC grains resulting in a higher hardness but lower fracture toughness for the ZrC doped composite as compared to the reference hardmetal and composite doped with TiC. While the hardness is higher for WNT than WNO, the grain growth is also slightly more prevalent. Under dry erosive wear, WNT performed well with half as much volume loss compared to WNZr or WNO. WNT was also the material with the highest mean free path value so it performed well under low stresses. TiC tends to reduce the compressive strength of WC cemented carbides; therefore, when tests were conducted under high-stresses, the surface carbides and binder were evenly worn away. The function of ZrC on WC-Ni does not provide any

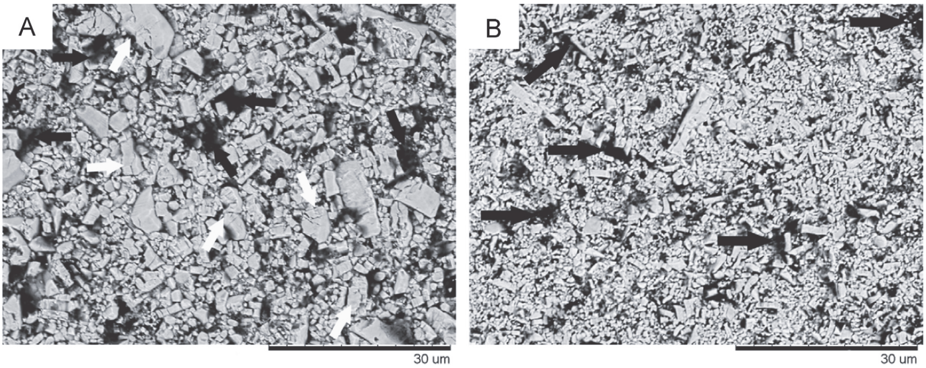

Fig. 12. SEM images from low stress test: (A) WNO and (B) WNT White arrow indicate fractured grains; black arrows are sites of carbide pull out.

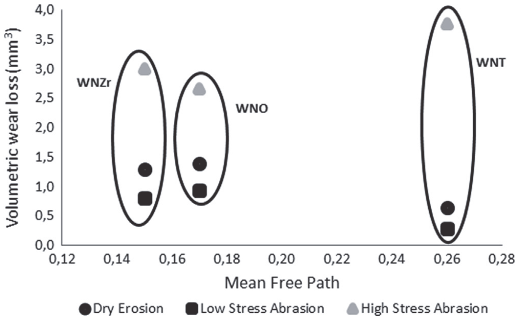

Fig. 13. Scatter between volumetric wear lost verse mean free path of samples.

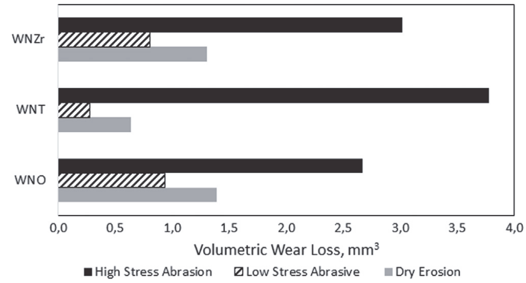

Fig. 14. Combined data of dry erosion, low and high stress abrasion tests for the samples tested in this work.

meaningful benefit to wear resistance, even though mechanically, the composite is harder and grain growth is inhibited. That alone is not sufficient to sustain against abrasive wear, as the resulting refined microstructure did not stand well against high-stress abrasive nor erosive wear in this study.

Acknowledgements

This work was supported by the Estonian Ministry of Education and Research (IUT 19–29). The authors would like to acknowledge the financial support of the European Commission for the Project NeTTUN, from the Seventh Framework Programme for Research, Technological Development and Demonstration (FP72007–2013) under Grant agreement 280712. The authors wish to thank M. Viljus from the Centre of Materials Research at Tallinn University of Technology for help with sample analysis.

References

[1] G.E. Springgs, A history of fine grained hardmetals, Int. J. Refract. Met. Hard Mater. 13 (1995) 241–255.

[2] P. Jakobsen, J. Lohne, Challenges of methods and approaches for estimating soil abrasivity in soft ground TBM tunnelling, Wear 308 (1–2) (2013) 166–173.

[3] X. Ren, H. Miao, Z. Peng, A review of cemented carbides for rock drilling: an old but still tough challenge in geo-engineering, Int. J. Refract. Met. Hard Mater. 39 (2013) 61–77.

[4] I. Konyashin, B. Ries, D. Hlawatschek, Y. Zhuk, A. Mazilkin, B. Straumal, F. Dorn, D. Park, Wear-resistance and hardness: are they directly related for nanostructured hard materials? Int. J. Refract. Met. Hard Mater. 49 (2015) 203–211.

[5] I. Konyashin, B. Ries, F. Lachmann, Near-nano WC–Co hardmetals: will they substitute conventional coarse-grained mining grades? Int. J. Refract. Met. Hard Mater. 28 (4) (2010) 489–497.

[6] I. Sevim, I.B. Eryurek, Effect of fracture toughness on abrasive wear resistance of steels, Mater. Des. 27 (10) (2006) 911–919.

[7] G. Gille, B. Szesny, K. Dreyer, H. van den Berg, J. Schmidt, T. Gestrich, G. Leitner, Submicron and ultra grained hardmetals for microdrills and metal and cutting inserts, Int. J. Refract. Met. Hard Mater. 20 (2002) 3–22.

[8] E. Detournay, T. Richard, M. Shepherd, Drilling response of drag bits: theory and experiment, Int. J. Rock Mech. Min. Sci. 45 (8) (2008) 1347–1360.

[9] I. Hussainova, M. Antonov, N. Voltsihhin, Assessment of zirconia doped hardmetals as tribomaterials, Wear 271 (9–10) (2011) 1909–1915.

[10] N. Voltsihhin, I. Hussainova, R. Traksmaa, K. Juhani, Optimisation of WC–Ni–ZrO$_2$ Structure, in: Proceedings of the European Conference on Composite Materials, 15, 2012, pp. 1–8.

[11] I. Preis, R. Traksmaa, A. Smirnov, I. Hussainova, E. Kimmari, Processing and microstructural characterization of WC-based cermets doped by ZrO2, Estonian J. Eng. 15 (4) (2009) 275.

[12] K. Bonny, P. De Baets, J. Vleugels, S. Huang, O. Van der Biest, B. Lauwers, Impact of Cr_3C_2/VC addition on the dry sliding friction and wear response of WC–Co cemented carbides, Wear 267 (9–10) (2009) 1642–1652.

[13] L. Espinosa, V. Bonache, M.D. Salvador, Friction and wear behaviour of WC–Co–Cr_3C_2–VC cemented carbides obtained from nanocrystalline mixtures, Wear 272 (1) (2011) 62–68.

[14] J. Poetschke, V. Richter, R. Holke, Influence and effectivity of VC and Cr3C2 grain growth inhibitors on sintering of binderless tungsten carbide, Int. J. Refract. Met. Hard Mater. 31 (2012) 218–223.

[15] A.V. Shatov, S.S. Ponomarev, S.A. Firstov, Modeling the effect of flatter shape of WC crystals on the hardness of WC-Ni cemented carbides, Int. J. Refract. Met. Hard Mater. 27 (2) (2009) 198–212.

[16] A.V. Shatov, S.S. Ponomarev, S.A. Firstov, Fracture of WC–Ni cemented carbides with different shape of WC crystals, Int. J. Refract. Met. Hard Mater. 26 (2) (2008) 68–76.

[17] X. Ren, Z. Peng, C. Wang, Z. Fu, L. Qi, H. Miao, Effect of ZrC nano-powder addition on the microstructure and mechanical properties of binderless tungsten carbide fabricated by spark plasma sintering, Int. J. Refract. Met. Hard Mater. 48 (2015) 398–407.

[18] J. Weidow, H.-O. Andrén, Grain and phase boundary segregation in WC–Co with TiC, ZrC, NbC or TaC additions, Int. J. Refract. Met. Hard Mater. 29 (1) (2011) 38–43.

[19] Y. Pan, D.Y. Li, H. Zhang, Enhancing the wear resistance of sintered WC–Co composite by adding pseudo-elastic TiNi constituent, Wear 271 (9–10) (2011) 1916–1921.

[20] F. Sergejev, M. Antonov, Comparative study on indentation fracture toughness measurements of cemented carbides, Proc. Estonian Acad. 12 (4) (2006) 388–398.

[21] H. Abrams, Grain size measurement by the intercept method, Metallography 4 (1) (1971) 59–78.

[22] M. Antonov, A. Zikin, I. Hussainova, Improved centrifugal tribodevice for ranking materials for slurry transport system, in: Proceedings of the 2nd International Conference on Abrasive Processes, 1 (1), 2014, p. 1.

[23] I. Hussainova, Microstructure and erosive wear in ceramic-based composites, Wear 258 (1–4) (2005) 357–365.

[24] ASTM, Standard Test Method for Pin Abrasion Testing, The American Society for Testing and Materials, West Conshohocken, 1 (1), 2001. pp. 1–8.

[25] H.-C. Kim, D.-K. Kim, K.-D. Woo, I.-Y. Ko, I.-J. Shon, Consolidation of binderless WC–TiC by high frequency induction heating sintering, Int. J. Refract. Met. Hard Mater. 26 (1) (2008) 48–54.

[26] V.E. Buchanan, P.H. Shipway, D.G. McCartney, Microstructure and abrasive wear behaviour of shielded metal arc welding hardfacings used in the sugarcane industry, Wear 263 (1–6) (2007) 99–110.

[27] I. Konyashin, B. Ries, Wear damage of cemented carbides with different combinations of WC mean grain size and Co content. Part II: laboratory performance tests on rock cutting and drilling, Int. J. Refract. Met. Hard Mater. 45 (2014) 230–237.

[28] I. Konyashin, B. Ries, Wear damage of cemented carbides with different combinations of WC mean grain size and Co content. Part I: ASTM wear tests, Int. J. Refract. Met. Hard Mater. 46 (2014) 12–19.

[29] R. van der Merwe, N. Sacks, Effect of TaC and TiC on the friction and dry sliding wear of WC–6 wt% Co cemented carbides against steel counterfaces, Int. J. Refract. Met. Hard Mater. 41 (2013) 94–102.

[30] K. Bonny, P. De Baets, Y. Perez, J. Vleugels, B. Lauwers, Friction and wear characteristics of WC–Co cemented carbides in dry reciprocating sliding contact, Wear 268 (11–12) (2010) 1504–1517.

[31] S.M. Nahvi, P.H. Shipway, D.G. McCartney, Particle motion and modes of wear in the dry sand–rubber wheel abrasion test, Wear 267 (11) (2009) 2083–2091.

[32] J. Pirso, S. Letunovitš, M. Viljus, Friction and wear behaviour of cemented carbides, Wear 257 (3–4) (2004) 257–265.

[33] M.G. Gee, A. Gant, B. Roebuck, Wear mechanisms in abrasion and erosion of WC/Co and related hardmetals, Wear 263 (1–6) (2007) 137–148.

Paper IV: **Yung DL**, Cygan S, Antonov M, Jaworska L, Hussainova I. Ultra high-pressure spark plasma sintered ZrC-Mo and ZrC-TiC composites. *International Journal of Refractory Metals and Hard Materials.* (2016) 61, 201-206, DOI: http://dx.doi.org/10.1016/j.ijrmhm.2016.09.014

Int. Journal of Refractory Metals and Hard Materials 61 (2016) 201–206

Contents lists available at ScienceDirect

Int. Journal of Refractory Metals and Hard Materials

journal homepage: www.elsevier.com/locate/IJRMHM

Ultra high-pressure spark plasma sintered ZrC-Mo and ZrC-TiC composites

Der-Liang Yung [a], Sławomir Cygan [b], Maksim Antonov [a], Lucyna Jaworska [b], Irina Hussainova [a,c,d,*]

[a] Department of Mechanical Engineering, Tallinn University of Technology, Ehitajate tee 5, 19086 Tallinn, Estonia
[b] Institute of Advanced Manufacturing Technology, 30-011 Krakow, ul. Wroclawska 37A, Poland
[c] ITMO University, Kronverksky 49, St. Petersburg 197101, Russian Federation
[d] Department of Mechanical Science and Engineering, University of Illinois at Urbana-Champaign, 1206 West Green Street, Urbana, IL 61801, USA

ARTICLE INFO

Article history:
Received 17 July 2016
Received in revised form 18 September 2016
Accepted 27 September 2016
Available online 29 September 2016

Keywords:
Spark plasma sintering
HPHT
Mechanical properties
ZrC-Mo
ZrC-Ti

ABSTRACT

Ultra-high-pressure spark plasma sintering was applied to ZrC-20 wt%Mo and ZrC-20 wt%TiC composites with a pressure up to 7.8 GPa and temperatures of 1550 °C and 1950 °C. Mechanical performance of the composites was benchmarked against a plain ZrC produced by the same method. Both composites outperformed the pure ZrC with superior hardness and indentation fracture toughness of 2239 HV1 and 5.4 MPa $m^{1/2}$, and 1896 HV1 and 5.9 MPa $m^{1/2}$, respectively, for ZrC-Mo and ZrC-TiC composites. It was shown that ultra-high compaction pressure affected the ZrC-20 wt%TiC miscibility gap by lowering the temperature threshold from the usually applied 1800 °C down to 1550 °C resulting in formation of the solid state solution of (Zr,Ti)C. In contrast, the high pressure does not inhibit the carburisation of Mo with ZrC to form MoC, even when experiments were performed in a graphite free environment. The equiaxed morphology of ZrC grains along with a right-shift in XRD peaks for ZrC indicates dissolution of Mo in ZrC resulting in formation of the solid solution of (Zr,Mo)C. High-temperature X-ray diffraction analysis under oxidation conditions was performed on the samples showing degradation of ZrC-20 wt%Mo due to the oxidation of Mo at high-temperature leading to MoO_3 vaporisation. Conversely, the oxidation of ZrC-20 wt%TiC composites was characterised by formation of ZrO_2 and TiO_2 remaining stable up to 1500 °C.

1. Introduction

Zirconium carbide (ZrC) is regarded as an important material either as an additive or a base material for high-temperature composites. The ultra-high melting point (~3420 °C) of ZrC along with its high hardness (~25.5 GPa), low electrical resistivity (4.3×10^{-7} Ω·cm), high modulus of elasticity (~400 GPa), and relatively low density (6.73 g cm^{-3}) make this carbide attractive candidate for many applications that require exposure to extreme thermal and chemical environments [1]. Moreover, ZrC-based alloys display strong resistance to irradiation damage and are widely used as cladding nuclear materials [2]. However, the strong covalent Zr—C bonding and a low self-diffusion coefficient makes processing of dense monolithic ZrC bulks a difficult task which, combined with a low fracture toughness of the pure ZrC (~4.0 MPa $m^{1/2}$), limits usage of the material for mechanically rigorous applications [3,4]. As for an ultra-refractory compound, very high-temperatures and pressure-assisted techniques are usually required to achieve dense bulks of zirconium carbide [5].

Various attempts have been made to improve toughness and mechanical performance of zirconium carbides by introducing a second phase or appropriate sintering aids to the ZrC matrix. For example, ZrC–Mo composites of >98% relative density were produced by hot isostatic pressing at 1800 °C and 200 MPa for 1 h [6,7]. However, the processing requires a non-carburising environment below 2100 °C since molybdenum readily reacts with carbon producing Mo_2C or MoC [4]. Therefore, the goal to achieve a liquid phase sintering and to produce viable ZrC-Mo cermet is compromised by a lack of metallic Mo in the system. Another approaches are either fabrication the solid-state solution with titanium carbide (TiC) [8–10], which requires adjusting molar ratios and high-temperature sintering (>2000 °C) [11], or incorporation of a tetragonal zirconia in an attempt to utilize a phase transformation toughening mechanism [3].

According to Markström et al. [12], the thermodynamic evaluation of the TiC-ZrC system has been performed to estimate a miscibility gap. The composite of ZrC-20 wt%TiC would have an approximate miscibility gap at ~1850 °C according to molar fraction ZrC_X-TiC_{1-X}, where x = 70 mol fraction). The mixed (Ti,Zr)C phase should be stable at high-temperatures, but decompose into TiC and ZrC at lower temperatures. Borgh et al. [13] suggested that mixed carbide could be used as a strengthening constituent in, for example, cemented carbides. It is believed that the new superhard mixed carbide has a high potential in

---

[*] Corresponding author at: Department of Mechanical Engineering, Tallinn University of Technology, Ehitajate tee 5, 19086 Tallinn, Estonia.
E-mail address: hussaino@illinois.edu (I. Hussainova).

http://dx.doi.org/10.1016/j.ijrmhm.2016.09.014
0263-4368/

various engineering applications such as in bulk cemented carbide and cermet cutting tools, and in surface coatings [14].

Much of the nowadays research onto the Group IV refractory carbides have centred around using spark plasma sintering (SPS) technology to synthesise the composites [8–11,15–18]. SPS offers fast heating rates, high-temperature sintering, and appropriate pressures to consolidate refractory carbides. Recently, the bulk products with relative density above 97% were obtained from as-received commercial ZrC powder by SPS operating at temperatures of 2100 °C [15]. Moreover, about 97.9% dense ZrC samples were recently obtained by SPS at 1800 °C, when the applied pressure was increased to 200 MPa [19]. The densification behavior is generally improved in the presence of mechanical loads and compaction pressure plays a significant role in the process of materials consolidation. As an example, the applied external pressure was specified as the most important hot pressing parameter, which controls the densification behavior of hot-pressed ZrB_2–SiC composites [20], however, such an importance was not observed in the monolithic [21] or carbon fiber reinforced ZrB_2-based ceramics [22]. High pressures up to 1 GPa with sintering below 1000 °C has shown to produce nanocrystalline zirconia (ZrO_2) [23] and yttria (Y_2O_3) [24]. Fabrication of a transparent alumina (Al_2O_3) synthesised with high-pressure compaction between 500 MPa to 8 GPa with sintering temperatures as low as 460 °C has been reported in [25–30]. Research on high-pressure high-temperature (HPHT) sintering refractory materials is rather limited, focusing on tantalum and tungsten/tungsten carbide [27,31,32].

The aim of this work is to exploit the potential of the HPHT SPS technique, attempting the densification of zirconium carbide based composites. In this study, we examined the influence of ultra-high-pressure of 7.8 GPa on sinterability and mechanical performance of the ZrC-20 wt%Mo and ZrC-20 wt%TiC materials. The HPHT SPS allows the powders to be sintered in a carbon-free environment, which is particularly important to achieve a viable ZrC-Mo cermet. A special attention is given to the microstructure and composition of the materials after processing as well as their mechanical properties. The HPHT SPS produced samples were also examined with a high-temperature XRD (HT-XRD) under oxidation conditions up to a temperature of 1500 °C to determine their phase transitions.

2. Materials and methods

Commercially available ZrC powder (~3.6 μm, Pacific Particulate Materials (PPM), 99% purity ZrC-7643) underwent ball milling with either 20 wt%Mo (1.0–3.0 μm, PPM, 99% purity Mo-7164) or 20 wt%TiC powder (2–3 μm, PPM, 99% purity TiC-2088). The compositions were milled for 48 h in a tungsten carbide mill using TiC-NiMo balls in a 8:1 wt% ball to powder ratio along with ethanol as a milling liquid. The powders were dried for 24 h at 50 °C, then sieved to 200 μm.

The densification process was carried out using the Bridgman-type toroidal apparatus. In this system, quasi-isostatic compression of the preliminary consolidated powders is achieved as a result of plastic deformation of the mineral gasket material (usually meta-morphic stones) between anvils [33]. The HPHT SPS equipment, shown in Fig. 1, consisted of a high tonnage hydraulic press equipped with a Bridgman anvil, and a direct-pulsed current generator with an accompanying computer control system. The homogeneously mixed powders were pre-pressed into pellets in tantalum foil capsules under the pressure of 200 MPa, fitted into graphite discs and ceramic gaskets, and then placed into the machine. A high-power transformer and graphite heater provided electrical heating to the sample. The resulting samples were circular 1 cm diameter discs with a height of 5 mm. Three experimental samples were synthesised for each material.

The sintering was carried out in a SPS furnace under vacuum, with heating provided by a 1 kHz pulsed current, which passed directly through the graphite heater. Since our composites were conductive, the current also passed through the powder compact allowing high-energy pulses of a direct current leading to the activation of the powder. This also generated an electric discharge in the neck region. The sintering temperatures were measured by an optical pyrometer focused on the half-through hole in the graphite die. The samples were each synthesised separately and up to three experiments were made for each materials for experiment average.

Table 1 displays the optimized sintering parameters to produce the materials of the highest reliability, which undergo further analysis. Cooling time was done by ambient temperature.

The produced samples were ground and polished with diamond solution to a 1 μm finish. The bulk densities of the as-sintered samples were measured by Archimedes' technique using distilled water medium while their theoretical density was calculated applying the rule of mixtures. The hardness and the indentation fracture toughness were determined by the Vickers indentation method applying load of 9.81 N (1 kg) and a dwell time of 10 s using an INDENTEC hardness testing machine. For each sample at least 8 indentations were made and results averaged. The stress intensity factor K_{IC} was calculated from the length of cracks formed by a Vickers indenter using the Palmqvist method based on Evan and Wilshaw's equation [34]:

$$K_{IC} = 0.079\frac{P}{a^{(3/2)}}\log\left(4.5\frac{a}{c}\right) \tag{1}$$

where P is the applied load (N), a is the length of the indent from the centre, and c is the total crack length propagated from the indented centre. Young's modulus of the composites was determined by ultrasonic wave transition method measuring the velocity of ultrasonic sound waves passing through the material using a flaw detector (Panametrics Epoch III). The calculations were carried out according to the following formula:

$$E = \rho\, CL\left(3\frac{C_L^2}{4C_T^2} - \frac{C_L^2}{C_T^2}\right) \tag{2}$$

where ρ is a density of the material, C_L is a velocity of the longitudinal wave, C_T is a velocity of the transversal wave. The velocities of transversal and longitudinal waves were determined as a ratio of the sample thick-ness and the relevant transition time.

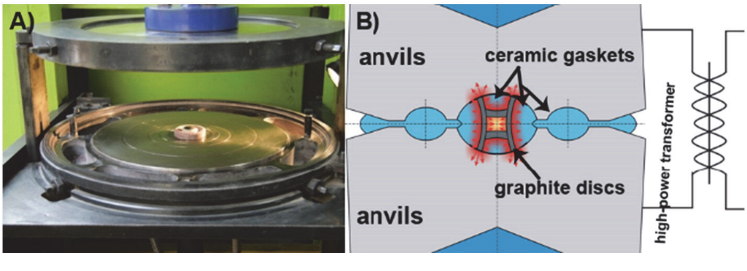

Fig. 1. (A) - HPHT SPS machine demonstrating anvil lifted up and a sample placed at the centre; and (B) - detailed view of compaction and SPS components.

Table 1
The HPHT parameters optimized for each sample composition.

Sample	Dwell time [s]	Temp. [°C]	Pressure [GPa]
ZrC	40	1550 ± 50	7.2 ± 0.2
ZrC-Mo	20	1900 ± 50	7.8 ± 0.2
ZrC-TiC	40	1550 ± 50	7.8 ± 0.2

The microstructures of the composites were examined under scanning electron microscopy (FE-SEM Hitachi S-4700, Japan) after etching with HF:HNO_3:H_2O (1:1:2 vol.%) solution for 10 s. Chemical composition was analyzed with X-ray diffraction (Empyrean, by PANalytical equipped with high-temperature chamber Anton Paar HTK 2000 N) by using the copper radiation (λCu Kα = 1.5418 Å). The measurements were carried out at room temperature as well as at 800 °C, 1000 °C, 1200 °C and 1500 °C in air. The HT-XRD parameters involved a heating rate of 20 °C min^{-1}, with each dwell time lasting 30 min before taking 1 h to do XRD scans at the dwell temperature.

3. Results and discussions

3.1. Synthesis

To produce the composites of the highest density and mechanical performance, an optimization of the HPHT SPS process was performed by variations of processing parameters such as dwelling time, temperature, and pressure. Given the experimental nature of the HPHT SPS system, an exact temperature measurement during operations was not possible. A special gasket assembly equipped with thermocouple calibrated the temperature based on filling degree of the direct pulse current. Likewise, the temperature ramp rate was also based on the filling degree, which is estimated to be between 200 and 300 °C s^{-1}.

In the high-pressure activated sintering processes, plastic deformation is the primary mechanism of mass transport and, consequently, it should be possible to obtain fully densified materials during time significantly lower than usually applied for the pressure-less processing. The ZrC-Mo cermet required a higher SPS temperature as compared to the plain ZrC and ZrC-TiC composite to produce a dense sample [10,18]. The samples obtained by HPHT within whole sintering temperature range from 1350 to 1950 °C had a bit higher densities and better mechanical properties in comparison to the samples sintered by SPS at the pressures of 50–100 MPa. To obtain a viable product, only 20 s and 40 s were required for consolidation of the ZrC-Mo and ZrC-TiC materials, respectively, when the pressure was kept at 7.8 ± 0.2 GPa.

3.2. Mechanical properties

High compaction pressure densifies powder by rearranging the particles, where the nuclei distances between spheres are dramatically shortened. The result is increase grain-to-grain contact area and intergranular elastic deformation (microstrains) in the surface shell. High stress contact points cause plastic deformation, closing the pores, and densifying the powder [31]. The sintering conditions specified in Table 1, materials of high densities (relative density > 98%) with Young's modulus value exceeding 340 GPa for ZrC-Mo and 319 GPa for ZrC-TiC were produced.

The mechanical properties of the samples are shown in Table 2 and compared with the samples of similar composition produced with the help of conventional SPS. The highest measured values of 2239 HV_1 and 5.4 MPa $m^{1/2}$ for hardness and fracture toughness, respectively, for ZrC-20 wt%Mo produced by HPHT process reflect no significant effect on the properties when compared to the properties of the cermet produced by conventional SPS. This reinforces the notion that for the ZrC-Mo composites, the sintering temperature affects the bulk density of the sample [6]. One consistent conclusion is that higher compaction pressure does densified the ZrC-20 wt%Mo sample up to > 98%.

Table 2
Mechanical properties of samples consolidated by HPHT and SPS.

HPHT SPS	Relative density [%]	Hardness [HV_1]	K_{IC} [MPa $m^{1/2}$]	Young Modulus [GPa]
ZrC-20 wt%Mo	98.6	2239 ± 38	5.4 ± 0.6	340 ± 7
ZrC-20 wt%TiC	96.4	1896 ± 40	5.9 ± 0.3	319 ± 6
SPS				
ZrC-20 wt%Mo [20]	97.7	2153 ± 34	5.5 ± 0.6	346 ± 16
ZrC-20 wt%TiC [10]	98.4	1878 ± 55	5.4 ± 0.5	347 ± 18

The application of HPHT SPS managed to slightly increase the toughness of ZrC-TiC by 10% with a value of 5.9 MPa $m^{1/2}$ as compared to values reported in [10]. In the present work, the mechanical values of ZrC-TiC for hardness and toughness are comparable to those obtained in the study by Liu et al. [9], although a higher sintering temperature of 1800 °C was applied. As for ZrC-Mo cermet, ultra-high-pressure does little to improve the mechanical properties of ZrC-20 wt%TiC composite. Research to characterise the compaction of ceramic powders and their compaction behavior takes into account macroscopic parameters related to the plastic deformation capacity of the powder, applied pressure, and density in the form of a phenomenological equation [35]. However, the equation does not take into consideration the effect of compaction pressure on the powders chemical properties, which maybe the case in our study and further discussed in the following section.

3.3. Microstructure and composition

Fig. 2 shows the SEM images of microstructure of materials produced by HPHT SPS. Fig. 2A reveals the surface of ZrC-20 wt%Mo after etching, clearly showing the ZrC grains (grey areas) of 2–3 μm in size

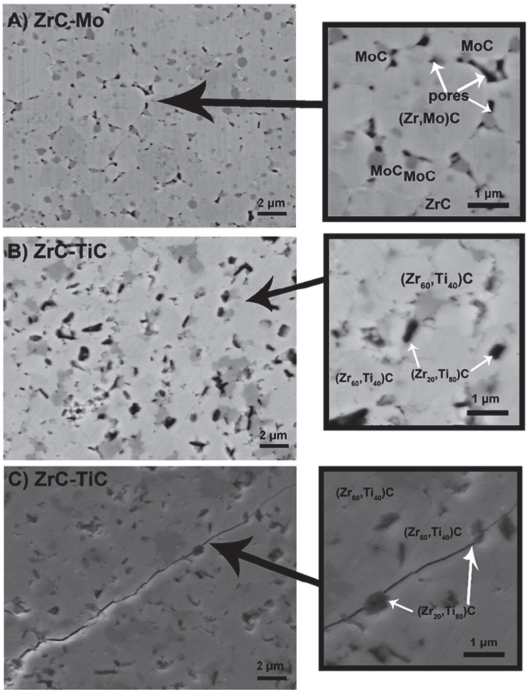

Fig. 2. SEM images of HPHT SPS samples: A) ZrC-Mo; B) ZrC-TiC; and C) a secondary electron image of the crack caused by indentation.

with no evidence of grain growth. The subsequent XRD analysis, Fig. 3, revealed the darker grey areas seen in Fig. 2A to be MoC with peaks at 36.3° and 43.3°. To ensure a non-carburising environment during sintering, tantalum foil was used to seal the powder; therefore, the only source of carbon would have come from the ZrC carburising with the Mo. The result is a microstructure composed primarily of solidified, equiaxed ZrC grains, an indication of the eutectic reaction with Mo to form (Zr,Mo)C. This is in accordance with other research showing an evident shift in the ZrC peaks towards higher 2θ values at 33.3° and 39.3° implying Mo dissolution into ZrC [7,18]. The shift in XRD pattern is clearly shown in Fig. 3 when the ZrC-Mo pattern is compared to the ZrC reference sample also produced by HPHT SPS. Alternatively, the presence of detected MoC could be the consequence of the ball milling parameters. Ohser-Wiedemann et al.'s [36] research into Mo-TiC composites proposed that the formation of Mo_2C is supported by either the higher concentration of crystal defects, which accelerated the carbon diffusion, or by the stronger fragmentation of TiC during aggressive high-energy powder milling. The effect of ultra-high-pressure compaction does not change the eutectic temperature between ZrC and Mo. Zirconium carbide absorbs the available molybdenum forming a solid solution (Zr,Mo)C at temperatures below 2100 °C. The fracture toughness in the ZrC-20 wt%Mo composite is, therefore, mostly attributed to solid solution strengthening. From the microstructure, it is evident the MoC started to interlace around the ZrC grains leaving visible pores in-between grains. This maybe a result of the very short sintering time, which was a technical necessity due to the temperature resistance of the gasket elements.

ZrC-TiC composite shows a mixed, solid solution microstructure as seen in Fig. 3B. The dark (almost black) areas are suspected to be Ti-rich phases according to secondary electronic images in Fig. 2C. One reason for the relatively high mechanical indentation fracture toughness of ZrC-TiC composite is bridging by Ti-rich solid solution $(Zr_{20}Ti_{80})C$ particles as cracks are deflected underneath or around the particle as seen in Fig. 2C. As for ZrC-TiC mixtures, there is a miscibility gap showing the dissolution of ZrC into TiC and vice versa creating a mixed carbide solid solution depending on the molar ratio of one carbide to the other. The SPS sintering of ZrC-TiC solid solution is made easier skewing towards the ZrC than TiC. The replacement of larger Zr ions by smaller Ti ones is easier than vice versa and thus the miscibility gaps are asymmetric [5,9]. Alternatively, development of ZrC-TiC solid-state solution would require adjusting molar ratios and a high sintering temperature (>2000 °C). Thermodynamic evaluation of the TiC-ZrC system [12] estimates that a composite of ZrC-20 wt%TiC has a miscibility gap at around 1850 °C. The mixed (Ti,Zr)C phase should be stable above this temperature, but decomposes into TiC and ZrC at lower temperatures. The effect of HPHT SPS on ZrC-20 wt%TiC shows that the miscibility gap can be influenced by applied compaction pressure. According to XRD patterns given in Fig. 3C, ZrC shifts to higher 2θ values revealing formation of Zr-rich solid solution $(Zr_{60}Ti_{40})C$ at 1600 °C that is reflected by strong peaks at 34° and 39.5°. Along with these peaks, the characteristic peaks of Ti-rich solid solution $(Zr_{20}Ti_{80})C$ are depicted by XRD. It should be noted that there is no detectable TiC (200) in the XRD pattern, which is most likely due to the peaks being overshadowed by the Ti-rich solid solution $(Zr_{20}Ti_{80})C$ phase at 35.8° and 41.6°.

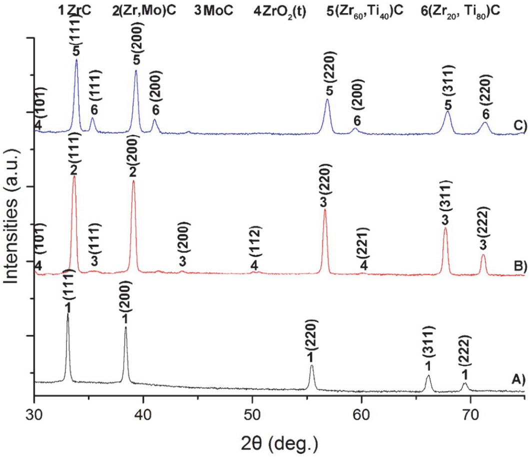

Fig. 3. XRD patterns of ZrC-based composites sintered by HPHT SPS: A) reference ZrC; B) ZrC-Mo; and C) ZrC-TiC.

The XRD pattern of the HPHT SPS produced ZrC-Mo reveals very subtle peaks of tetragonal zirconia impurities. In all probability during processing of the composite powders, which involved ball milling in air, trapping traces of oxygen were captured by the mixture. The rapid heating during HPHT SPS and ceramic/Ta seals prevented the trace oxygen from escaping at elevated temperatures resulting in oxide formation.

3.4. High-temperature oxidation

The main limitation for high-temperature applications for ZrC-based composites concerns the oxidation behavior as the carbides start to oxidize into non protective and porous scale of ZrO_2 at temperature above 600 °C. To study the compositional changes occurring at high-temperature, the samples of ZrC-20 wt%Mo and ZrC-20 wt%TiC produced by HPHT SPS were exposed to air in a closed chamber and temperature ramped to various set points before XRD analysis is done at each set point. Fig. 4 details the phase changes for ZrC-20 wt%Mo starting from 800 °C, where the formation of oxide species ZrO_2 and MoO_3 are detected at 30.2°, 23° and 25°, respectively. The evaporation of the molybdenum trioxide (MoO_3) starts at around 700 °C and the evaporation rate becomes much more significant beyond the melting point of MoO_3 at 790 °C. The peaks of (Zr,Mo)C and MoC are still depicted at 800 °C, while peak of (Zr,Mo)C disappears by 1000 °C. The evaporation of MoO_3 can cause catastrophic breakdown and expedited oxidation of (Zr,Mo)C phase. Orthorhombic MoO_3 is detected to be a major peak at 27.5° supporting the aggressive oxidation of any Mo at 1000 °C. When the temperature reaches 1200 °C, only ZrO_2 is detectable, implying MoO_3 to have been completely evaporated. These results show that ZrC-20 wt%Mo oxidation kinetics is affected by the mechanism of Mo oxidation.

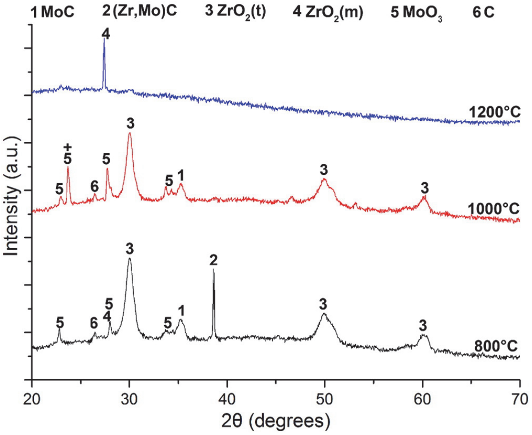

Fig. 4. HT-XRD pattern of ZrC-20 wt%Mo produced by HPHT SPS. The "+" symbol indicates orthorhombic MoO_3.

ZrC-20 wt%TiC composite undergoes a less dramatic shift in phase changes when exposed to oxidation at high-temperatures. Fig. 5 shows phases detected at 1000 °C showing formation of oxides ZrO_2 and TiO_2 at 30°. Carbides (Zr,Ti)C, either Zr-rich or Ti-rich areas, are well pronounced at temperature range from 1000 °C to 1500 °C. The oxide peaks are strong suggesting the continuous surface oxidation. There are peaks in the XRD scan at 1200 °C and 1500 °C at 33°, which appear due to the dissolution between ZrC and TiC the development of mixed oxide solid solution $(Zr,Ti)O_2$. However, $(Zr,Ti)O_2$ possesses a unique diffraction peak at 32°, which does not appear in the XRD patterns. Therefore, this peak may reflect the presence of un-oxidized ZrC. The presence of ZrO_2 and oxidation of carbides also likely yielded free carbon. ZrO_2 and free carbon can react at high-temperatures to produce ZrC during possible self-propagating synthesis [37]. The intensity of this peak grows between 1200 and 1500 °C, which is in agreement with carbo-thermal synthesis at the same temperature.

4. Conclusions

In this research, ZrC-20 wt%Mo and ZrC-20 wt%TiC composites were sintered at ultra-high pressure of 7.8 GPa and temperatures of 1900 and 1550 °C, respectively, using HPHT SPS method. Both composites showed no significant effect of the high pressure onto hardness and indentation fracture toughness as benchmarked the materials of the same composition produced with the help of SPS technique at the same temperatures and pressure of 50–100 MPa. Cermet ZrC-20 wt%Mo sintered with HPHT method, even during a very short dwell time of 20 s, achieved Young's modulus of 340 GPa, hardness of 2239 HV_1 and fracture toughness of 5.4 MPa $m^{1/2}$. The composite ZrC-20 wt%TiC was sintered during 45 s to achieve Young's modulus of 319 GPa, hardness of 1896 HV_1 and fracture toughness of 5.9 MPa $m^{1/2}$. HPHT SPS and sintering in a non-carburising environment did not substantially inhibit the eutectic reaction between Mo and ZrC: Mo dissolution into ZrC still occurred and Mo was carburised with formation of MoC grains. HPTH SPS influenced ZrC-TiC by lowering the miscibility gap temperature for ZrC-20 wt%TiC below the 1850 °C threshold. ZrC-TiC composite was shown to form solid solution of Zr-rich and Ti-rich areas in the microstructure at a temperature of 1600 °C.

Subsequent high temperature XRD analysis reveals severe oxidation of ZrC-20 wt%Mo cermet at temperatures higher than 800 °C. Upon higher temperatures up to 1200 °C, the product of oxidation, MoO_3, is completely evaporated causing catastrophic disintegration of the sample. In contrast, ZrC-20 wt%TiC underwent oxidation up to 1500 °C with a consistently growth of oxides ZrO_2 and TiO_2.

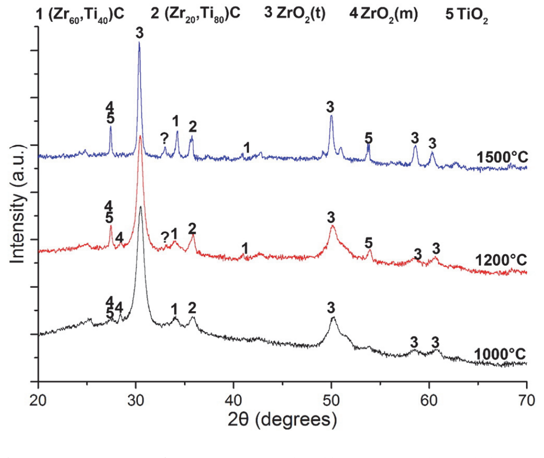

Fig. 5. HT-XRD patterns of ZrC-20 wt%TiC produced by HPHT SPS. The symbols "?" are suspected to be $(Zr,Ti)O_2$ or ZrC.

Acknowledgements

This work was supported by the Eesti Teadusagentuur (PUT1063, I. Hussainova), Tallinn University of Technology young researcher basic financing (B56, Maksim Antonov), and the Institutional Research Funding (IUT 19-29) of the Estonian Ministry of Education and Research. The author would also like to thank Dr. Jolanta Cyboroń (IAMT) for XRD analysis and Dr. Mart Viljus (TUT) for SEM imaging.

References

[1] H.O. Pierson, Handbook of Refractory Carbides and Nitrides William Andres Publishing/Noyes, Westwood, NJ, 1996.

[2] S. Pellegrino, L. Thomé, A. Debelle, S. Miro, P. Trocellier, Radiation effects in carbides: TiC and ZrC versus SiC, Nucl. Instrum. Methods Phys. Res., Sect. B 327 (2014) 103–107.

[3] I. Hussainova, N. Voltšihhin, E. Cura, S.-P. Hannula, Densification and characterization of spark plasma sintered ZrC–ZrO_2 composites, Mater. Sci. Eng. A 597 (2014) 75–81.

[4] S.E. Landwehr, G.E. Hilmas, W.G. Fahrenholtz, I.G. Talmy, Processing of ZrC-Mo cermets for high-temperature applications, Part I: chemical interactions in the ZrC–Mo system, J. Am. Ceram. Soc. 90 (2007) 1998–2002.

[5] O. Adjaoud, G. Steinle-Neumann, B.P. Burton, A. van de Walle, First-principles phase diagram calculations for the HfC–TiC, ZrC–TiC, and HfC–ZrC solid solutions, Phys. Rev. B 80 (2009) 134112.

[6] S.E. Landwehr, G.E. Hilmas, W.G. Fahrenholtz, I.G. Talmy, Processing of ZrC–Mo cermets for high temperature applications, Part II: pressureless sintering and mechanical properties, J. Am. Ceram. Soc. 91 (2008) 873–878.

[7] S.E. Landwehr, G.E. Hilmas, W.G. Fahrenholtz, I.G. Talmy, S.G. DiPietro, Microstructure and mechanical characterization of ZrC–Mo cermets produced by hot isostatic pressing, Mater. Sci. Eng. A 497 (2008) 79–86.

[8] Y. Li, H. Katsui, T. Goto, Effect of heat treatment on the decomposition of TiC–ZrC solid solutions by spark plasma sintering, J. Eur. Ceram. Soc. (2016).

[9] S. Liu, W. Hu, J. Xiang, F. Wen, B. Xu, D. Yu, J. He, Y. Tian, Z. Liu, Mechanical properties of nanocrystalline TiC–ZrC solid solutions fabricated by spark plasma sintering, Ceram. Int. 40 (2014) 10517–10522.

[10] D. Yung, I. Hussainova, M. Rodriguez, R. Traksmaa, Processing of ZrC–TiC composites by SPS, Key Eng. Mater. 674 (2016) 94–99.

[11] Y. Li, H. Katsui, T. Goto, Spark plasma sintering of TiC–ZrC composites, Ceram. Int. 41 (2015) 7103–7108.

[12] A. Markström, K. Frisk, Experimental and thermodynamic evaluation of the miscibility gaps in MC carbides for the C–Co–Ti–V–W–Zr system, Calphad 33 (2009) 530–538.

[13] I. Borgh, P. Hedström, A. Blomqvist, J. Ågren, J. Odqvist, Synthesis and phase separation of (Ti,Zr)C, Acta Mater. 66 (2014) 209–218.

[14] T. Ma, P. Hedström, V. Ström, A. Masood, I. Borgh, A. Blomqvist, J. Odqvist, Self-organizing nanostructured lamellar (Ti,Zr)C — a superhard mixed carbide, Int. J. Refract. Met. Hard Mater. 51 (2015) 25–28.

[15] D. Sciti, S. Guicciardi, M. Nygren, Spark plasma sintering and mechanical behaviour of ZrC-based composites, Scr. Mater. 59 (2008) 638–641.

[16] M. Umalas, I. Hussainova, V. Reedo, D.-L. Young, E. Cura, S.-P. Hannula, R. Lõhmus, A. Lõhmus, Combined sol–gel and carbothermal synthesis of ZrC–TiC powders for composites, Mater. Chem. Phys. 153 (2015) 301–306.

[17] S.-K. Sun, G.-J. Zhang, W.-W. Wu, J.-X. Liu, T. Suzuki, Y. Sakka, Reactive spark plasma sintering of ZrC and HfC ceramics with fine microstructures, Scr. Mater. 69 (2013) 139–142.

[18] D.-L. Yung, M. Antonov, I. Hussainova, Spark plasma sintered ZrC-Mo cermets: influence of temperature and compaction pressure, Ceram. Int. 42 (2016) 12907–12913.

[19] X. Wei, C. Back, O. Izhvanov, O. Khasanov, C. Haines, E. Olevsky, Spark plasma sintering of commercial zirconium carbide powders: densification behavior and mechanical properties, Materials 8 (2015) 6043–6061.

[20] M. Jaberi Zamharir, M. Shahedi Asl, N. Pourmohammadie Vafa, M. Ghassemi Kakroudi, Significance of hot pressing parameters and reinforcement size on densification behavior of ZrB_2–25 vol% SiC UHTCs, Ceram. Int. 41 (2015) 6439–6447.

[21] M. Shahedi Asl, M. Ghassemi Kakroudi, B. Nayebi, H. Nasiri, Taguchi analysis on the effect of hot pressing parameters on density and hardness of zirconium diboride, Int. J. Refract. Met. Hard Mater. 50 (2015) 313–320.

[22] M. Shahedi Asl, F. Golmohammadi, M. Ghassemi Kakroudi, M. Shokouhimehr, Synergetic effects of SiC and Csf in ZrB_2-based ceramic composites. Part I: densification behavior, Ceram. Int. 42 (2016) 4498–4506.

[23] U. Anselmi-Tamburini, J.E. Garay, Z.A. Munir, Fast low-temperature consolidation of bulk nanometric ceramic materials, Scr. Mater. 54 (2006) 823–828.

[24] H. Zhang, B.-N. Kim, K. Morita, H. Yoshida, K. Hiraga, Y. Sakka, J. Ballato, Fabrication of transparent yttria by high-pressure spark plasma sintering, J. Am. Ceram. Soc. 94 (2011) 3206–3210.

[25] S. Grasso, B.-N. Kim, C. Hu, G. Maizza, Y. Sakka, Highly transparent pure alumina fabricated by high-pressure spark plasma sintering, J. Am. Ceram. Soc. 93 (2010) 2460–2462.

[26] S. Grasso, H. Yoshida, H. Porwal, Y. Sakka, M. Reece, Highly transparent α-alumina obtained by low cost high pressure SPS, Ceram. Int. 39 (2013) 3243–3248.
[27] Y. Kim, D. Lee, J. Hwang, H.J. Ryu, S.H. Hong, Fabrication and characterization of powder metallurgy tantalum components prepared by high compaction pressure technique, Mater. Charact. 114 (2016) 225–233.
[28] N. Kuskonmaz, N. Can, A. Can, L. Sigalas, Sintering behaviour of nano-crystalline γ-Al_2O_3 powder without additives at 2–7 GPa, Ceram. Int. 37 (2011) 437–442.
[29] S.C. Liao, Y.J. Chen, B.H. Kear, W.E. Mayo, High pressure/low temperature sintering of nanocrystalline alumina, Nanostruct. Mater. 10 (1998) 1063–1079.
[30] N. Nishiyama, T. Taniguchi, H. Ohfuji, K. Yoshida, F. Wakai, B.-N. Kim, H. Yoshida, Y. Higo, A. Holzheid, O. Beermann, T. Irifune, Y. Sakka, K.-i. Funakoshi, Transparent nanocrystalline bulk alumina obtained at 7.7 GPa and 800 °C, Scr. Mater. 69 (2013) 362–365.
[31] P. Liu, F. Peng, F. Liu, H. Wang, C. Xu, Q. Wang, X. Zhou, W. Yin, S. Yin, Y. Li, D. He, High-pressure preparation of bulk tungsten material with near-full densification and high fracture toughness, Int. J. Refract. Met. Hard Mater. 42 (2014) 47–50.
[32] Q. Zhou, P. Chen, Fabrication and characterization of pure tungsten using the hot-shock consolidation, Int. J. Refract. Met. Hard Mater. 42 (2014) 215–220.
[33] L.G. Khvostantsev, V.N. Slesarev, V.V. Brazhkin, Toroid type high-pressure device: history and prospects, High Pressure Res. 24 (2004) 371–383.
[34] A.G. Evans, T.R. Wilshaw, Quasi-static solid particle damage in brittle solids—I. Observations analysis and implications, Acta Metall. 24 (1976) 939–956.
[35] R. Panelli, A.F. Filho, A study of a new phenomenological compacting equation, Powder Technol. 114 (2001) 255–261.
[36] R. Ohser-Wiedemann, C. Weck, U. Martin, A. Müller, H.J. Seifert, Spark plasma sintering of TiC particle-reinforced molybdenum composites, Int. J. Refract. Met. Hard Mater. 32 (2012) 1–6.
[37] A. Chu, M. Qin, d.R. ud, L. Zhang, H. Lu, B. Jia, X. Qu, Carbothermal synthesis of ZrC powders using a combustion synthesis precursor, Int. J. Refract. Met. Hard Mater. 36 (2013) 204–210.

DISSERTATIONS DEFENDED AT TALLINN UNIVERSITY OF TECHNOLOGY ON *MECHANICAL ENGINEERING*

1. **Jakob Kübarsepp**. Steel-Bonded Hardmetals. 1992.

2. **Jakub Kõo**. Determination of Residual Stresses in Coatings &Coated Parts. 1994.

3. **Mart Tamre**. Tribocharacteristics of Journal Bearings Unlocated Axis. 1995.

4. **Paul Kallas**. Abrasive Erosion of Powder Materials. 1996.

5. **Jüri Pirso**. Titanium and Chromium Carbide Based Cermets. 1996.

6. **Heinrich Reshetnyak**. Hard Metals Serviceability in Sheet Metal Forming Operations. 1996.

7. **Arvi Kruusing**. Magnetic Microdevices and Their Fabrication methods. 1997.

8. **Roberto Carmona Davila**. Some Contributions to the Quality Control in Motor Car Industry. 1999.

9. **Harri Annuka**. Characterization and Application of TiC-Based Iron Alloys Bonded Cermets. 1999.

10. **Irina Hussainova**. Investigation of Particle-Wall Collision and Erosion Prediction. 1999.

11. **Edi Kulderknup**. Reliability and Uncertainty of Quality Measurement. 2000.

12. **Vitali Podgurski**. Laser Ablation and Thermal Evaporation of Thin Films and Structures. 2001.

13. **Igor Penkov**. Strength Investigation of Threaded Joints Under Static and Dynamic Loading. 2001.

14. **Martin Eerme**. Structural Modelling of Engineering Products and Realisation of Computer-Based Environment for Product Development. 2001.

15. **Toivo Tähemaa**. Assurance of Synergy and Competitive Dependability at Non-Safety-Critical Mechatronics Systems design. 2002.

16. **Jüri Resev**. Virtual Differential as Torque Distribution Control Unit in Automotive Propulsion Systems. 2002.

17. **Toomas Pihl**. Powder Coatings for Abrasive Wear. 2002.

18. **Sergei Letunovitš**. Tribology of Fine-Grained Cermets. 2003.

19. **Tatyana Karaulova**. Development of the Modelling Tool for the Analysis of the Production Process and its Entities for the SME. 2004.

20. **Grigori Nekrassov**. Development of an Intelligent Integrated Environment for Computer. 2004.

21. **Sergei Zimakov**. Novel Wear Resistant WC-Based Thermal Sprayed Coatings. 2004.

22. **Irina Preis**. Fatigue Performance and Mechanical Reliability of Cemented Carbides. 2004.

23. **Medhat Hussainov**. Effect of Solid Particles on Turbulence of Gas in Two-Phase Flows. 2005.

24. **Frid Kaljas**. Synergy-Based Approach to Design of the Interdisciplinary Systems. 2005.

25. **Dmitri Neshumayev**. Experimental and Numerical Investigation of Combined Heat Transfer Enhancement Technique in Gas-Heated Channels. 2005.

26. **Renno Veinthal**. Characterization and Modelling of Erosion Wear of Powder Composite Materials and Coatings. 2005.

27. **Sergei Tisler**. Deposition of Solid Particles from Aerosol Flow in Laminar Flat-Plate Boundary Layer. 2006.

28. **Tauno Otto**. Models for Monitoring of Technological Processes and Production Systems. 2006.

29. **Maksim Antonov**. Assessment of Cermets Performance in Aggressive Media. 2006.

30. **Tatjana Barashkova**. Research of the Effect of Correlation at the Measurement of Alternating Voltage. 2006.

31. **Jaan Kers**. Recycling of Composite Plastics. 2006.

32. **Raivo Sell**. Model Based Mechatronic Systems Modeling Methodology in Conceptual Design Stage. 2007.

33. **Hans Rämmal**. Experimental Methods for Sound Propagation Studies in Automotive Duct Systems. 2007.

34. **Meelis Pohlak**. Rapid Prototyping of Sheet Metal Components with Incremental Sheet Forming Technology. 2007.

35. **Priidu Peetsalu**. Microstructural Aspects of Thermal Sprayed WC-Co Coatings and Ni-Cr Coated Steels. 2007.

36. **Lauri Kollo**. Sinter/HIP Technology of TiC-Based Cermets. 2007.

37. **Andrei Dedov**. Assessment of Metal Condition and Remaining Life of In-service Power Plant Components Operating at High Temperature. 2007.

38. **Fjodor Sergejev**. Investigation of the Fatigue Mechanics Aspects of PM Hardmetals and Cermets. 2007.

39. **Eduard Ševtšenko**. Intelligent Decision Support System for the Network of Collaborative SME-s. 2007.

40. **Rünno Lumiste**. Networks and Innovation in Machinery and Electronics Industry and Enterprises (Estonian Case Studies). 2008.

41. **Kristo Karjust**. Integrated Product Development and Production Technology of Large Composite Plastic Products. 2008.

42. **Mart Saarna**. Fatigue Characteristics of PM Steels. 2008.

43. **Eduard Kimmari**. Exothermically Synthesized B_4C-Al Composites for Dry Sliding. 2008.

44. **Indrek Abiline**. Calibration Methods of Coating Thickness Gauges. 2008.

45. **Tiit Hindreus**. Synergy-Based Approach to Quality Assurance. 2009.

46. **Karl Raba**. Uncertainty Focused Product Improvement Models. 2009.

47. **Riho Tarbe**. Abrasive Impact Wear: Tester, Wear and Grindability Studies. 2009.

48. **Kristjan Juhani**. Reactive Sintered Chromium and Titanium Carbide-Based Cermets. 2009.

49. **Nadežda Dementjeva**. Energy Planning Model Analysis and Their Adaptability for Estonian Energy Sector. 2009.

50. **Igor Krupenski**. Numerical Simulation of Two-Phase Turbulent Flows in Ash Circulating Fluidized Bed. 2010.

51. **Aleksandr Hlebnikov**. The Analysis of Efficiency and Optimization of District Heating Networks in Estonia. 2010.

52. **Andres Petritšenko**. Vibration of Ladder Frames. 2010.

53. **Renee Joost**. Novel Methods for Hardmetal Production and Recycling. 2010.

54. **Andre Gregor**. Hard PVD Coatings for Tooling. 2010.

55. **Tõnu Roosaar**. Wear Performance of WC- and TiC-Based Ceramic-Metallic Composites. 2010.

56. **Alina Sivitski**. Sliding Wear of PVD Hard Coatings: Fatigue and Measurement Aspects. 2010.

57. **Sergei Kramanenko**. Fractal Approach for Multiple Project Management in Manufacturing Enterprises. 2010.

58. **Eduard Latõsov**. Model for the Analysis of Combined Heat and Power Production. 2011.

59. **Jürgen Riim**. Calibration Methods of Coating Thickness Standards. 2011.

60. **Andrei Surzhenkov**. Duplex Treatment of Steel Surface. 2011.

61. **Steffen Dahms**. Diffusion Welding of Different Materials. 2011.

62. **Birthe Matsi**. Research of Innovation Capasity Monitoring Methodology for Engineering Industry. 2011.

63. **Peeter Ross**. Data Sharing and Shared Workflow in Medical Imaging. 2011.

64. **Siim Link**. Reactivity of Woody and Herbaceous Biomass Chars. 2011.

65. **Kristjan Plamus**. The Impact of Oil Shale Calorific Value on CFB Boiler Thermal Efficiency and Environment. 2012.

66. **Aleksei Tšinjan**. Performance of Tool Materials in Blanking. 2012.

67. **Martinš Sarkans**. Synergy Deployment at Early Evaluation of Modularity of the Multi-Agent Production Systems. 2012.

68. **Sven Seiler**. Laboratory as a Service – A Holistic Framework for Remote and Virtual Labs. 2012.

69. **Tarmo Velsker**. Design Optimization of Steel and Glass Structures. 2012.

70. **Madis Tiik**. Access Rights and Organizational Management in Implementation of Estonian Electronic Health Record System. 2012.

71. **Marina Kostina**. Reliability Management of Manufacturing Processes in Machinery Enterprises. 2012.

72. **Robert Hudjakov**. Long-Range Navigation for Unmanned Off-Road Ground Vehicle. 2012.

73. **Arkadi Zikin**. Advanced Multiphase Tribo-Functional PTA Hardfacings. 2013.

74. **Alar Konist**. Environmental Aspects of Oil Shale Power Production. 2013.

75. **Inge Roos**. Methodology for Calculating CO_2 Emissions from Estonian Shale Oil Industry. 2013.

76. **Dmitri Shvarts**. Global 3D Map Merging Methods for Robot Navigation. 2013.

77. **Kaia Lõun**. Company's Strategy Based Formation of e-Workplace Performance in the Engineering Industry. 2013.

78. **Maido Hiiemaa**. Motion Planner for Skid-Steer Unmanned Ground Vehicle. 2013.

79. **Dmitri Goljandin**. Disintegrator Milling System Development and Milling Technologies of Different Materials. 2013.

80. **Dmitri Aleksandrov**. Light-Weight Multicopter Structural Design for Energy Saving. 2013.

81. **Henrik Herranen**. Design Optimization of Smart Composite Structures with Embedded Devices. 2014.

82. **Heiki Tiikoja**. Experimental Acoustic Characterization of Automotive Inlet and Exhaust System. 2014.

83. **Jelena Priss**. High Temperature Corrosion and Abrasive Wear of Boiler Steels. 2014.

84. **Aare Aruniit**. Thermoreactive Polymer Composite with High Particulate Filler Content. 2014.

85. **Dmitri Gornostajev**. Development of the Calculation Method for Barge Hull. 2014.

86. **Liina Lind**. Wear of PVD Coatings on Fineblanking Punches. 2014.

87. **Nikolai Voltšihhin**. Design and Technology of Oxides-Containing Ceramic-Based Composites. 2014.

88. **Aleksander Šablinski**. RANS Numerical Modelling of Turbulent Polydispersed Flows in CFB Freeboard. 2015.

89. **Tanel Aruväli**. Wireless Real-time Monitoring of Machining Processes. 2015.

90. **Andrei Bogatov**. Morphological Changes on Diamond and DLC Films During Sliding Wear. 2015.

91. **Raimo Kabral**. Aero-Acoustic Studies and Innovative Noise Control with Application to Modern Automotive Gas Exchange System. 2015.

92. **Jevgeni Sahno**. Dynamic Management Framework for Continuous Improvement of Production Processes. 2015.

93. **Ott Pabut**. Optimal Design of Slotless Permanent Magnet Generators. 2015.

94. **Merili Kukuškin**. Value Centric Business Development for Estonian Manufacturing Small and Medium Sized Enterprises. 2015.

95. **Kaimo Sonk**. Development of Additive Manufacturing Based on Functional Requirements. 2015.

96. **Marina Aghayan**. Functionalization of Alumina Nanofibers with Metal Oxides. 2016.

97. **Marek Jõeleht**. Titanium Carbide Cermet as Ballistic Protection Material. 2016.

98. **Heikki Sarjas**. Novel Synthesized and Milled Carbide-based Composite Powders for HVOF Spray. 2016.

99. **Klodian Dhoska**. Measurement Methods with 3D Coordinate Measuring Machine and Improved Characterization Setup for Detector Performance. 2016.

100. **Aleksei Snatkin**. Development and Optimisation of Production Monitoring System. 2016.

101. **Igor Poljantšikov**. Partners Selection Tool for Virtual Enterprise in SMEs Network. 2016.

102. **Sergei Žigailov**. Experimental and Analytical Modelling of Pelvic Motion. 2016.

103. **Rommi Källo**. Synergy-Based Chaos Control in the Multi-Agent Hierarchical Systems. 2016.